Graduate School ETD Form 9
(Revised 12/07)

PURDUE UNIVERSITY
GRADUATE SCHOOL
Thesis/Dissertation Acceptance

This is to certify that the thesis/dissertation prepared

By Jordi Condominas

Entitled
MOBILE PHONE BASED IMAGING SYSTEM FOR SELECTED TELE-HEALTHCARE APPLICATIONS

For the degree of Master of Science

Is approved by the final examining committee:

Suranjan Panigrahi
Chair

Robert J. Herrick

Alicia Casals

To the best of my knowledge and as understood by the student in the *Research Integrity and Copyright Disclaimer (Graduate School Form 20)*, this thesis/dissertation adheres to the provisions of Purdue University's "Policy on Integrity in Research" and the use of copyrighted material.

Approved by Major Professor(s): Suranjan Panigrahi

Approved by: James L Mohler 05/30/2013
Head of the Graduate Program Date

MOBILE PHONE BASED IMAGING SYSTEM FOR SELECTED TELE-HEALTHCARE APPLICATIONS

A Thesis

Submitted to the Faculty

of

Purdue University

by

Jordi Condominas

In Partial Fulfillment of the

Requirements for the Degree

of

Master of Science

August 2013

Purdue University

West Lafayette, Indiana

UMI Number: 1549315

UMI 1549315

ProQuest LLC.
789 East Eisenhower Parkway
P.O. Box 1346
Ann Arbor, MI 48106 - 1346

ACKNOWLEDGMENTS

The author would like to thank the thesis committee for their help and guidance throughout the development of this thesis, and in particular Professor Panigrahi for his effort in providing all the necessary knowledge to write the thesis. Also, the author would like to thank the skin cancer image database sources Dermis.net, DermQuest.org and Dermnetnz.org to provide the skin cancer images used in this research.

TABLE OF CONTENTS

Page

LIST OF TABLES

Table Page

Table Page

LIST OF FIGURES

Figure Page

Figure Page

Figure Page

Figure Page

ABSTRACT

Condominas, Jordi. M.S., Purdue University, August 2013. Mobile Phone based imaging system for selected Tele-Healthcare applications. Major Professor: Suranjan Panigrahi.

A mobile phone based telemedicine study is developed to see how feasible phone usage is in selected health care applications. The research is divided into three different objectives. The first objective is to compile the technical characteristics of selected mobile phones from telemedicine perspective. The second objective is to develop techniques to acquire quality images of skin with mobile phones. Finally a smartphone based telemedicine application will be developed to assess skin cancer.

CHAPTER 1. INTRODUCTION

Chapter 1 introduces the problem stating the scope and its significance. The most important key terms will be defined and it will present the assumptions, delimitations and limitations.

1.1 Statement of purpose

The goal is to study the feasibility of mobile phones for telemedicine applications. The specific objectives are to:

1. Compile the technical and functional capabilities of one popular cellphone and 3 popular smartphones for telemedicine applications.
2. Develop techniques for acquiring quality images of skin and oral cancer for telemedicine applications using mobile phones.
3. Develop and evaluate computer vision methods (algorithms / program) to process, analyze and interpret for skin cancer medical images for skin cancer assessment.

1.2 Scope

The research is limited to compile the technical capabilities of mobile phones from a telemedicine perspective. Techniques for acquiring images will be evaluated to enhance the quality of images taken by mobile phones. The images will be obtained under a controlled environment.

A mobile phone telemedicine application is developed to assess the disease of selected medical images. The application is based in skin cancer disease detection.

1.3 Significance

This research expands knowledge in the telemedicine area by developing a set of techniques for acquiring quality medical images with mobile phones. A mobile phone based telemedicine application is developed to diagnose automatically selected diseases. The study of the feasibility of mobile phones in telemedicine enhances the knowledge of this technology for remote diagnosing.

1.4 Research question

The research question of this study is:

- How can we improve the quality of images from standard cellphones and smartphones for telemedicine purposes?
    - Can we build a reliable smartphone based skin disease telemedicine application?

1.5 Definitions

This section defines the key terminology used throughout the research:

Android: Open source platform, hardware independent operating system for principally smartphones and tablets (Hugo, Lourenço & Paz, 2011a, p 111).

Computer Vision: Computer vision is the science that analyzes images trying to produce quantitative or qualitative data extracted from that image. In this field algorithms are developed to process, segment, extract and recognize features detected in the image (Panigrahi & Gunasekaran, 2000, p 39).

e-Health: Electronic Health is the practice of healthcare remotely. (Perera, 2012, p 1)

m-Health: practice of e-Health but using mobile phones and other portable devices such as tablets. (Perera, 2012, p 1)

OpenCV: open source computer vision software library.

Telemedicine: Telemedicine is the discipline that uses informational and communication technologies in order to provide health care remotely (Matheus & Ribeiro, 2009, p 275).

1.6 Assumptions

The assumptions for this research are:

- Mobile cameras with more than 1 Megapixels resolution are sufficient for telemedicine applications.

- The telemedicine application will be developed under Android platform and using OpenCV 2.4 libraries.
- The research will use the skin mole images from available resources.

1.7 Delimitations

The research acknowledges the following delimitations:

- The evaluation and comparison of mobile phones does not take into account more phones than chosen for the research.
- The evaluation and comparison do not include tablets and other devices without camera and standalone cameras.
- The methodology to improve the images for telemedicine does not include standalone cameras.
- The techniques to enhance image quality do not require any special and expensive equipment.

1.8 Limitations

The research acknowledges the following limitations:

- The research for evaluation and comparison of standard cellphones and smartphones from telemedicine perspective utilizes 4 distinct cellphones: Nokia, Android, iPhone and Blackberry.
- The dataset of images used for telemedicine application apply only for skin cancer.
- The research does not generate any datasets of images.

- The application is tested in a Samsung Galaxy SII.

1.9 Summary

This chapter provides an overview of the research introducing the statement of purpose, the scope and significance of this thesis. Finally the definitions, research question, assumptions, limitations and delimitations are specified. The objectives of the thesis are divided in three steps to assess if mobile phones are capable to perform telemedicine tasks by using images of skin cancer diseases.

CHAPTER 2. LITERATURE REVIEW

The goal of developing a system of smartphone based health care system for remote diagnosis requires an understanding of the evolution of telemedicine and the technology used for its application. The concept of telemedicine has been widely used for different purposes such as remote monitoring of elderly people, monitoring for chronic diseases or only as a system that captures medical images and send them through the internet. A state of the art literature review of this thesis focuses on three specific areas:

- Telemedicine
- Smartphones
- Computer vision

2.1 Telemedicine

Telemedicine is also known as Telehealth or e-Health. It is the discipline that uses informational and communication technologies in order to provide health care remotely (Matheus & Ribeiro, 2009). The persistent increase of the costs of health care, mainly in developed countries, has increased the interest of researchers to reduce hospitalizations of the patients (Rashkovska, Tomasic & Trobec, 2011). Such hospitalizations can be reduced by developing better telemedicine systems. Subsequently, this will allow the patients to stay home without losing the quality of health care. Telemedicine applications bring the information to the right place at the right moment to the right person in correct form (Ganapathy & Ravindra, 2008).

Telemedicine is useful in rural areas or when distance is a critical factor, for instance when the specialist required is not in the same hospital as the patient. Countries can benefit greatly from telemedicine technologies to provide health care to isolated locations. Furthermore, these technologies can improve the quality of life in locations with a few specialists.

Currently the vast majority of telemedicine applications are developed in western world, despite the fact that developing countries would benefit more from these applications. Telemedicine applications could bring health care to needy areas. Countries with low resources tend to lack specialists, equipment and hospitals. The problem of lack of specialists can partially be addressed by using telemedicine services.

Currently, E-Health services can be found in academic medical institutions, and rural hospitals. They are also used in international links between hospitals from developed countries and hospitals from developing countries (Nutalapati, Boyapati, Jampani, & Dontula, 2011). US Army widely uses telemedicine. For example, they have been using teledermatology to diagnose and treat skin diseases for many years, treating as many as 30,000 cases (Lowie, 2012).

Despite the social benefits telemedicine could bring to society, there are technical, economical and legal implications before deploying an e-Health system. Such systems must be evaluated with humans, but normally, multiple permissions are required before starting the investigations. Thus, the costs of the development of these systems are higher. Due to the fact that telemedicine is still a discipline not considered positively amongst specialists (Hitchcock, 2011), the investments on research is diverted to other areas before going to telemedicine. This results in a lack of development of policies to standardize the telemedicine procedures. In conclusion, the development of telemedicine depends less on the technology than the development of policies, intercommunication between hospitals, security, liability, etc. Besides these implications, these systems must be reliable, accurate and easy to use (Sposaro & Tyson, 2009). The other critical issue is to comply with appropriate policies and protocols to work with human medical samples (i.e. skin cancer images).

2.1.1 Telemedicine imaging

To provide service of telehealth, information must be acquired and transmitted over internet. Telemedicine is currently a discipline because it is much faster to send large amount data than it was possible 10 years ago. Typically, m-Health applications send radiographs, medical test results, medical images or patients' health information via internet. Medical imaging produces the possibility to diagnose certain diseases remotely as long as these images meet quality requirements. Although, medical imaging is not always necessary to diagnose remotely, it adds more value to the diagnostic process. Different studies demonstrate that diagnosing remotely with only images has around 80% accuracy (Hsieh, Tsai, Yin, Chen, Yang & Jeng, 2004). Although medical imaging is an important part of telemedicine, it is challenging to use it and obtain good results. Remote diagnosing of certain diseases requires specific images. For instance telemedicine applications of dermatology uses dermascopy images, and these are difficult to acquire by non-specialists (Cavalcanti & Scharcanski, 2011). Sometimes, the person responsible of obtaining the image is not an expert. Thus the images might not have sufficient quality to be used in diagnosis. Therefore, to allow the users to use telemedicine service in home, it is required to teach non-specialists how to acquire quality medical images. However, the purpose of consumer cameras is not for telemedicine, for that reason pictures obtained by standalone cameras require preprocessing to be used in telemedicine (Cavalcanti & Scharcanski, 2011).

2.1.2 Technology in telemedicine

E-Health benefits from the new forms of connection to the internet like 3G, LTE, fiber optics, and ADSL. Typically, a telemedicine application generates vast amounts of data. Ten years ago, when the common internet connection was a 56 kbps modem or ISDN, these applications were not possible to implement. The new broadband technology has reshaped telemedicine discipline. Currently, send high resolution images is affordable (Istepanian, Pattichis, & Laxminarayan, 2006) containing significant amount of data. Telemedicine applications benefit from using wireless connectivity together with sensors for physiological monitoring of health data such as heart rate (Finlay, Nugent, Breen, Bond, & Moore, 2009). Also studies in emergency handling demonstrate that patient survival depends on the effectiveness of pre-hospital healthcare (Batistatos, Tsoulos, & Athanasiadou, 2012). Therefore remote health care systems are of vital importance to handle more effectively these situations (Bailo, Barbieri, & Cevasco, 2005; Batistatos et al., 2012). Telemedicine in an emergency unit can send critical physiological information to the hospital.

Camera technology used for telemedicine purposes has advanced significantly. In recent years, camera resolution has increased from 3 megapixels (MP) to 15 MP. These digital cameras have a variety of in-built functionalities (i.e. white balance, color calibration and adjustments). Flash is useful to prevent low exposure pictures, but sometimes the flash can aggravate the quality of the image (Romero, Cortina, & Vera, 2008). However, from the perspective of this research, the revolution lies in the mobile phone cameras. Earlier mobile phone cameras were quite rudimentary and simplified versions of standalone cameras; with very low resolution. However, it was feasible to use those low resolution cameras for telemedicine applications (Wirthlin et al., 1998). Currently available mobile cameras can be compared with the standalone cameras, perhaps with less functionalities. Mobile phones are used in telemedicine, not only because of the cameras but for other advantages as well (portability, internet connection, computing power and high resolution cameras). The discipline that uses mobile phones for telemedicine application is known as m-health (Perera, 2012).

2.1.2.1 Applications in telemedicine

This section presents applications in remote pathology, dermatology, dentistry, care of patients, monitoring of physiological parameters, and emergency handling.

Pathology is the diagnosis of diseases. Pathology tries to explain the cause and effect of injured or ill cells or skin. Telepathology is the diagnosis of diseases remotely by sending images or video of the region of interest. For instance, the University of Basel, Switzerland developed an “app” called iPath that provided a web-based platform for second opinions. It also incorporated a set of images and virtual slides of diseases to train the specialists in developing areas (Hitchcock, 2011). Another study developed a methodology to acquire images with mobile phones directly from the microscope, without any add-on. Then these images were sent through Multimedia Messaging Service (MMS), which have high penetration in the world (Bellina & Missoni, 2009).

Dermatology is a discipline that can benefit enormously from the telemedicine. Dermatology is the medical field that studies skin diseases, including hair, nails and scalp. Therefore, remote dermatology is known as teledermatology. The possible applications for teledermatology are obvious because it is relatively easy to obtain images of skin parts and send them to the specialist. Moreover, there has been research in the area of computer-aided diagnostic systems to help the doctors by providing additional information about the disease. These automatic diagnostic systems use computer vision algorithms to extract important features of the regions of interest. These systems, under controlled environments, showed an accuracy of higher than 95% (Cavalcanti & Scharcanski, 2011). Teledermatology systems can also be used as second opinion platform (Lowie, 2012), or for triage of seriousness of the wound and thus prioritize the most injured patients (Hsieh et al., 2004).

Western countries are currently facing the challenge of providing new care needs to elderly people. The population of the elderly is increasing and their health care is important. Telemedicine could present a solution to decrease the pressure on the healthcare system. The discipline of telemedicine that addresses this situation is known as telecare. Telecare normally uses all the technology available to control and monitor the status of the patient. Domotics, sensors, webcams, and mobile phones monitor the patient constantly and in case of emergency, the key persons are alerted (Milligan, Roberts, & Mort, 2011).

Telemedicine has benefited significantly from applications of health monitoring using small remote devices that connect through the internet to a central server located in hospitals. These monitoring systems are mainly composed of a sensor, a Bluetooth device, a receiver device that is capable to connect to the internet and the central server (Hugo, Lourenço & Paz, 2011; Marshall, Medvedev & Antonov, 2008; Rashkovsk, Tomasic & Trobec, 2011; Sposaro & Tyson, 2009; Woodbridge, Nahapetian, Noshadi, Sarrafzadeh & William, 2009). These systems can monitor heart or respiratory diseases. Telemedicine monitoring is an interesting application because patients always carry their own cellphones.

In emergencies, telemedicine applications have an important task to send in real time information about the patients (i.e. video, electrocardiograms, blood pressure or respiratory rate are transmitted and stored in the hospital) (Bailo et al., 2005).

2.2 Mobile phones

In the 21st century, mobile phones have been a vital part of our society. 15 years ago they were used only to call and text. They did not have camera or GPS. As it is mentioned in Ascent of Smartphones (Charlesworth, 2010), the best smartphone of today is an ordinary phone of tomorrow, meaning that the evolution of this technology is growing rapidly. The mobile phones today are also being used as video player, videogame system or GPS navigator.

2.2.1 Smartphones

This decade can be considered as the decade of the portable personal computers with the explosion of the smartphones and tablets. The worldwide sales of smartphones grew 47% (Goasduff & Pettey, 2012). Although that growth corresponds mainly in developed countries, this high demand creates cheaper models of the most popular and expensive smartphones. These cheaper versions of the most popular smartphones still have the basic functionalities somebody would expect from a cellphone: 1 to 5 MP camera, touch screen and a reasonable high speed CPU of more than 500 Mhz.

Most of the smartphones available now have a high resolution camera, from 1 MP to 13 MP. A powerful CPU that can reach up to 1.5 Ghz. Moreover, these smartphones have added capabilities, i.e. GPS, accelerometer, extra camera, SD card, compass, etc.

In Table 2.1 the market share for each platform is illustrated. Android is the platform most used in the world followed by Apple and its iPhone. Both platforms together have 85% of the market while the remaining 15% is shared between RIM BlackBerry, Microsoft with Windows Phone and Symbian.

Table 2.1: Smartphone platform market share in US. (ComScore, 2012)

Top Smartphone Platforms
3 Month Avg. Ending Oct. 2012 vs. 3 Month Avg. Ending Jul. 2012
Total U.S. Smartphone Subscribers Ages 13+
Source: comScore MobiLens

	Share (%) of Smartphone Subscribers		
	Jul-12	**Oct-12**	**Point Change**
Total Smartphone Subscribers	**100.0%**	**100.0%**	**N/A**
Google	52.2%	53.6%	1.4
Apple	33.4%	34.3%	0.9
RIM	9.5%	7.8%	-1.7
Microsoft	3.6%	3.2%	-0.4
Symbian	0.8%	0.6%	-0.2

2.2.2 Standard phones / cellphones

A standard phone (cellphone) is less capable than the smartphones, with a low resolution camera, physical keyboard or standard touch screen. However, sometimes the distinction between cellphone and a smartphone is not clear. From the perspective of this research anything that does not have touch screen, sensors, high connectivity and high definition camera is considered a cellphone.

According to the Garnet 2012 report, the most important seller for standard phones is Nokia, whose sales are currently declining because of the rapid growth of smartphones. In 2011, there were 6,000 million cellphones subscriptions in the world (International Telecommunication Union, 2012), with a distribution of1, 500 million in developed countries and 4,500 in developing countries. Although, next generation mobile networks are not deployed yet in those countries (3G and LTE), there has been research using GPRS networks to send SMS and MMS with medical information (Istepanian et al., 2006).

2.3 Uses of the smartphones for telemedicine applications

The machine vision algorithms are computer intensive because they work with large data structures such as images. However, smartphones can execute computer vision algorithms for telemedicine applications (Alcón et al., 2009; Cavalcanti & Scharcanski, 2011). Also, the smartphone's connectivity allows sending medical data through internet, meeting one of the critical characteristics of telemedicine. High resolution camera images are of the order of Megabytes. So using 3G network with an average speed of 1Mbps, it will take more than a few minutes to send and image.

So far, there are studies of telemedicine applications for skin disease recognition (Tran, Ayad, Weinberg, Cherng, Chowdhury, Monir, El Hariri, Kovarik, 2011); (López Ruiz , et al., 2012) demonstrated oxygen presence recognition using a special architecture configuration to create a chemical reaction to see presence of oxygen in the red spectrum of the RGB color space; Quantification of colors on colorimetric diagnosis assays was demonstrated by Shen et al. (2012). Colorimetric assays in these little color strips used to measure the pH of the water; telemedicine applications for monitoring physiological parameters such as hearth rate (Hugo et al., 2011; Rashkovska et al., 2011; Sposaro & Tyson, 2009).

2.4 Computer vision

Computer vision is the science that analyzes images to produce quantitative or qualitative data extracted from that image. Images are processed, and segmented to extract features. Afterwards, these features are used to understand the image (Panigrahi & Gunasekaran, 2000). With computer vision it is possible to recognize patterns to detect concrete diseases. Computer vision is also known as machine vision or computing imaging.

The basic components in a computer vision system are:

- Camera
- Frame grabber
- Light source
- Computer

Computer vision, specifically object recognition, is still a difficult computational problem. For example, recognition of objects is a very complicated problem because of the many pictures that can be taken from infinite orientations of the object, pose or light conditions (Pinto, Cox & DiCarlo, 2008). However, with appropriate algorithms, it is possible to achieve high levels of accuracy.

2.4.1 Computer vision in tele-healthcare applications

Computer vision is critical to telemedicine applications. The objective is to improve the medical image to facilitate the physicians to diagnose. Computer aided diagnosis (CAD) systems are useful in areas where the physician has to analyze the characteristics of an image where the probability of misclassification is high. For example a radiologist may miss around 30% of the lung nodules in chest radiographs where some of the nodules are clearly visible (Doi, 2009). In that specific case, a computer vision system was implemented to help the radiologist to detect the nodules by image differencing. The nodule candidates were thresholded and filtered. Finally those nodules that passed through all the filters were highlighted. CAD systems have been used in dermatology (Alcón et al., 2009; Cavalcanti & Scharcanski, 2011), dentistry (Brüllmann, Alvarez, & Willershausen, 2009) or radiology (Doi, 2009). Normally, CAD systems use the process described in Figure 2.2 to interpret the images.

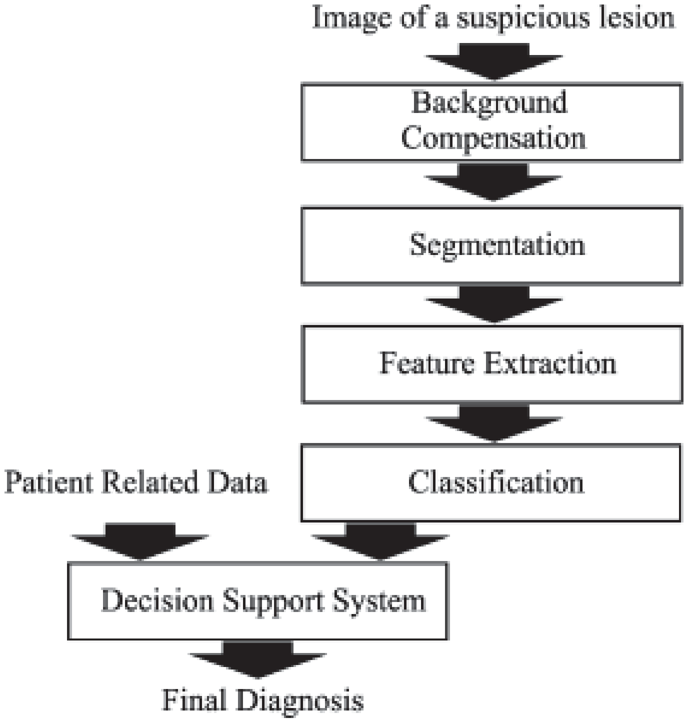

Figure 2.1: *Workflow of a medical image diagnostic system (Alcón, Ciuhu, Kate, Heinrich, Uzunbajakava, Krekels, Siem & de Haan, 2009)*

Because the noise of the image and uneven illumination areas in regions of interest, appropriate image processing operations is critical. Sometimes, before background compensation, it is useful to change the color space of the image (Cavalcanti & Scharcanski, 2011). Color space defines how the colors are represented. The most popular color space is RGB and it is used in printing, television, and electronic display applications. However, RGB is not always the best color space representation because it is not very intuitive. There are also other representations of color spaces (i.e. Hue, Saturation and Intensity (HSI) or Hue, Saturation and Lightness (HSL)) which are intuitive (Smith, 1978).

The next step is to segment the image. The goal of segmenting is to obtain the region of interest where the melanoma is located. When the melanoma is segmented, pattern recognition algorithms are used to classify the image as malign or benign melanoma. Pattern recognition uses features to interpret the image and classify it. The features for this study follow the ABCD rule of dermatoscopy. ABCD stands for Asymmetry, Border, Color and Diameter. The rule is used to differentiate melanomas from benign moles because melanomas tend to be very asymmetric, with blurry borders, inhomogeneous colors and diameters bigger than 6mm (JAMA, 2011).

2.4.2 Image segmentation

Image segmentation is the process of organizing the image into similar regions (Adams & Bischof, 1994). Similar regions are areas of the image with similar pixels. Image segmentation algorithms can be classified in four types: histogram threshold based segmentation, border detection, region detection and hybrid techniques. These algorithms are widely used because they reduce the quantity of information of the image in order to be able to extract and classify objects. Segmentation algorithms vary according the type of image expected. For example if the image is composed of background and one object, a threshold base algorithm can be used. But if the image is more complicated, more objects in the scene, other types of segmenting algorithms are needed, for instance region growing algorithms.

The threshold based algorithms analyze the distribution of pixels values and it plots the frequency into a histogram, exemplified in Figure 2.4. Then a threshold is used to separate the object from the background. For example, the well-known Otsu's algorithm works very well in this kind of single object images. It dynamically assigns a threshold by maximizing the between class variance. However, these type of algorithms are not very suitable under noise images, change of illuminations and images with more than one object (Kurita, Otsu, & Abdelmalek, 1992).

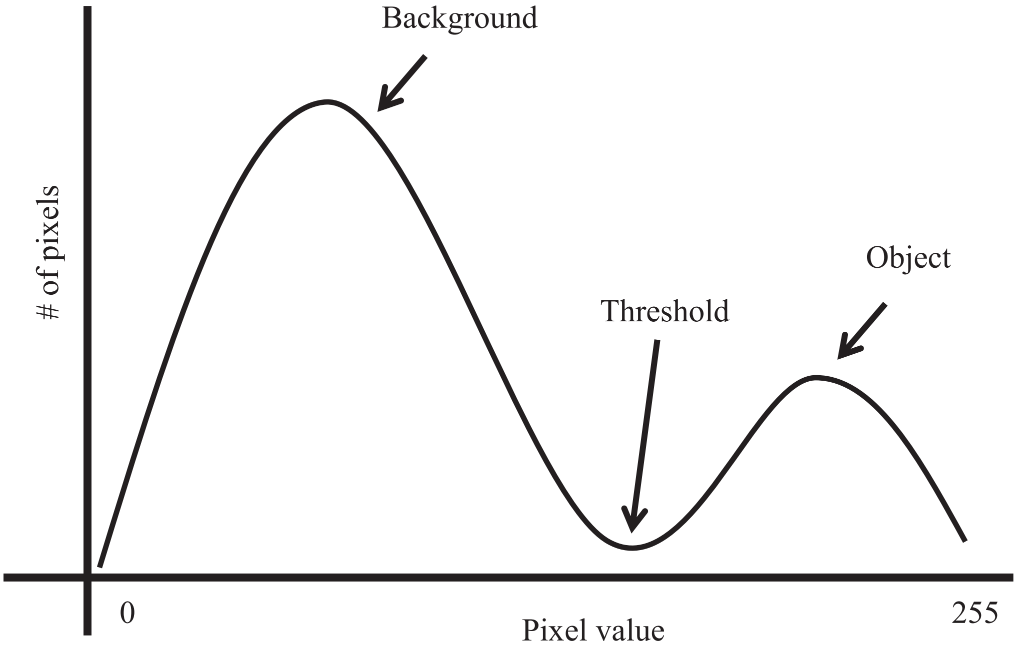

Figure 2.2: *Otsu's dynamic thresholding*

Region growing is a robust and fast algorithm for segmentation. Region growing analyze the similarity of each pixel to decide if a pixel belongs to the same group or not. However, these types of algorithms are not very suitable when there are illumination issues in the image and the intensity of the pixels vary too much. Normally, region growing algorithms need a seed to start the process. This seed consists of a value which the algorithm will use to start the segmentation by grouping pixels similar to this seed into groups (Gao, Mas, Kerle, & Navarrete Pacheco, 2011).

2.4.3 Skin cancer features

Features represent information which define the pattern desired to be analyzed (i.e. shape, borders, color, holes, etc.). The features used for pattern classification algorithms related with skin cancer applications usually follow the ABCD rule. The ABCD rule is a scoring rule according the strength of four characteristics: asymmetry, sharpness of the border, color and diameter. Once the features are extracted, the pattern recognition algorithm decides whether there is cancer or not (Alcón et al., 2009).

The asymmetry features usually are obtained by enclosing the segmented melanoma with a bounding box. Then it is possible to check geometric properties such as the compactness of the melanoma (Cavalcanti & Scharcanski, 2011) which is obtained by the ratio shown in equation, (Maglogiannis & Doukas, 2009):

$$Compactness = \frac{Perimeter^2}{Area} \tag{2.1}$$

Circularity is another important geometry property independent of scale and orientation obtained using the below formula, (Montero & Bribiesca, 2009):

$$Circularity = \frac{\mu_R}{\sigma_R} \tag{2.2}$$

Where μ_R and σ_R are the mean and standard deviation of the distance from the centroid to the border of the melanoma.

The bounding rectangle is used to find the principal and secondary axes. These axes cut the melanoma in four different regions. Afterwards, it is possible to calculate dozens of different features such as symmetry between areas drawn by the axes, ratios between axes, ratio between healthy areas and melanoma areas, and so on (Cavalcanti & Scharcanski, 2011).

The color features found in the literature review for skin cancer classification are usually statistical information of the color components of the melanoma. Thus, it is common to use specific color spaces such as HSI, HSV, or normalized RGB to eliminate illumination issues. For instance HSI separates the hue of the color to its saturation, so it is more logical to compute averages on the hue part of the color. On the other hand, using RGB it is not possible to differentiate same colors but with different intensities. Normally average and standard deviation is calculated for each component of the color space, (Przystalski, 2010).

For border features, it is common to use an edge detector like gradient. From the edges it is extracted the magnitude of the gradient. It is known that melanomas tend to have blurry edges, and benign moles tend to have clearly demarked borders (Cavalcanti & Scharcanski, 2011).

2.4.4 Pattern classification

Pattern classification is a great computer vision challenge. These algorithms use extracted features to classify objects. Usually the algorithms of classification work with thousands of different features hence are computer intensive. Therefore, one of the problems of pattern classification is to select the best set of features to allow the classifier to classify quickly and with high accuracy. Typically, machine learning algorithms are used at the same time to select the best set of features and to classify the patterns (Viola & Jones, 2004). Generally pattern classification algorithms are supervised machine learning systems. Thus they use labeled data to train the model. In the skin cancer case, the images used to train the pattern classification algorithms are medical labeled samples of skin cancer and benign moles, thus these samples are already diagnosed. In literature we find that to classify melanomas the following pattern classification algorithms are used: Boosting algorithms, which take a set of smaller and weak classifiers to build a stronger classifier(Alcón et al., 2009); Support Vector Machine (SVM), which separates the data in two categories with an hyper plane (Przystalski, 2010); Neural Networks (Maglogiannis & Doukas, 2009); k-nearest neighbor classification is also commonly used because of its performance and good accuracy (Ganster et al., 2001); Also have been used regression trees, decision trees and Bayesian networks (Maglogiannis & Doukas, 2009).

2.5 Summary

Chapter two reviewed the previous work in telemedicine, using smartphones and computer vision algorithms. Although research of telemedicine using smartphones and their cameras is limited, there are a few studies that prove the potential of mobile phones in telemedicine. The review indicates that that smartphones would be incorporated in telemedicine applications using computer vision algorithms to detect skin cancer.

CHAPTER 3. METHODOLOGY

In this chapter is explained the development approach of the three objectives.

3.1 Objective one: mobile phone comparison

The first objective is to compile the technical and functional capabilities of one popular cellphone and 3 popular smartphones for telemedicine applications. First, it is determined the current market share for cellphones and smartphones to compile a list of the most popular mobile phones in the USA. Then three smartphones and one standard cellphone are selected: Android, iPhone, BlackBerry and Nokia. The four cellphones have to meet the following minimum capabilities:

a. Color screen
b. Camera with a resolution of equal or more than 1 MP
c. Connectivity with General Packet Radio Service (GPRS) or better

The characteristics that it is used for the evaluation of the mobile phones are:

a. CPU
b. Size of the phone
c. Weight

d. Storage

e. Battery

f. Cost

g. Connectivity

h. Camera resolution

i. Inbuilt camera functions

To evaluate and compare the phone cameras it is insufficient to just compile the technical aspects of the cameras. The principal differences between the phone cameras are detected after performing a controlled test.

The test consists of two scenarios to evaluate different aspects of the camera. The first scenario evaluates the color quality. To perform this test, a ColorChecker chart presented in Figure 3.1 is used. The chart is a printed color card with 14 different colors.

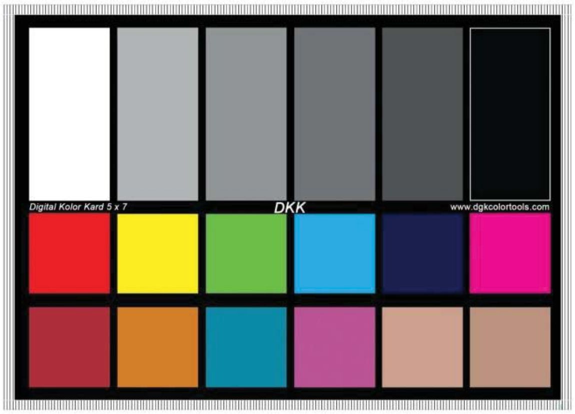

Figure 3.1: *ColorChecker used for smartphone color calibration (Obtained from Amazon.com)*

For each phone, images of the color squares of the ColorChecker chart are obtained at the maximum quality of the phone using daylight balanced light, the lowest possible ISO and the white-balance configured to daylight. Afterwards, the red, green, blue, white and black squares are evaluated using its histogram.

The second test consists of evaluating the overall sharpness of the image. The resolution of the camera impacts directly the sharpness of the image. Other factors (optics of the camera and the inbuilt functionalities that preprocess the image) also affect the image quality. To perform the test, an ISO 12233 chart illustrated (Figure 3.2), is used. Afterwards, the image is closely analyzed to detect at which level the lines are undistinguishable, that the camera is not able to represent that level of line separation.

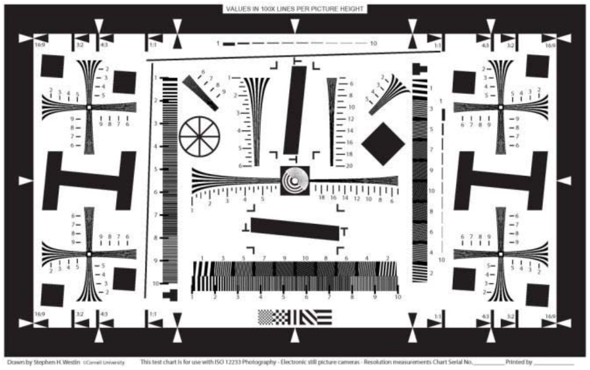

Figure 3.2: *ISO 12233 chart (Westin, 2010)*

3.2 Objective two: methodology to acquire quality images

Objective two consists of developing techniques for acquiring quality images of skin and oral cancer for telemedicine applications using mobile phones. For this objective, different procedures to acquire quality pictures are investigated for telemedicine purposes. The effects external sources of light are studied. Therefore it is defined a set of configurations for image acquisition.

It is used a doll as the subject to acquire skin images. Due to the high variety of camera flashes available in the market, the camera flash is intentionally disabled. Therefore the light sources used for this objective are standard room light and a table light with daylight source (Color temperature of 6300K). two smartphones are used, Samsung Galaxy SII with 8 MP camera, BlackBerry Curve 9300 with 2 MP camera. The standard cellphone Nokia 2720 with 1.3 MP camera is also used as the cellphone.

Three experiments are conducted to differentiate which lighting configuration yielded the best quality, (Figures 3.3, 3.4 and 3.5):

1. Room light with table light on the side
2. Table light on the side
3. Table light on the front

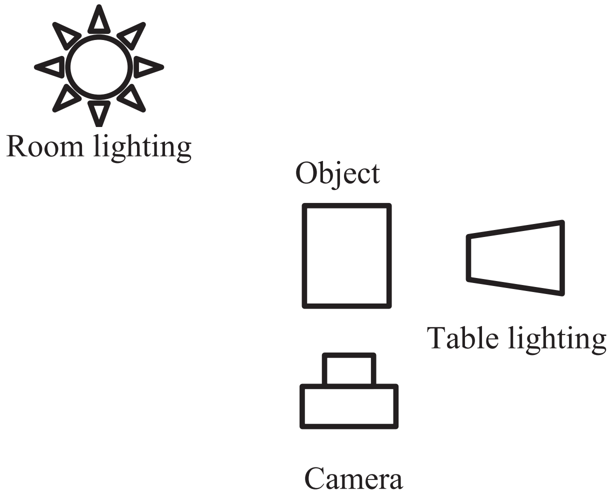

Figure 3.3: *Configuration 1: Room light with table light on the side*

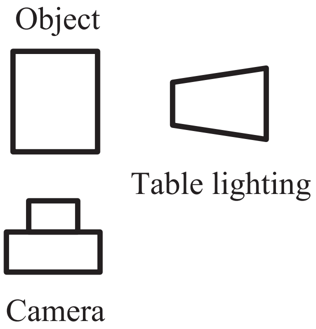

Figure 3.4: *Configuration 2: Table light on the side*

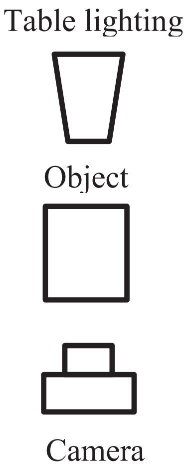

Figure 3.5: *Configuration 3: Table light on the front*

3.3 Objective three: develop a mobile phone based telemedicine application for skin cancer assessment

Figure 3.7 illustrates application process for skin cancer classification. Different standard computer vision operations (image processing, image analysis and image understanding) are incorporated as shown in the flow chart.

3.3.1 Image acquisition

As it is beyond the scope for this research to acquire skin images (cancerous and benign) from human subjects, it is obtained previously acquired and classified images from different sources (Table 3.1). In total 291 images are used, of which 143 are melanomas and 148 are benign moles.

Table 3.1: Sources of skin mole images

Melanoma		**Benign mole**	
Number of images	**Source**	**Number of images**	**Source**
67 images	Dermnetnz.org	73 images	Dermnetnz.org
44 images	Dermis.net	65 images	Dermis.net
32 images	DermQuest.org	10 images	DermQuest.org

3.3.2 Platform used

The obtained images are processed and analyzed in OpenCV (Itseez, 2013) environment in both MS-Windows and Android OS.

3.3.3 Skin cancer image classification overview

The process for the skin cancer image classification program follows the steps shown in Figure 3.6:

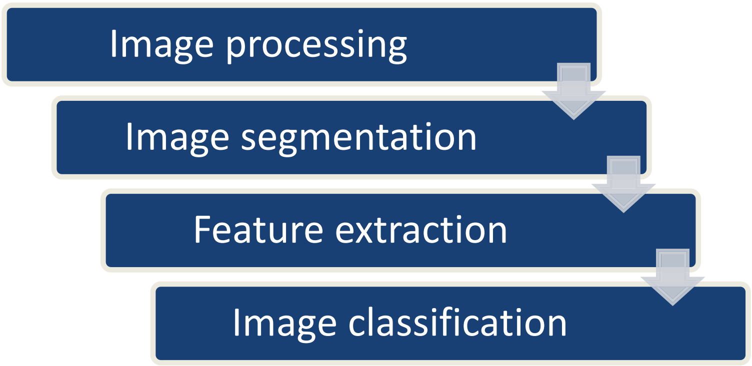

Figure 3.6: *Skin cancer application process*

- Image processing is the step to enhance the quality of the image and thus facilitate the segmentation process.
- Image segmentation is the process which will separate the mole from the background.
- Feature extraction will obtain information from the segmented mole such as asymmetry, color or border information.
- Image classification will use the features information to decide whether the image is a melanoma or a healthy mole.

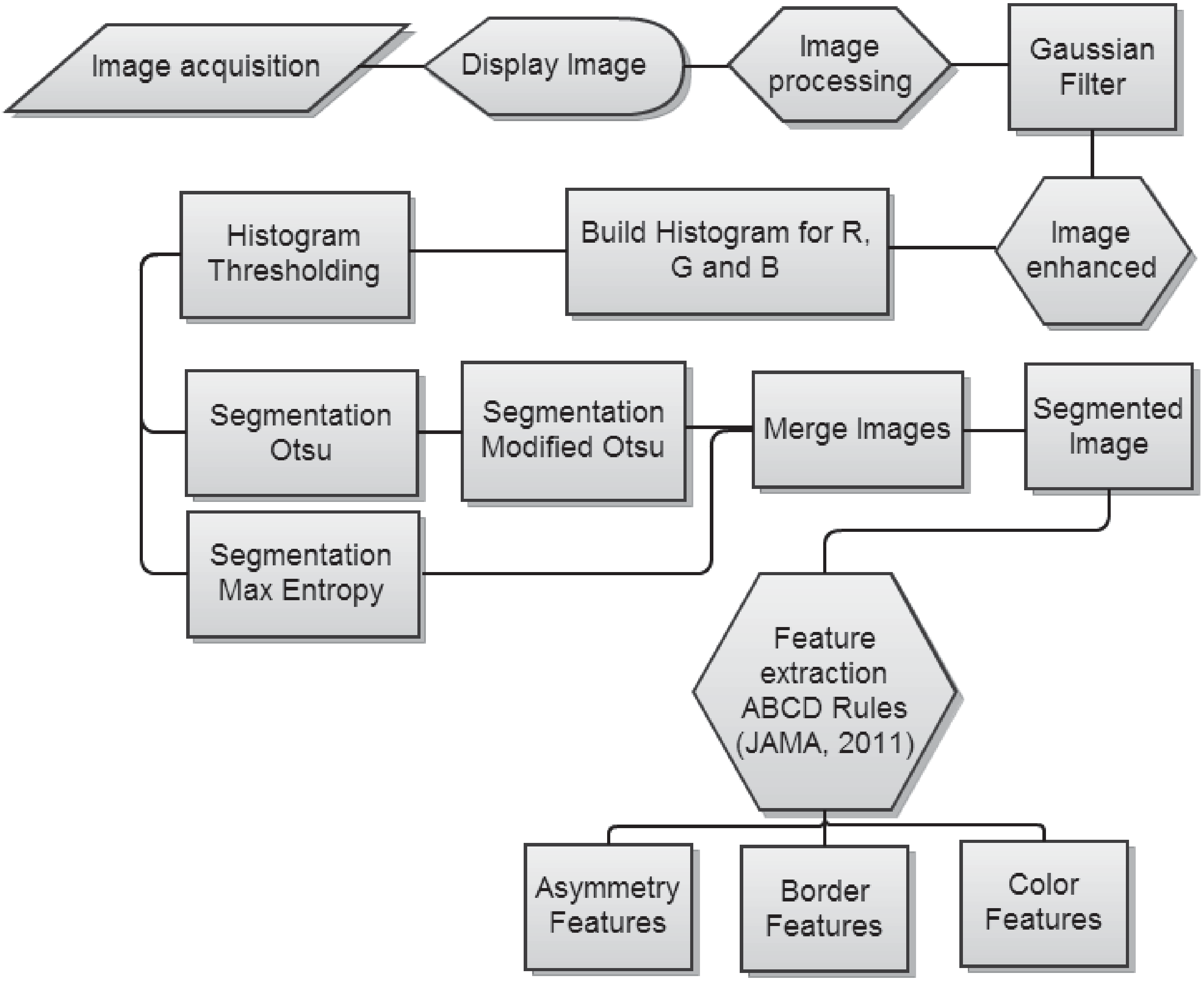

Figure 3.7: *Flow chart of the skin cancer classification application*

3.3.4 Image processing

There are different methods to reduce noise and improve the quality of the image such as smoothing, median filters, mean filters, Gaussian filters, gamma correction, or histogram equalization (Maglogiannis & Doukas, 2009). Normally noise is assumed to follow a Gaussian distribution (Alcón et al., 2009). Therefore a Gaussian filter was applied in the three coordiantes of the image to reduce noise. A 2D Gaussian kernel is specified as:

$$G(x,y,\sigma) = \frac{1}{2\pi\sigma^2} e^{-\frac{x^2+y^2}{2\sigma^2}} \tag{3.1}$$

σ determines the width of the Gaussian kernel. In this research the value of $\sigma = 2$.

3.3.5 Histogram based thresholding and segmentation

The skin images containing tumors (benign or cancerous) always have certain portion of skin on the background. It is necessary to segment the skin background from tumor for further analysis and classification of images.

3.3.5.1 Histogram

A histogram is a probability distribution of an image. Let's have $L \in 0 \dots 255$ bins. An 8-bit image has N pixels with pixel intensity levels in the range of $I(x,y) \in 0 \dots 255$. Therefore the probability to find the pixel intensity level i is:

$$p_i = \frac{n_i}{N} \tag{3.2}$$

$$\sum_{i=0}^{L} p_i = 1 \tag{3.3}$$

Where n_i is the number of pixels with the intensity level i in the image.

The thresholding techniques utilized in this research are based on the histogram of the image. Therefore, the histograms for each color coordinate (red, green, and blue) are used.

3.3.5.2 Moments

Moments are a mathematical concept that can be understood as a quantitative characteristic of a probability distribution. For instance, the moment of order one m_1 represents the mean of the distribution. The central moment of order two represents the variance. Mathematically a moment of order i of a continuous function of a real variable is defined as (Keyes & Winstanley, 2001):

$$m_i = \int_{-\infty}^{\infty} x^i f(x) dx \tag{3.4}$$

Central moment of order i is defined as:

$$\mu_i = \int_{-\infty}^{\infty} (x - m_1)^i f(x) dx \tag{3.5}$$

The representation of the moments of a discrete function is:

$$m_i = \sum_{x} x^i f(x) \tag{3.6}$$

$$\mu_i = \sum_x (x - m_1)^i f(x) \tag{3.7}$$

Image moments use the same principle but extended to 2 dimensions. Thus the moment of order $p + q$ of a 2D continuous function of real values is defined as:

$$m_{pq} = \int_{-\infty}^{\infty} \int_{-\infty}^{\infty} x^p y^q f(x, y)\, dx\, dy \tag{3.8}$$

And the digital representation is

$$m_{pq} = \sum_x \sum_y x^p y^q f(x, y) \tag{3.9}$$

The centroid of the image is obtained by:

$$\bar{x} = \frac{m_{10}}{m_{00}} \tag{3.10}$$

$$\bar{y} = \frac{m_{01}}{m_{00}} \tag{3.11}$$

There are other moments that are descriptive for shapes and they are invariant to scaling, translation, or even rotation. Those moments are known as normalized central moments and seven Hu Moments (Burger & Burge, 2010). To obtain these moments it is necessary to introduce image central moments. The central moment for a 2D continuous function of real values is defined as:

$$\mu_{pq} = \int_{-\infty}^{\infty} \int_{-\infty}^{\infty} (x - \bar{x})^p (y - \bar{y})^q f(x, y)\, dx\, dy \tag{3.12}$$

And its digital representation is

$$\mu_{pq} = \sum_x \sum_y (x - \bar{x})^p (y - \bar{y})^q f(x, y) \tag{3.13}$$

The central moments of the order 3 or less can be expressed as:

$$\mu_{00} = M_{00} \tag{3.14}$$

$$\mu_{11} = M_{11} - \bar{y}\, M_{10} \tag{3.15}$$

$$\mu_{10} = 0 \tag{3.16}$$

$$\mu_{01} = 0 \tag{3.17}$$

$$\mu_{20} = M_{20} - \bar{x} M_{10} \tag{3.18}$$

$$\mu_{02} = M_{02} - \bar{y} M_{01} \tag{3.19}$$

$$\mu_{30} = M_{30} - 3\bar{x} M_{20} + 2\, \bar{x}^2 M_{10} \tag{3.20}$$

$$\mu_{03} = M_{03} - 3\bar{y} M_{02} + 2\, \bar{y}^2 M_{01} \tag{3.21}$$

$$\mu_{12} = M_{12} - 2\bar{y} M_{11} - \bar{x} M_{02} + 2\, \bar{y}^2 M_{10} \tag{3.22}$$

$$\mu_{21} = M_{21} - 2\bar{x} M_{11} - \bar{y} M_{20} + 2\, \bar{x}^2 M_{01} \tag{3.23}$$

Central moments are normalized to calculate the seven Hu Moments. These normalized central moments are useful because they are invariant to scaling and translation, meaning that for instance two images with a circle of different size will have the same normalized central moments (Burger & Burge, 2010).

$$\eta_{pq} = \frac{\mu_{pq}}{\mu_{00}^{\gamma}} \tag{3.24}$$

Where $\gamma = \left(\frac{1}{2}(p + q)\right) + 1$

Hu Moments are 7 moments set out by Hu (Hu, 1962) which were proved to be invariant for translation, scaling and rotation. These moments can be represented as:

$$Hu_1 = \eta_{20} + \eta_{02} \tag{3.25}$$

$$Hu_2 = (\eta_{20} + \eta_{02})^2 + 4\eta_{11}^2 \tag{3.26}$$

$$Hu_3 = (\eta_{30} - 3\eta_{12})^2 + (\eta_{03} + 3\eta_{21})^2 \tag{3.27}$$

$$Hu_4 = (\eta_{30} - \eta_{12})^2 + (\eta_{03} + \eta_{21})^2 \tag{3.28}$$

$$\begin{aligned} Hu_5 = (3\eta_{30} - 3\eta_{12})(\eta_{30} + \eta_{12})[(\eta_{30} + \eta_{12})^2 \\ - 3(\eta_{21} + \eta_{03})^2] \\ + (3\eta_{21} - \eta_{03})(\eta_{21} + \eta_{03}) * [3(\eta_{30} + \eta_{12})^2 \\ - (\eta_{21} + \eta_{03})^2] \end{aligned} \tag{3.29}$$

$$\begin{aligned} Hu_6 = (\eta_{20} - \eta_{02})[(\eta_{30} + \eta_{12})^2 - (\eta_{21} + \eta_{03})^2] \\ + 4\eta_{11}^2(\eta_{30} + \eta_{12})(\eta_{21} + \eta_{03}) \end{aligned} \tag{3.30}$$

$$\begin{aligned} Hu_7 = (3\eta_{21} - \eta_{03})(\eta_{30} + \eta_{12})[(\eta_{30} + \eta_{12})^2 \\ - 3(\eta_{21} + \eta_{03})^2] \\ + (3\eta_{12} - \eta_{30})(\eta_{21} + \eta_{03}) * [3(\eta_{30} + \eta_{12})^2 \\ - (\eta_{21} + \eta_{03})^2] \end{aligned} \tag{3.31}$$

3.3.5.3 Histogram thresholding methods

Histogram thresholding segmentation algorithms work when there is a clear separation between the pixels corresponding to the object and the pixels corresponding to the background. In general the histograms obtained from the skin images had two different peaks. The smallest and darkest peak tended to be the mole and the biggest and brightest peak tended to be the background. Therefore, the goal of histogram threshold is to find intensity level k ($k \in 0 \dots 255$) that separates the two classes (background and object).

Artifacts (i.e. hair, freckles) and noise impact in the result of the segmented image. Noise is already reduced after applying the Gaussian filter, but artifacts are still present on the image. Reducing them is outside of scope for this research. Therefore, the images with bad segmentation results are discarded from further analysis and classification.

In the literature there are many algorithms that have been used for histogram-based segmentation. In this research 3 histogram-based thresholding methods are selected:

1. Otsu’s Thresholding, (Otsu, 1979)
2. Modified Otsu’s (Panigrahi, Misra, Bern, & Marley, 1995)
3. Max Entropy (Kapur, Sahoo, & Wong, 1985)

Figure 3.8 shows the flow chart for histogram-based thresholding.

3.3.5.3.1 Otsu´s Thresholding

Otsu’s thresholding is an unsupervised thresholding method and its goal is to find the grey level which maximizes the separability of the two classes (background and object) (Otsu, 1979). The ideal case for Otsu´s is when the image histogram presents two peaks separated by a deep valley.

The image histogram is separated in 2 classes with a threshold $k \in 0 \ldots 255$. Otsu´s searches k which better separates the two classes in the histogram. G_b and G_o are the class for background and for object respectively. Therefore the probability of occurrence of each class is given by:

$$w_0 = P(G_b) = \sum_{i=0}^{k} p_i = w(k) \qquad (3.32)$$

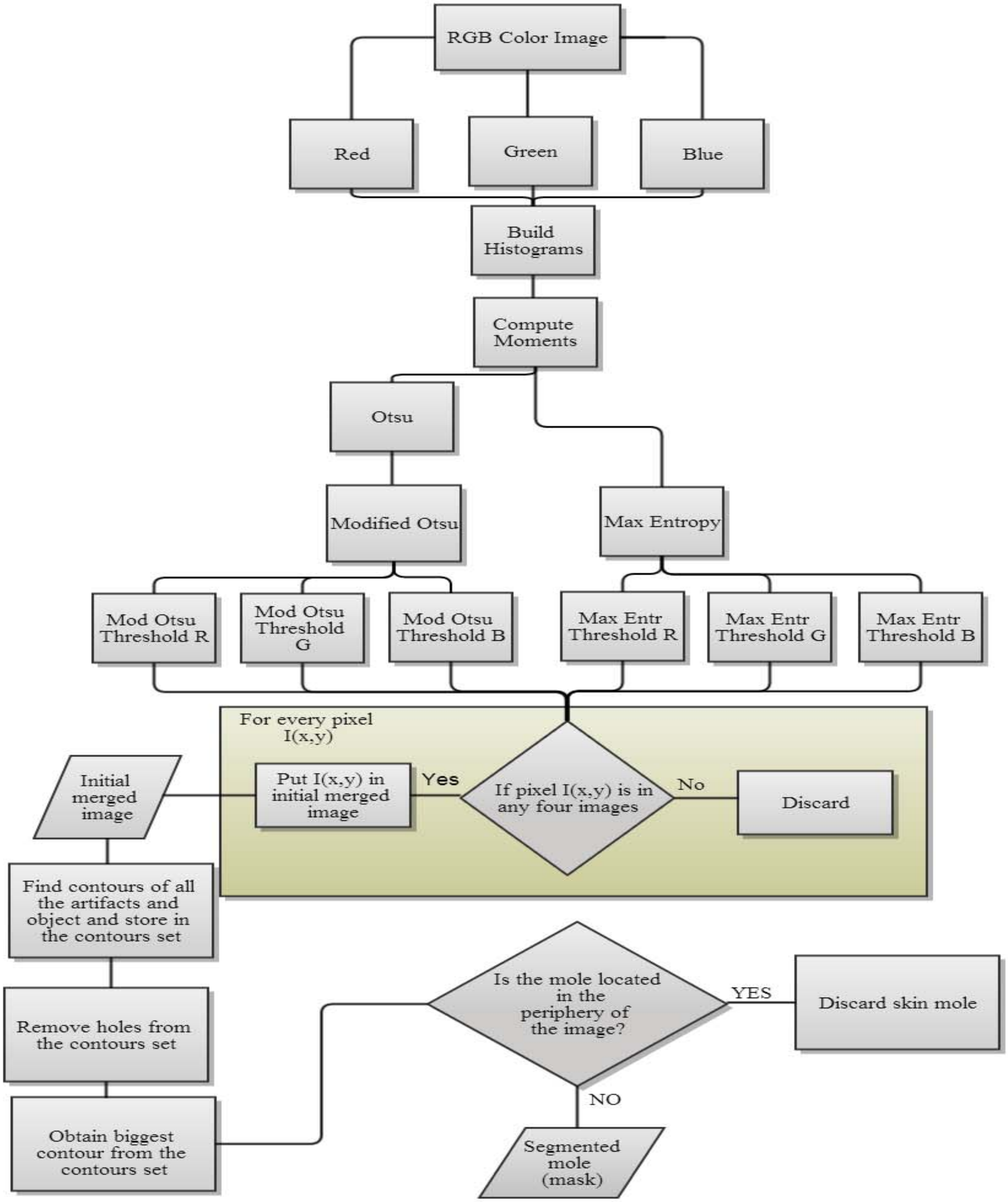

Figure 3.8: *Histogram-based thresholding*

Notice the use of the moment of order zero in equation 3.32.

$$w_1 = P(G_o) = 1 - w_0 = 1 - w(k) \tag{3.33}$$

The best separation is obtained by maximizing the between class variance which is found by equation 3.34:

$$\sigma_B^2 = w_0 w_1 (\mu_1 - \mu_0)^2 \tag{3.34}$$

$$\mu_0 = \sum_{i=0}^{k} i\, P(i|G_b) = \sum_{i=0}^{k} i \frac{p_i}{w_0} = \frac{\mu(k)}{w(k)} \tag{3.35}$$

$$\mu_1 = \sum_{i=k+1}^{L} i\, P(i|G_o) = \sum_{i=0}^{k} i \frac{p_i}{w_1} = \frac{\mu_T - \mu(k)}{1 - w(k)} \tag{3.36}$$

Where μ_T is the overall mean of the histogram. $\mu(k)$ is obtained using the moment of order one:

$$\mu(k) = \sum_{i=0}^{k} i\, p_i \tag{3.37}$$

The implementation of Otsu's thresholding is very efficient because of the use of moments. First it is necessary to compute the overall mean of the histogram. Therefore it is computed the first moment of the histogram. Afterwards, it is computed at each iteration the probability of occurrence of each class w_0 and w_1, the mean μ_0 and μ_1, and the between class variance σ_B. At each iteration the obtained σ_B is checked if it is bigger than the maximum $Max\ \sigma_B$ stored from the past iterations. If it is bigger, it is stored. Finally, the associated k to $Max\ \sigma_B$ is the Otsu´s threshold.

3.3.5.3.2 Modified Otsu´s

Modified Otsu is a variant of Otsu´s thresholding algorithm which works very well when the object is composed of more than one main color (Panigrahi et al., 1995). For instance, melanomas often have different colors in the border. Otsu´s would mark the threshold in some region between the background and the border. In these cases, Modified Otsu adjusts dynamically the previous Otsu´s threshold k in the real limit of the border. The details of the algorithm are mentioned in (Panigrahi et al., 1995). Briefly, the algorithm further searches for another threshold after obtaining the threshold using Otsu's method. It uses probability theory with image distribution values and focuses on minimizing the error of classification. This algorithm selects the final threshold based on user selected parameter as a function of cumulative probability distribution. In this study a value of 0.4 is used.

In this research, Otsu´s threshold k is calculated first. Afterwards Modified Otsu´s threshold $k´$ is computed.

3.3.5.3.3 Max Entropy

The third thresholding algorithm evaluated is Max Entropy segmentation method. This segmentation utilizes the principle of Shannon Entropy (Kapur et al., 1985)

$$H = -\sum_{i=0}^{L} p_i \log(p_i) \tag{3.38}$$

The histogram is separated in two classes, G_b and G_o which are background and object respectively. The best threshold is located where the sum of entropies for G_b and G_o is maximum.

$$H_{G_b} = -\sum_{i=0}^{k} \frac{p_i}{w_0} \log\left(\frac{p_i}{w_0}\right) \tag{3.39}$$

$$H_{G_o} = -\sum_{i=k+1}^{L} \frac{p_i}{w_1} \log\left(\frac{p_i}{w_1}\right) \tag{3.40}$$

$$Max\ entropy = \max\left(H_{G_b} + H_{G_o}\right) \tag{3.41}$$

The implementation of Max Entropy histogram thresholding method is ported from M. Emre Celebi's fourier routines (Celebi, 2013).

3.3.5.4 Merging the results

Red, green and blue coordinates of the original image are segmented using both Modified Otsu's and Max Entropy methods individually. This process creates six different segmented images. Each segmented image contains object information, labeled as 255, the background information is labeled with value of 0. These segmented images are:

1. Modified Otsu´s red segmentation
2. Modified Otsu´s green segmentation
3. Modified Otsu´s blue segmentation
4. Max Entropy red segmentation
5. Max Entropy green segmentation

6. Max Entropy blue segmentation

The following logic is used to merge these six obtained images:

1. For each pixel $I(x, y)$, $I(x, y)$ is compared in the six images.
2. If $I(x, y)$ is equal to 255 for any four images, the pixel belongs to the object
3. Repeat step 1 and step 2 for all the pixels, from left to right and top to bottom.
4. This process result is called initial merged image.

In practice, this initial merged image might have random artifacts surrounding the object "mole". So to reduce the artifacts the following procedure is used:

1. Find all the contours of all the artifacts and the object. To determine the contours the algorithm developed by Suzuky and Abe (1985) in OpenCV environment is used. Briefly, the algorithm creates a hierarchical data structure where the parent consists of all the external border points of all the shapes present in the image, and the children represent the existing holes inside all the shapes. An external border is defined as the border which its points are connected with the frame S. The frame S is further defined as the set of points which belong to the background with pixel values 0 and the background is connected with the periphery of the image.
2. The holes are removed from the set, if any, from the data structure.
3. The biggest set of points are obtained next. It is assumed that the mole is the biggest shape.
4. It is also verified that the mole is not located in the periphery of the image. If at all the segmented region includes the periphery of the image, then there is an error, and the result is discarded.

The final result of the merging operation is the segmented mole which is used as a mask in further operations (object information labeled as 255, and background information labeled as 0).

3.3.6 Feature extraction

The features extracted for the skin cancer smartphone application follow the ABCD melanoma diagnosis rules introduced in chapter 2, (JAMA, 2011). The features are divided into three groups: color features, asymmetry features and border features.

3.3.6.1 Color coordinate conversion

In skin images, color is an important attribute. Color images are represented with a variety of color coordinate systems (Burger & Burge, 2010); of those, HSV is a popular coordinate system. It was used HSV because it separates the color information from the illumination and saturation information.

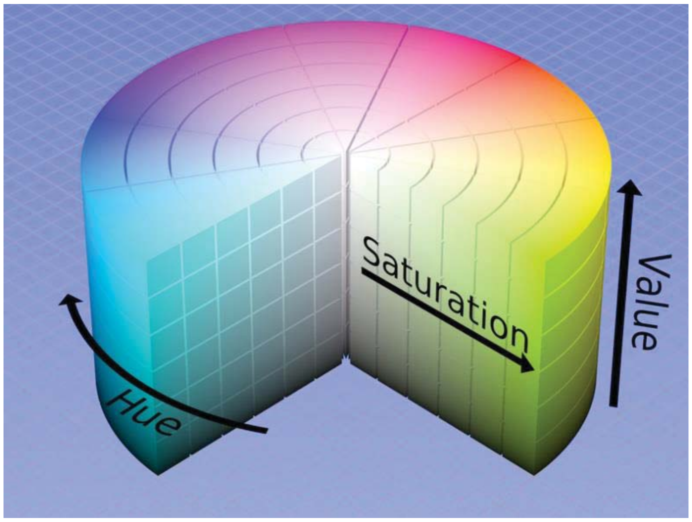

Figure 3.9: *HSV Cylinder representation (Shark. D, 2009).*

In Figure 3.9, HSV color coordinate system is represented as a cylinder (Burger & Burge, 2010). The Hue coordinate represents the color, whereas saturation indicates the dominance of hue in the color. Value describes the intensity of the light, how dark or bright is the color. In “OpenCV”, the image values are stored in 8-bit variables. Therefore, the range of Hue goes from 0 to 179 degrees and Saturation and Value coordinates’ ranges are from 0 to 255. Notice in Figure 3.9 that if Value coordinate is close to 0, the color is black; therefore the values of Hue and Saturation are meaningless.

The following equations introduces the relationship between RGB color space and HSV used by OpenCV (Itseez, 2013). Given a pixel in 8-bit RGB color image $I(x, y)$, the coordinates R, G and B must be scaled between 0 and 1:

$$R' = \frac{R}{255} \tag{3.42}$$

$$G' = \frac{G}{255} \tag{3.43}$$

$$B' = \frac{B}{255} \tag{3.44}$$

Then the maximum and minimum from the three coordinates are obtained to compute the values for Saturation and Value coordinates:

$$\max = Max(R', G', B') \tag{3.45}$$

$$\min = Min(R', G', B') \tag{3.46}$$

$$S = \frac{\max - \min}{max} \tag{3.47}$$

$$V = max \tag{3.48}$$

If Saturation is 0, then the color is monochrome, therefore corresponding Hue pixels are meaningless.

If Value is 0, then the color is black, therefore corresponding Hue and Saturation pixels are meaningless.

If $Max = R'$, then

$$H = \frac{60(G' - B')}{V - min} \tag{3.49}$$

If $Max = G'$, then

$$H = 120 + \frac{60(G' - B')}{V - min} \tag{3.50}$$

If $Max = B'$, then

$$H = 240 + \frac{60(R' - G')}{V - min} \tag{3.51}$$

$$if\ H < 0\ then\ H = H + 360 \tag{3.52}$$

If H is negative, 360 is added to the previous value to obtain a positive Hue value.

Finally, the values for the three coordinates are scaled accordingly the value ranges indicated previously:

$$H = \frac{H}{2} \tag{3.53}$$

$$Saturation\ value = S * 255 \tag{3.54}$$

$$Value\ value = V * 255$$

OpenCV implements an RGB to HSV conversion using the previous equations.

3.3.6.2 Color feature extraction

HSV color coordinates is used to extract color information. Therefore, the segmented image is converted from RGB to HSV using the process explained in the previous section. Figure 3.10 illustrates the flow chart for color feature extraction. Figure 3.11 presents the process to extract color information from the Hue, Saturation and Value coordinates using the four location image regions.

Parameters in detecting melanoma are homogeneity and variation of color in HSV coordinate. In order to characterize the variation of color, region growing algorithm is used to create four predefined regions. However, the Hue coordinate is shifted 90 degrees to move the green to the end of the Hue distribution, because the region growing algorithm must identify the two parts of red (0 and 180) as the same region. Otherwise, region growing would assigned red colors in two completely different regions.

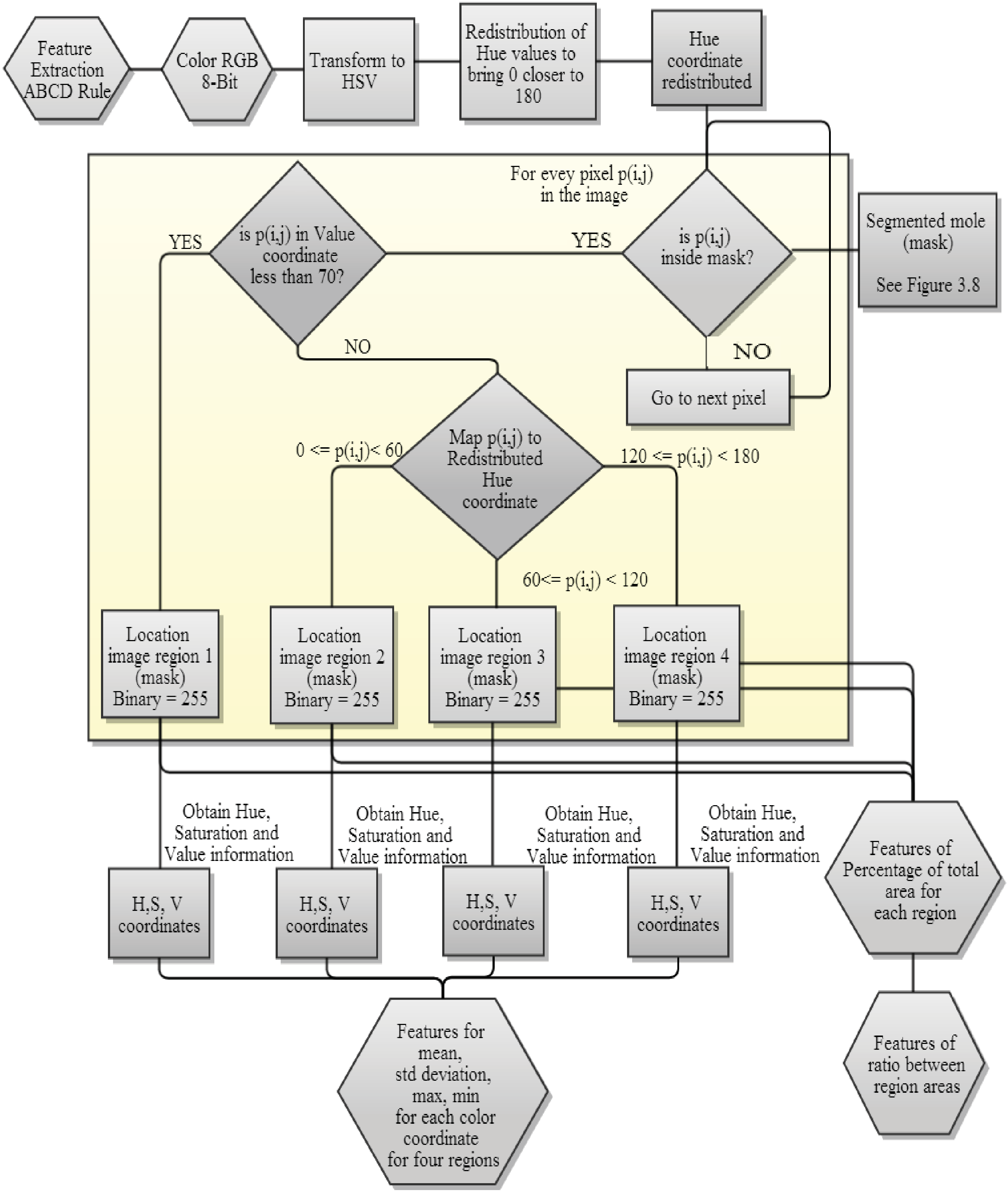

Figure 3.10: *Flow chart for color features extraction*

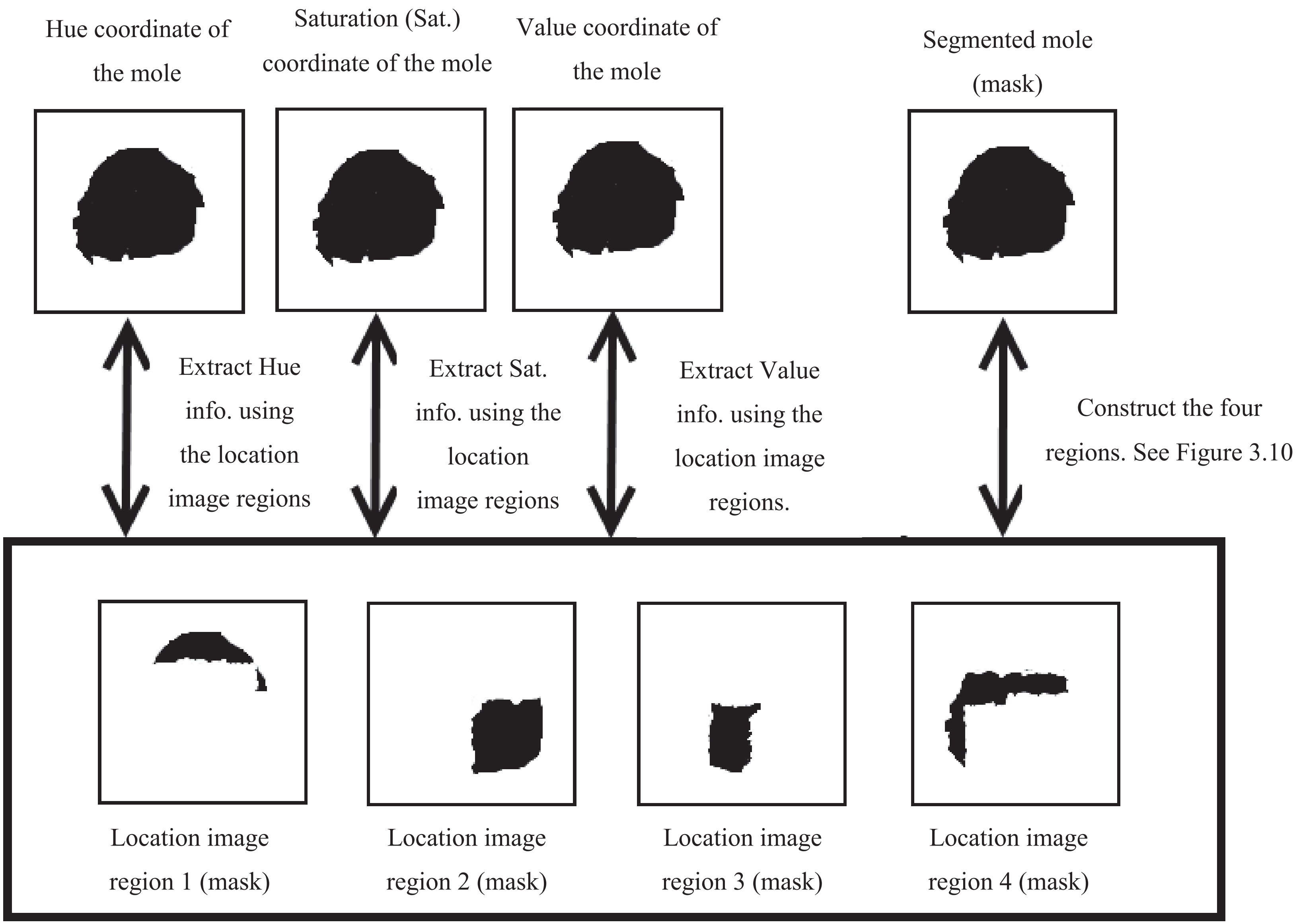

Figure 3.11: *Diagram of color feature extraction color mapping*

The algorithm for shifting is as follow. Given $H(x, y)$ an intensity value in Hue color coordinate, the redistribution is performed following equation 3.55:

$$\begin{gathered} if\ I(x, y) \geq\ 90\ then \\ I(x, y) = (I(x, y) + 90)\ mod\ 180 \\ else\ I(x, y) = I(x, y) + 90 \end{gathered} \tag{3.55}$$

The result of shifting Hue coordinate is called Hue coordinate redistributed.

Once the Hue coordinate is redistributed, the region growing algorithm starts iterating all the pixels in the skin mole. For each pixel $p(i, j)$ in the skin mole it is checked if it belongs to the mole. To know if $p(i, j)$ is inside the mole it is used the image Segmented mole obtained in the previous operation of merging the images. Therefore, if $p(i, j)$ is inside the mole, then it is checked at which region $p(i, j)$ belongs following the next criteria:

- If $p(i, j)_V$ in the Value coordinate is less than 70, then $p(i, j)$ belongs to region 1. Therefore, in the coordinate (i, j) in the mask used for region 1, called Location image region 1, is set to 255.
- Else, if $0 \leq p(i, j)_H < 60$ in the Hue coordinate, then $p(i, j)$ belongs to region 2. Therefore, in the coordinate (i, j) in the mask used for region 2, called Location image region 2, is set to 255.
- Else, if $60 \leq p(i, j)_H < 120$ in the Hue coordinate, then $p(i, j)$ belongs to region 3. Therefore, in the coordinate (i, j) in the mask used for region 3, called Location image region 3, is set to 255.

- Else, if $120 \leq p(i,j)_H < 180$ in the Hue coordinate, then $p(i,j)$ belongs to region 4. Therefore, in the coordinate (i,j) in the mask used for region 4, called Location image region 4, is set to 255.

Once the four Location image regions are obtained, the color information is extracted. For each region $i \in 1,2,3,4$, it is obtained all those pixel values from Hue, Saturation and Value coordinates which have a pixel correspondence in the Location image region i. See Figure 3.11.

Afterwards, for each region and for each color coordinate it is computed the following parameters. See Table 3.2 for the list of color features:

- Mean, standard deviation, maximum and minimum

Moreover, percentage of total area of the mole for each region is obtained following equation 3.56:

$$Percentage\ of\ total\ area\ of\ the\ mole\ in\ Region_i = \frac{Number\ pixels\ in\ Region_i}{Area\ mole} \tag{3.56}$$

$$i \in \{1,2,3,4\}$$

Finally, it was computed the ratio of percentage of areas for each region as follow:

$$ratio\ area = \frac{Area\ Region_i}{Area\ Region_j}\quad i \neq j \tag{3.57}$$

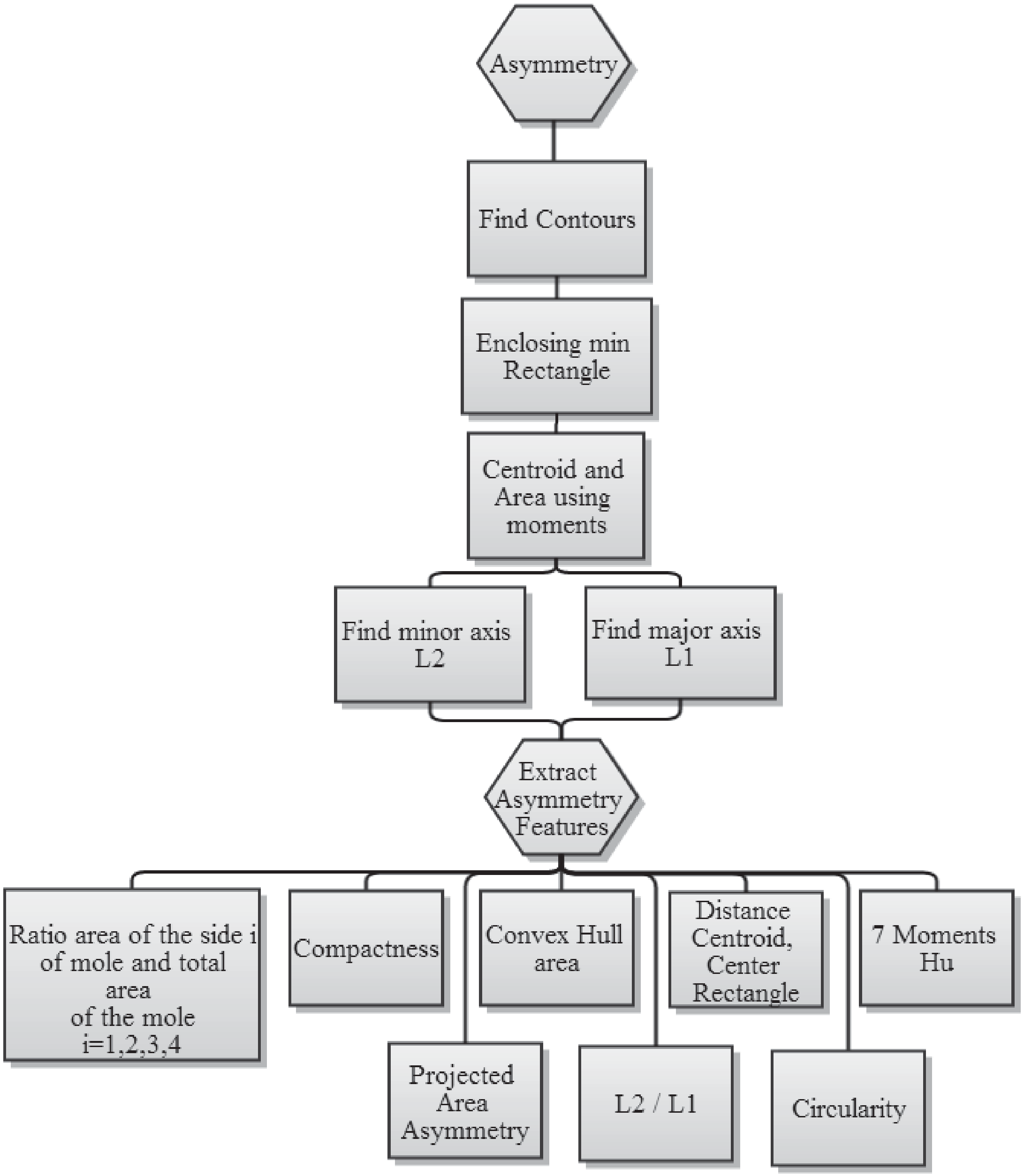

Figure 3.12: *Flow chart for asymmetry feature extraction*

3.3.6.3 Asymmetry feature extraction

Figure 3.12 illustrates the flow chart to extract asymmetry features. This process does not need color information. Therefore a binary image is used with a closed shape. Its background pixels have value of 0 and object pixels have value of 255.

In order to extract asymmetry features, it is necessary to compute the contours of the image and the minimum area enclosing rectangle (bounding box) of the mole. The contours are obtained using Freeman Chain Code, FCC, an algorithm that needs one starting point and a chain code to reconstruct the full border. A modification of the conventional Chain Code algorithm is outlined as follows (Freeman, 1974):

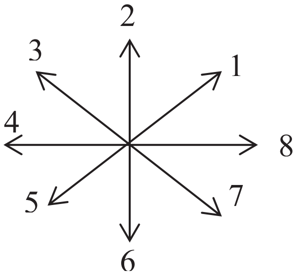

Figure 3.13: *FCC´s possible directions*

1. Select a point which is known to be inside the shape, and assign the component x of the point to 0. $Point\ p(x,y) \rightarrow p'(0,y)$.
2. Move from left to right until the initial border point, $P_{initial}(x,y)$ is found
3. Initiate the search (Chain Code), starting in direction four, in anti-clockwise direction. See Figure 3.13.
4. Find direction code of the present border point
5. Find its opposite direction

6. Add 1 to the direction
7. Repeat step 4, 5 and 6 until you find $P_{initial}(x, y)$.

The contours of the mole are used to obtain the bounding box. It is used the OpenCV's inbuilt method $minAreaRect$ which returns a rectangle enclosing the entire shape. Further details of the algorithm can be found in Freeman and Shapira's algorithm (1975). A brief outline of this algorithm is as follows:

Two principal axes (L1 and L2) are constructed using the bounding box. Major axis L1 bisects the bounding box longitudinally and minor axis L2 is a perpendicular axis from L1. Given a rotated rectangle r with center $p(x, y)$, width w , height h and angle α, L1 and L2 are obtained as follows:

$$L1[0] = Point\left(x + \frac{h}{2} * \cos(\alpha), y + \frac{h}{2} * \sin(\alpha)\right) \tag{3.58}$$

$$L1[1] = Point\left(x - \frac{h}{2} * \cos(\alpha), y - \frac{h}{2} * \sin(\alpha)\right) \tag{3.59}$$

$$L2[0] = Point\left(x + \frac{w}{2} * \cos(90 + \alpha), y + \frac{w}{2} * \sin(90 + \alpha)\right) \tag{3.60}$$

$$L2[1] = Point\left(x - \frac{w}{2} * \cos(90 + \alpha), y - \frac{w}{2} * \sin(90 + \alpha)\right) \tag{3.61}$$

For each principal axis, two sides of the shape are created. These two sides for each axis have either pixels corresponding to the object or pixels corresponding to the background.

3.3.6.3.1 Computation of the centroid

The centroid of the shape is calculated using M_{10}, M_{01} and M_{00} moments. The centroid point is located in:

$$(\bar{x}, \bar{y}) = \left(\frac{M_{10}}{M_{00}}, \frac{M_{01}}{M_{00}}\right) \tag{3.62}$$

3.3.6.3.2 Computation of the asymmetry features

The following asymmetry features are obtained:

1. Circularity:

$$Circularity = \frac{\sigma_R}{\mu_R} \tag{3.63}$$

Where μ_R and σ_R are the mean and standard deviation of the distance from the centroid to all the border points of the mole (Montero & Bribiesca, 2009). A perfect circle will have circularity value of 0. Therefore the bigger the value the less circular it is:

2. Compactness:

$$Compactness = \frac{4 * \pi * Area}{Perimeter^2} \tag{3.64}$$

The perimeter is obtained using the contours. It is used an inbuilt method from OpenCV:

$$\begin{aligned} &Perimeter \\ &= (\#\ of\ connections\ not\ diagonal\ ) \\ &+ \left(\#of\ connections\ in\ diagonal * \sqrt{2}\ \right) \end{aligned} \tag{3.65}$$

The area is obtained using the moment M_{00}. Compactness is multiplied by $4 * \pi$ to obtain a range between 0 and 1.

3. Ratio of principal axes

$$Ratio = \frac{L_1}{L_2} \tag{3.66}$$

4. Ratio of the area of the mole and the area of the bounding box.

$$Ratio\ Area = \frac{Area\ of\ the\ mole}{area\ of\ the\ bounding\ box} \tag{3.67}$$

5. Ratio of the area of the one side of the principal axes $L1$ or $L2$ and the total area of the mole.

$$Ratio\ Asymmetry_k = \frac{Area_{Li,j}}{Total\ Area\ of\ the\ mole}$$
$$i\ is\ L1\ or\ L2, \in \{1,2\} \tag{3.68}$$
$$j\ is\ left\ or\ right\ side \in \{1,2\}$$

6. Ratio of area of convex Hull and area of the mole

$$Ratio\ Hull\ area = \frac{Area\ of\ the\ mole}{Area\ of\ the\ convex\ hull} \tag{3.69}$$

   The convex Hull was obtained using an inbuilt OpenCV method.

7. Distance between the centroid of the mole and the center of the bounding box.
8. Seven Hu moments which are invariant to scaling, translation and rotation.
9. Ratio of the difference of the correspondence pixels of the sides of L1 or L2 and the total area of the mole. The goal of this feature was to determine the number of pixels which were not symmetrical. That is, all these pixels in one side of the mole which do not have a correspondence in the other side of the mole. Therefore, it was necessary to mirror one side of the mole in order to be able to compare it with the other side. The algorithm’s outline to compare the difference area in pixel correspondence using L1 is as follows:

i) Rotate the bounding box to obtain a new rectangle with 0 degree with respect to x-axis.

ii) Copy the two sides of the mole in a two new images of the size of each side.

iii) Flip the right side of L1 to the left. Given an image I of the right side of L1 the flip operation is performed for all the pixels. Max_x is maximum value of x found in the image:

$$FlipL1(x, y) = \ RightL1(Max_x - x, y\ ) \tag{3.70}$$

iv) Subtract the left side of L1 (LeftL1) to FlipL1

$$K = LeftL1 - FlipL1 \tag{3.71}$$

v) Obtain ratio

$$ratio = \frac{K}{Total\ area\ of\ the\ mole} \tag{3.72}$$

3.3.6.4 Border feature extraction

Figure 3.14 illustrates the flow chart for border feature extraction. The process to extract border features is developed as follow.

The border of the mole is extended 8 pixels. Therefore the process to construct the new border image is as follow:

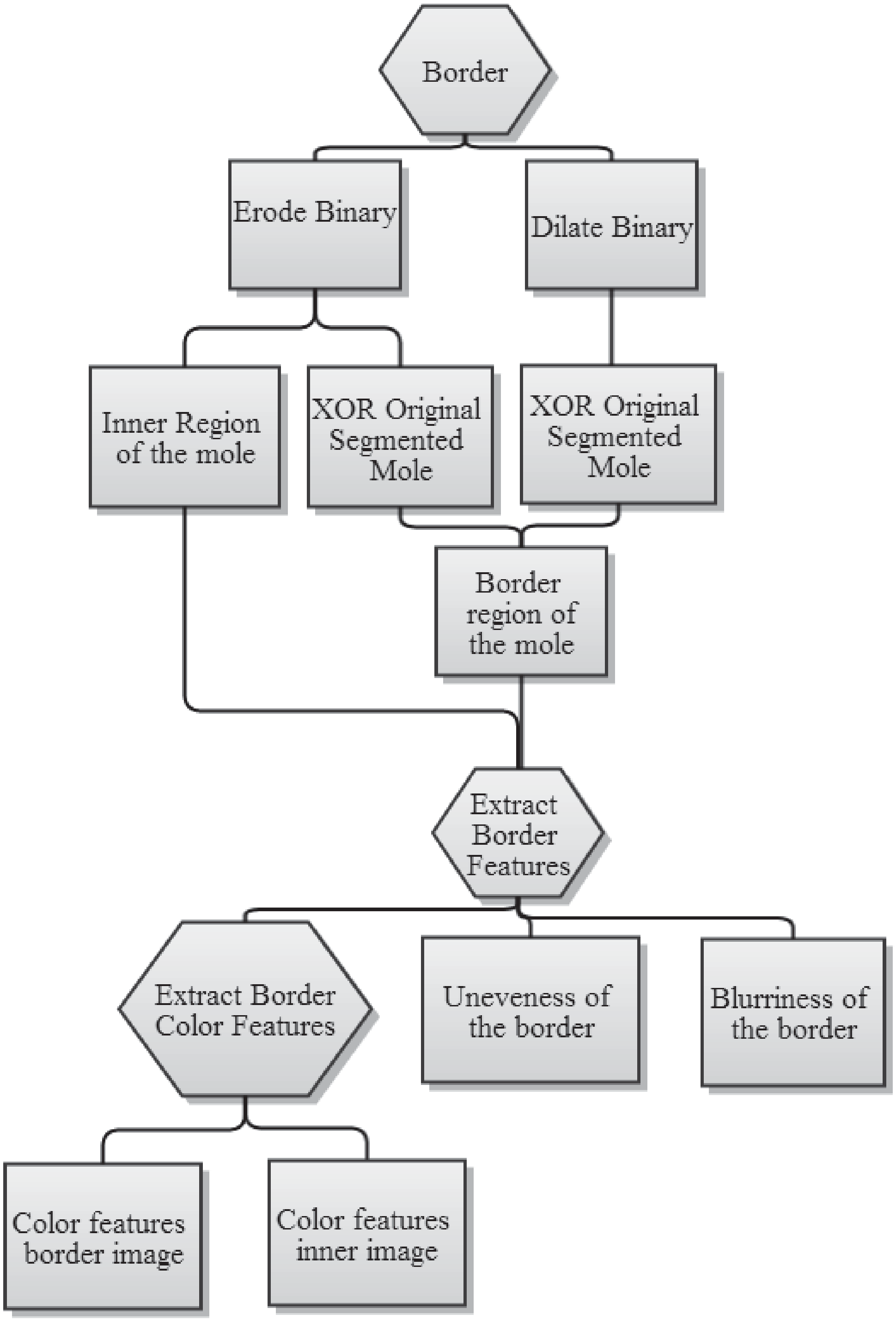

Figure 3.14: *Border features extraction flow chart*

1. Dilate the segmented image by four pixels. Dilation is a mathematical morphology operation which expands the region of the mole. Let S, a $3x3$ matrix, be the structuring element where all its elements are either 0 or 255. The dilation operation is defined as (Burger & Burge, 2010):

$$S = \begin{pmatrix} a_{11} & a_{12} & a_{13} \\ a_{21} & a_{22} & a_{23} \\ a_{31} & a_{32} & a_{33} \end{pmatrix} \tag{3.73}$$

$$I_{dilated} = I \oplus S \equiv \{(i+s) \mid for\ every\ point\ i \in I\ and\ point\ s \in S\} \tag{3.74}$$

   Therefore, the dilation process produces a new image which have all the possible combinations of points between I and S.

2. Erode the segmented image four pixels. Erosion is the complementary operation of the dilatation. In this operation, the binary shape is shrunk by four pixels. The operation is defined as (Burger & Burge, 2010):

$$I_{eroded} = I \ominus S = \{i \in \mathbb{Z}^2 \mid (i+s) \in I, for\ every\ s \in S\} \tag{3.75}$$

   Therefore, a point i is only included in the set of points of the erosion, if and only if the structuring element S, when lying in some point i, is totally inside the points of the shape of the image I.

3. Use a XOR operation between the dilated image and the original segmented image. The result obtained is the four pixel wide outer border.

$$I_{outer} = (I_{dilated})\ XOR\ (I_{original}) \tag{3.76}$$

4. Use a XOR operation between the eroded image and the original segmented image. The result obtained is the four pixel wide inner border.

$$I_{inner} = (I_{eroded})\ XOR\ (I_{original}) \tag{3.77}$$

5. Merge the outer border image with the inner border image. The operation for merging is a binary OR between the images

$$I_{border} = (I_{outer})\ OR\ (I_{inner}) \tag{3.78}$$

I_{border} becomes the binary border of the segmented mole. I_{eroded} becomes the binary inner region, I_{inner}, of the segmented mole.

3.3.6.4.1.1 Border color features

To characterize the color differences between border and inner region of the mole, the pixel points of I_{border} are mapped to the original RGB image creating a new RGB image of the border, $I_{colorborder}$, and the pixel points of $I_{inner}$are mapped to the original RGB image creating a new RGB image of the inner mole, $I_{colorinner}$. Afterwards, the same process explained in the section of color feature set extraction is applied. However, the image segmented mole used in the color feature set extraction as a mask is changed to the new image I_{border}. Statistical parameters are obtained for the four image regions for both $I_{colorborder}$ and $I_{colorinner}$.

3.3.6.4.1.2 Border unevenness features

Unevenness border features are extracted using Freeman Chain Code introduced previously. Each border pixel is assigned a direction code. For each direction code, the difference between the current direction code and the previous direction code is obtained. Therefore, the average in difference direction code is calculated for all the direction codes of the mole.

3.3.6.4.1.3 Border blurriness features

The blurriness of the border is characterized by computing the average and standard deviation of the border magnitude on the grey scale image, $I_{greyborder}$. Therefore, $I_{colorborder}$ is transformed from RGB to grey scale to obtain $I_{greyborder}$ using the inbuilt method of OpenCV for color conversion which uses the following equation:

$$\begin{aligned} I_{greyborder}(x,y) \\ &= (0.299)\cdot[\,I^{R}_{colorborder}(x,y)] + (0.587) \\ &\cdot[\,I^{G}_{colorborder}(x,y)] + (0.114) \\ &\cdot[\,I^{B}_{colorborder}(x,y)] \end{aligned} \tag{3.79}$$

Sobel edge detector operator is applied on $I_{greyborder}$ to obtain the edges. Sobel is a popular edge detector operator which uses the following kernel to convolve with the image:

$$Sobel\ operator\ for\ x\ domain$$

$$dx = \begin{pmatrix} 1 & 2 & 1 \\ 0 & 0 & 0 \\ -1 & -2 & -1 \end{pmatrix} \tag{3.80}$$

$$Sobel\ operator\ for\ y\ domain$$

$$dy = \begin{pmatrix} 1 & 0 & -1 \\ 2 & 0 & -2 \\ 1 & 0 & -1 \end{pmatrix} \tag{3.81}$$

$$Ix' = I \otimes dx \tag{3.82}$$

$$Iy' = I \otimes dy \tag{3.83}$$

After applying this kernel, two new images are obtained, $Ix'$and Iy'. The magnitude for a given pixel $Ix'(x, y)$ and $Iy'(x, y)$ is calculated by

$$Magnitude = \sqrt{Ix'(x,y)^2 + Iy'(x,y)^2} \tag{3.84}$$

The average and standard deviation border magnitude are obtained by computing the magnitude for all the pixels in $I_{greyborder}$

3.3.7 List of features

Tables 3.2, 3.3 and 3.4 illustrate the list of features used in this research. In total 197 features are extracted.

3.3.8 Feature analysis

It is necessary to conduct a statistical analysis of each feature to detect which features could be more useful for the classifier.

The feature set analysis consists of obtaining the statistical distribution of every feature (mean, standard deviation, maximum and minimum) for each group (benign and malign) to understand the feature statistical distribution. The goal is not to find the best feature set, but to understand better the data obtained.

3.3.9 Classification of skin cancer images

In this research Support Vector Machine is chosen to be used as the classifier for skin cancer classification. Figure 3.15 shows the process of classification using Support Vector Machines and the extracted features.

3.3.9.1 Support Vector Machine

Support Vector Machines (SVM) is a supervised machine learning algorithm. Its goal is to find the hyper plane which separates with the maximum margin the two classification groups (melanomas and benign moles). A training data set is defined as a pair of $x_i - y_i$ where $x_i \in \mathbb{R}^n$ is the vector of n features for the training sample and $y_i \in (-1,1)$ is the group which belongs the sample i.

SVM requires the solution of the following equations (Cortes & Vapnik, 1995). Further details of SVM algorithm can be found in Cortes & Vapnik (1995):

$$\min_{w,b,\,\xi_i} \left(\frac{1}{2}\|n\|^2 + \mathrm{C}\sum_{i=0}^{n} \xi_i\right) \tag{3.85}$$

$$constraint\colon y_i(nx_i + b) \geq 1 - \xi_i \; and \; \xi_i \geq 0 \tag{3.86}$$

Table 3.2: (a) Color features list for each image region. (b) Area region percentages feature list.

(a)

Image region 1			**Image region 2**			**Image region 3**			**Image region 4**		
H	**S**	**V**	**H**	**S**	**V**	**H**	**S**	**V**	**H**	**S**	**V**
Mean	Mean	Mean	Mean	Mean	Mean	Mean	Mean	Mean	Mean	Mean	Mean
Std dev	Std dev	Std dev	Std dev	Std dev	Std dev	Std dev	Std dev	Std dev	Std dev	Std dev	Std dev
Max	Max	Max	Max	Max	Max	Max	Max	Max	Max	Max	Max
Min	Min	Min	Min	Min	Min	Min	Min	Min	Min	Min	Min

(b)

Percentage area image region 1	Percentage area image region 2	Percentage area image region 3	Percentage area image region 4	area region 1 / area region 2
area region 1 / area region 3	area region 1 / area region 4	area region 2 / area region 3	area region 2 / area region 4	area region 3 / area region 4

Table 3.3: Asymmetry features list

Circularity	Compactness	Ratio of principal axes	Ratio melanoma area	Ratio of area side left L1
Ratio of area side right L1	Ratio of area side left L2	Ratio of area side right L2	Ratio of convex hull area	Distance centroid – center rectangle
Invariant moment 1	Invariant moment 2	Invariant moment 3	Invariant moment 4	Invariant moment 4
Invariant moment 6	Invariant moment 7	Correspondence Points in L1	Correspondence Points in L2	

Table 3.4: Border features list

Average magnitude of the border	Standard deviation magnitude of the border
Average of direction code change	Standard deviation of direction code change
Color features using the border image $I_{colorborder}$ illustrated in Table 3.2	Color features using the inner image of the mole $I_{innerborder}$ illustrated in Table 3.2

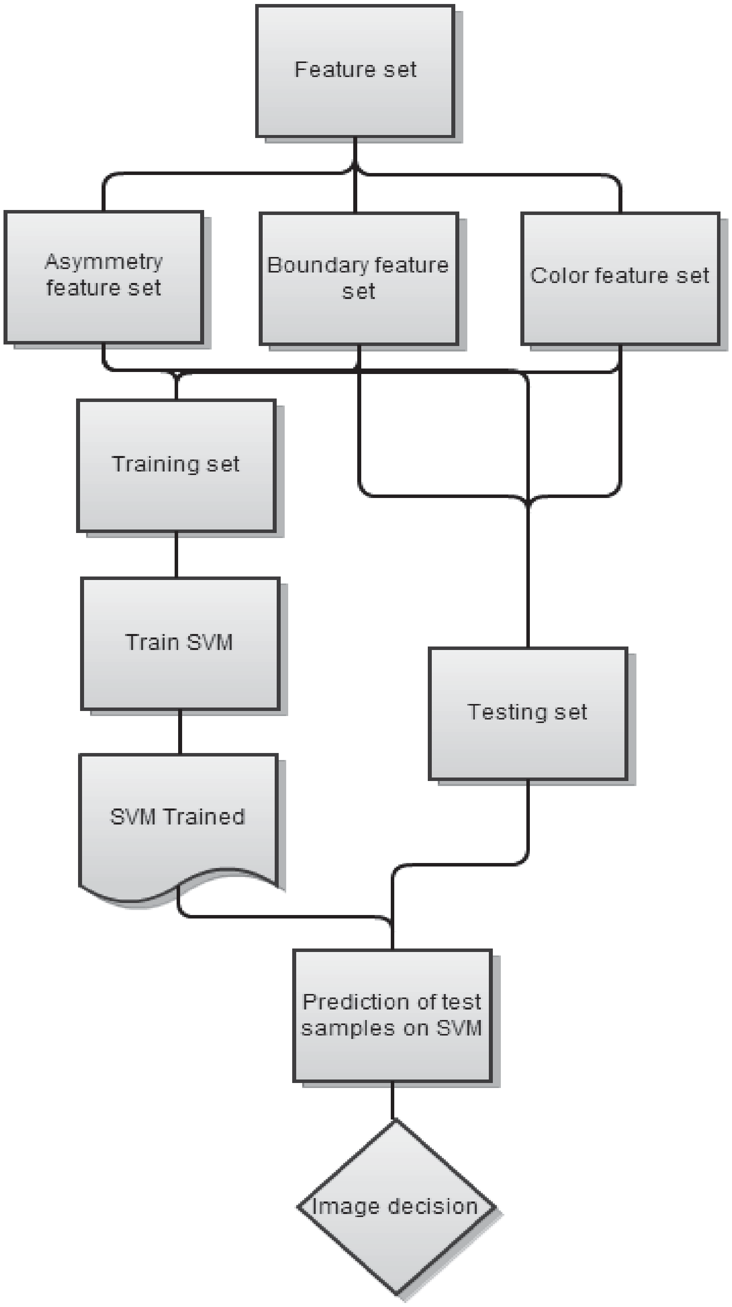

Figure 3.15: *Flow chart for the classification process*

Finally, it uses *the kernel trick* (Aizerman, Braverman, & Rozonoer, 1964), which maps the sample data into another higher dimensional space, for identifying a hyperplane which separates better the data. There are different kernels such as linear, polynomial, radial basis function (RBF) or sigmoid (Hsu, Chang, & Lin, 2010). There is no direct method to know which kernel is optimal for a given problem. Therefore, it is recommended to perform cross validation using all the possible kernels and then use the best one. However, due to limitations of time it is not possible to perform cross validation with all the possible kernels, because it requires finding optimal parameters for each kernel. Therefore, start with radial basis function is recommended because it adds only one extra parameter, and has at least the same performance as a linear kernel (Hsu et al., 2010). RFB kernel is defined as:

$$Kernel(x_i, y_i) = \exp(-\gamma \|x_i - y_i\|^2)\,, \gamma > 0 \tag{3.87}$$

Therefore, the configuration of the SVM classifier only requires two parameters, C and γ.

OpenCV uses a version of SVM based for the implementation of LibSVM (Fan, Chen, & Lin, 2005).

The results obtained with SVM are evaluated using three parameters simultaneously. These parameters are accuracy, sensitivity and specificity, defined as follow (Cavalcanti & Scharcanski, 2011):

$$Accuracy \; = \frac{Total\ images\ classified\ correctly}{Total\ testing\ images} x\ 100 \tag{3.88}$$

$$Sensitivity = \frac{Melanomas\ classified\ correctly}{Total\ testing\ meloma\ images}\ x\ 100 \tag{3.89}$$

$$Specificity = \frac{Control\ images\ classified\ correctly}{Total\ testing\ control\ images}\ x\ 100 \qquad (3.90)$$

For this study, our target for accuracy is 90%.

3.3.9.2 Training set of skin images

The dataset of skin cancer images consists of 291 images out of this 143 are melanomas and 148 are benign moles.

The set of images is split in two groups: training and testing groups.

The training dataset consists of 70% (204) of the images (102 melanomas and 102 benign moles). The testing dataset consists of 87 images (41 melanomas and 46 benign moles). The training set is constructed by selecting those melanomas and benign moles which maximized the variation of samples for each group.

3.3.9.3 Feature selection

The feature set consists of 187 features. It is recommended to reduce the feature set to reduce dependency, and to increase accuracy. Therefore, principal component analysis (PCA) is used to reduce the high dimensionality of the feature set. PCA transforms a set of correlated data into a new set of linearly uncorrelated data. PCA is performed by computing the eigenvectors W from the covariance matrix $= XX^T$, where X is the matrix of all the features for all the skin images. Then k eigenvectors which have the biggest eigenvalues associated are identified (Martínez & Kak, 2001). The number of principal components k that explains 98% of the variation of the 187 features are identified.

3.3.9.4 Parameter tuning for SVM

Two parameters are required to be configured to train and classify the skin images using SVM, C and γ. In order to find a good combination of values for the two parameters, a grid search is conducted. The range of possible values for the parameters to configure the classification algorithm is suggested by Hsu (Hsu et al., 2010):

$$C \in (2^{-5}, 2^{-3}, 2^{-1}, 2, 2^{3}, 2^{4}, 2^{5}, 2^{6}, 2^{7}, 2^{10}, 2^{13}, 2^{15})$$

$$\gamma \in (2^{-15}, 2^{-13}, 2^{-10}, 2^{-7}, 2^{-8}, 2^{-6}, 2^{-5}, 2^{-4}, 2^{-3}, 2^{-2}, 2^{-1}, 2, 2^{2}, 2^{3}, 2^{4})$$

Therefore, a grid search is performed with all the possible combinations between(C, γ).

The algorithm is as follows:

- Construct the PCA feature set as explained.
- Construct the vector of labels. A label indicates the group of each training image, 1 for melanoma and -1 for benign moles.
- Configure the SVM with the selected pair (C, γ).
- Start the training process with the training set
- Test the classification with the training set
- Test the model with the testing set.
- Store the obtained accuracy

3.3.10 Diagram of architecture

Figure 3.16 presents the architecture of the program developed for objective 3.

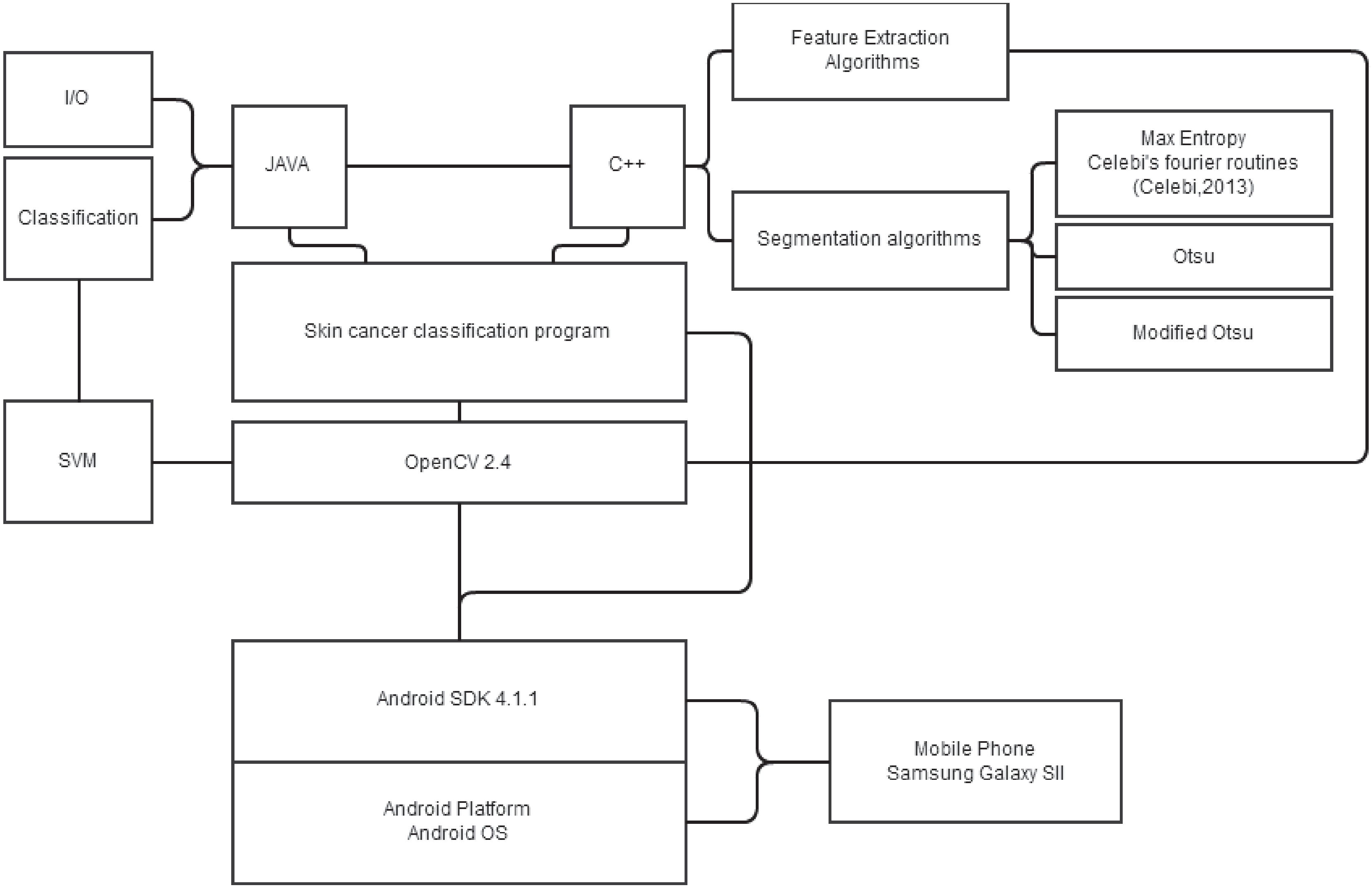

Figure 3.16: *Diagram of architecture for the skin cancer classification program*

CHAPTER 4. RESULTS AND DISCUSSIONS

This chapter presents the results and discussions of the research. First, the results of the data compiled for the four popular cellphones are discussed. Second, the methodology to acquire quality medical images with a cellphone is described. Finally, the results of the smartphone application to diagnose skin cancer are presented.

4.1 Objective 1

In the world, there are currently 6 billion cellphone subscriptions (International Telecommunication Union, 2012), with a distribution of 5 billion subscription in developing countries and 1 billion in developed countries. Therefore, this data demonstrates how important is to analyze the feasibility of cellphones for telemedicine purposes, as the majority of people in the world are still owners of cellphones.

Nokia is a well-known company for production of cellphones. It was the global leader of this market until 2012 when Samsung became the new leader of cellphones (Goasduff & Pettey, 2012). Nokia competes in the mobile phone market by cost. Its biggest market in the world is the developing countries. Therefore, the standard cellphone chosen for the evaluation is selected to be a Nokia, as they are still the most popular cellphones. It is difficult to determine a very popular cellphone, because there are currently in the market hundreds of different models. Thus, the cellphone chosen meets some criteria but it is not the most popular one. Nokia 2720 is inexpensive, around $50, and it is relatively new as it came to market in September, 2009. It was quite popular at the beginning. The life of a cellphones is very short, so Nokia 2720 does not have an important market share.

Figure 4.1: *Nokia 2720.*

Nokia 2720 is a cellphone thought to be very competitive in cost. The main screen is a 120 x 160 Thin-film transistor (TFT) with 16 bit color screen, so it can represent up to 65536 colors. It includes one front screen of very low resolution. The phone camera has low resolution, 1.6 Megapixels (MP) compared to 5 MP found in currently available cameras. Nokia 2720´s camera does not have flash, and a variable focus. It has a digital zoom of 4x. It stores images using JPEG, but it is possible to work with BMP, PNG or GIF. The camera has built-in functionalities such as white balance, auto exposure, and scene modes. The cellphone uses a Li-Ion battery of 860 mAh with duration of 400 hours in stand-by and up to 4 hours of talk time. The cellphone does not have external storage like flash card, with only 9 MB of internal storage. The connectivity of Nokia 2720 is very limited, having only the possibility to connect through internet via General Packet Radio Service (GPRS) or Bluetooth. It does not have USB port, so in the case of sending medical images, this limitation creates an important barrier for telemedicine purposes, because not all the cellphone subscriptions have internet connectivity. The phone runs a property OS and a custom Java version, so theoretically it is not possible to include a telemedicine application on the phone to diagnose cancer, because there is no a source development kit for third parties. However, it would be possible to obtain medical pictures and send them through internet for further analysis. The dimensions of the phone is 93 x 46 x 17.9 mm and has a weight of 90.3g. The phone is really inexpensive. The price could vary from operator to operator and country to country, but usually it is around $20-$70. It is undoubtedly a really good inexpensive phone for customers with a low income but wanting to have capabilities of modern cellphones.

RIM is a Canadian telecommunications company known for its BlackBerry smartphone. Blackberry is characterized for having a physical keyboard instead of using a touch screen. This keyboard became the identity´s signature of RIM´s BlackBerry. RIM enjoyed several years of success, increasing its net profits every year. But by the end of 2010, new and better smartphones became widely available. BlackBerry started selling less and less. Customers preferred to acquire a touch smartphone, more useful for navigation purposes (Chitika, 2012). The main market for RIM was the business environment because RIM offered a highly secure network for instant messaging, including different useful tools for managers. The physical keyboard helped to improve the efficiency of businessmen. However, Apple is currently gaining more percentage of this market, while RIM is plummeting. Nevertheless, BlackBerry is still a smartphone with an important market share; it was included in this study. In Table 2.1 the market Share of the principal smartphone vendors in the USA, is shown.

Figure 4.2: *BlackBerry Curve 9320*

The BlackBerry chosen for the research is the BlackBerry Curve 9320. It was released on 2010. It has a 320 x 240 TFT color screen of 16-bit. The inbuilt camera has 2 MP. The phone camera has the common functionalities like white balance or video recording. It does not have flash. It has a fixed focus with digital zoom. The storage capacity of the smartphone is high, allowing using microSD up to 32 GB and it has 256MB of internal memory. BlackBerry is considered a smartphone because of its connectivity. BlackBerry Curve 9300 has full connectivity with Wi-Fi b/g/n support, and Bluetooth. The smartphone works with the 2G and 3G and HSDPA cellphone networks, meaning that it can be connected to internet to speeds up to 7.2MB/s. Moreover, it has a USB port, that can connect the phone to external USB modems, or external memory, or even the computer. RIM is the only company, together with Apple, who builds its own hardware and OS for its smartphones. Therefore all BlackBerrys run BlackBerry OS, but in this case it runs also a Java virtual machine. Therefore it is possible, theoretically, to develop hardware independent telemedicine applications to diagnose cancer. BlackBerry Curve 9300 has dimensions of 109 x 60 x 13.9 mm and has a weight of 104 g. The price is more expensive than a cellphone. This model is not the newest one, so the price has been reduced, but it is still around $150.

Apple is a multinational company which develops hardware and software. It is a leader in the market of tablets and smartphones. It is almost standardizing the shape and functionalities of the current smartphones available in the market. Even though Apple did not invent the touch screen, it actually developed a smartphone which integrated very well the touch capabilities and a good OS. The first smartphone that Apple released was the iPhone. Currently, the iPhone 5 is available. However, this research reviews the iPhone 3GS, which is not different from the newest iPhone and it is more affordable than the iPhone 5 in second hand markets.

Figure 4.3: *iPhone 3GS*

iPhone 3GS was released in 2009 worldwide. It has a 320 x 480 multi touch capacitive TFT screen with 16 million colors. The main difference between iPhone 3GS and the newer versions is the camera resolution. While 3GS phone has a 3.15MP camera, the cameras in newer versions have resolution up to 8 MP. 3.15MP camera is sufficient to acquire high quality images. The inbuilt functionalities of the camera include auto focus, touch focus, white balance, and auto macro, (up to 10 cm). With auto macro it is possible to acquire focused images having the camera very close to the subject. IPhone does have external memory; hence flash memory card cannot be added to increase the storage capacity of the phone. However, iPhone was released with large storage capacity, 8, 16 or 32 GB. iPhone 3GS has 256 MB of RAM. It has all the connectivity features expected from a smartphone: Wi-Fi b/g, Bluetooth, USB. iPhone also works with 2G and 3G phone networks, achieving speeds up to 7.2 when there is HSDPA signal. Apple also builds its own hardware and software, hence iPhone runs with its own OS called iPhone OS. Regardless, it does not have a Java machine running on the phone, Apple has created a set of tools to facilitate software developers to design and built applications for the phone. Therefore, Apple has created a myriad of mobile applications exclusive for iPhone. The organization has the leadership in the market of smartphones. The dimensions of the phone are 115.5 x 62.1 x 12.3 mm and weights 135g. iPhone is actually the most expensive smartphone currently in the market. The Apple smartphone considered in this research is quite old, and actually, it is only possible to find it in the second hand market. The price in this market goes from $70 to $150 depending on the quality of the phone. Usually when a new iPhone is released in the market, the price is between $500 and $700.

Samsung is an electronic multinational company with headquarters in Seoul, Korea. It is well-known for its TV, Tablet and smartphone products. Whereas in the smartphone market, Apple and RIM built their own software and hardware, Samsung only produces the hardware. For the software, Samsung uses the open platform from Google called Android. Android is an open source hardware independent operating system for tablets and smartphones. Samsung released its first smartphone with android in 2009 called Samsung Galaxy. The smartphone used in this research is the evolution of the first Samsung with Android O/S called Samsung Galaxy SII.

Figure 4.4: *Samsung Galaxy SII*

Samsung Galaxy SII is a smartphone released in 2011. It uses a 480 x 800 super AMOLED multitouch capacitive screen with 16 million colors. It has a high resolution camera with 8 MP and it includes a second camera (2 MP resolution) for video conferencing purposes. It is the only phone in this study that includes a camera with flash. Moreover, the camera has a fixed focal length with digital zoom. Samsung Galaxy SII allows using microSD up to 32 GB, and also it has 16 or 32 GB of internal storage. It has 1 GB of RAM. This smartphone uses Android OS so it is possible to develop user applications using the Android tools provided by Google. To run the applications, it uses a Java virtual machine. Theoretically, the application is hardware independent. Actually, Android smartphones suffer from fragmentation, meaning that there are dozens of different phones with Android with different capabilities, so this ends up having applications which do not work in all the Android versions. The smartphone has Wi-Fi connectivity and Bluetooth. Also, it adds a USB port. Samsung Galaxy SII connects to 2G, 3G and HDPSA+ phone networks, so it can reach speeds up to 12MB/s. Newer versions of this phone can connect to the LTE or 4G networks. The dimensions of the phone are 125.3 x 66.1 x 8.5 mm and weights 116 g. The price of Samsung Galaxy SII varies from \$300 to \$500.

In Table 4.1 the compilation of the technical features for each mobile phone is presented.

4.1.1 Camera test

Figure 4.5, Figure 4.6, Figure 4.7, and Figure 4.8 show the ColorChecker images obtained using the four cellphones.

Table 4.1: Cellhpone and smartphones technical comparison

	Screen	**Camera**	**Battery**	**Storage**	**Connectivity**	**Dimensions**	**Price**
Nokia 2720	• TFT • 120 x 160 • 16 bits	• 1.3 MP • 1280 x 1024 • No flash • White balance • Fixed Focus	• Li-Ion 860 mAh • Standby: 400h • Talk : 5h	• No external storage • 9MB Internal storage	• Bluetooth • 2G	• 93 x 46 x 17.9 • 90.3 g	$20-$70
BlackBerry Curve 9300	• TFT • 320 x 240 • 16 bit	• 2 MP • 1600 x 1200 • No flash • ISO	• Li-Ion 1150 mAh • Standby: 456 • Talk: 4h30’	• MicroSD 32GB • 256 MB internal memory	• Wi-Fi • Bluetooth • 2G / 3G / HSDPA	• 109 x 60 x 13.9 • 104 g	$90-$150
iPhone 3GS	• TFT • 320 x 480 • 24 bits • Multitouch	• 3.15 MP • 2048 x 1536 • No flash • ISO	• Li-Ion • Standby: 300h • Talk: 12 h	• No external storage • 8 / 16 / 32 GB internal	• Wi-Fi • Bluetooth • 2G / 3G / HSDPA	• 115.5 x 62.1 x 12.3 • 135 g	$70 - $150
Samsung Galaxy SII	• SUPER AMOLED • 24 bits • Multitouch	• 8 MP front • 3264 x 2448 • LED Flash • ISO • Secondary camera 2 MP	• Li-Ion 1650 mAh • Standby: 710 h • Talk: 18h	• MicroSD 32 GB • 16 / 32 GB internal storage	• Wi-Fi • Bluetooth • 2G / 3G / HSDPA+ / LTE	• 125.3 x 66.1 x 8.5 • 116 g	$200-$400

Figure 4.5: *Nokia´s image of the ColorChecker*

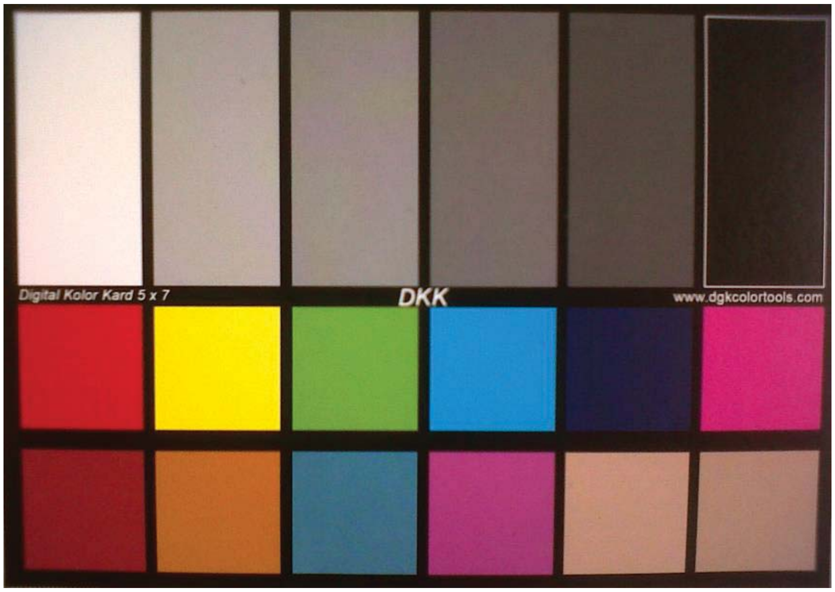

Figure 4.6: *BlackBerry´s image of the ColorChecker*

Figure 4.7: *iPhone´s image of the ColorChecker*

Figure 4.8: *Galaxy´s image of the ColorChecker*

The four images were obtained with the same light conditions as described in section 3. With visual inspection, it is easy to detect the differences in quality of the four cameras.

The real color of each square is indicated in the backside of the Color Checker chart.

Table 4.2: (a) Euclidean distance to the real red color (255,0,0), and (b) Values of the red square for the four phones

(a)

Phone	Distance
Nokia	99.3077
BlackBerry (BB)	85.2239
iPhone	54.7961
Galaxy	66.1143

(b)

	Red coordinate			**Green coordinate**			**Blue coordinate**		
Phone	μ mean	σ std dev.	$\frac{\sigma}{\mu}$ variability	μ mean	σ std dev.	$\frac{\sigma}{\mu}$ variability	μ mean	σ std dev.	$\frac{\sigma}{\mu}$ variability
Nokia	182.615	3.402	0.018	51.763	3.957	0.076	44.097	5.309	0.120
BB	190.463	5.187	0.027	33.963	3.915	0.115	28.978	4.002	0.138
iPhone	212.840	3.670	0.017	19.631	3.602	0.183	14.739	3.690	0.250
Galaxy	209.671	3.106	0.014	45.816	2.994	0.065	44.079	3.019	0.068

Table 4.3 illustrates the results obtained with the four phones. iPhone is the phone which obtains the closest representation of the red square. However, the spread of the distribution is bigger for the other phones than for the Galaxy SII.

Table 4.3: (a) Euclidean distance to the real green color (94,255,0), and (b) Values of the green square for the four phones

(a)

Phone	Distance
Nokia	117.4996
BlackBerry (BB)	90.0019
iPhone	101.7802
Galaxy	82.6449

(b)

	Red coordinate			Green coordinate			Blue coordinate		
Phone	μ mean	σ std dev.	$\frac{\sigma}{\mu}$ variability	μ mean	σ std dev.	$\frac{\sigma}{\mu}$ variability	μ mean	σ std dev.	$\frac{\sigma}{\mu}$ variability
Nokia	101.769	3.602	0.035	148.434	1.595	0.010	48.883	5.053	0.103
BB	101.484	4.246	0.041	177.409	3.448	0.019	44.989	5.000	0.111
iPhone	98.048	4.085	0.041	157.157	3.441	0.021	27.742	3.704	0.133
Galaxy	109.908	9.173	0.083	178.980	8.479	0.047	28.250	8.924	0.315

Samsung Galaxy SII represents with the highest quality the green square. However, in general the results representing this green color are less accurate than the results of representing the red square. The coefficients of variation are very similar amongst Nokia, BlackBerry and iPhone. However, Galaxy phone presents bigger variability than the rest. The spread of its distribution is bigger.

Table 4.4 presents the results obtained with the four cellphones using the blue square (RGB values (0,20,102), square number five in the ColorChecker chart). The best representation of the blue square is obtained using BlackBerry and iPhone. Samsung Galaxy's image is brighter than the other images. Therefore, the representation of the blue square is less accurate. Besides, Samsung Galaxy and iPhone have the highest coefficient of variation.

Table 4.5 presents the results obtained with the four phones from the white square (RGB value (255,255,255)). iPhone yields the best accuracy of representing a true white. In general the results are better than for green and blue squares. The coefficient of variability for Samsung Galaxy and iPhone is very low. On the other hand, Nokia and Blackberry have bigger variability; therefore the values are more spread.

Table 4.4: (a) Euclidean distance to the real blue color (0,20,102), and (b) Values of the blue square for the four phones

(a)

Phone	**Distance**
Nokia	59.4871
BlackBerry (BB)	50.9145
iPhone	57.9156
Galaxy	64.7060

(b)

	Red coordinate			**Green coordinate**			**Blue coordinate**		
Phone	μ mean	σ std dev.	$\frac{\sigma}{\mu}$ variability	μ mean	σ std dev.	$\frac{\sigma}{\mu}$ variability	μ mean	σ std dev.	$\frac{\sigma}{\mu}$ variability
Nokia	42.990	4.680	0.108	48.327	1.419	0.029	72.199	2.527	0.035
BB	35.647	4.851	0.136	41.385	2.469	0.059	72.603	2.810	0.038
iPhone	14.303	3.556	0.248	27.071	3.071	0.113	46.325	3.278	0.070
Galaxy	51.079	7.442	0.145	59.681	7.117	0.119	100.208	6.947	0.069

Table 4.5: (a) Euclidean distance to the real white color (255,255,255), and (b) Values of the white square for the four phones

(a)

Phone	**Distance**
Nokia	57.4489
BlackBerry (BB)	45.9349
iPhone	34.0635
Galaxy	62.4314

(b)

	Red coordinate			**Green coordinate**			**Blue coordinate**		
Phone	μ mean	σ std dev.	$\frac{\sigma}{\mu}$ variability	μ mean	σ std dev.	$\frac{\sigma}{\mu}$ variability	μ mean	σ std dev.	$\frac{\sigma}{\mu}$ variability
Nokia	217.145	3.004	0.013	218.638	2.349	0.010	231.648	3.162	0.013
BB	220.067	6.156	0.028	234.478	5.349	0.022	233.351	5.332	0.022
iPhone	233.587	1.789	0.007	235.660	1.667	0.007	236.894	1.730	0.007
Galaxy	214.136	1.301	0.006	218.657	1.435	0.006	224.882	1.312	0.005

Table 4.6 presents the results obtained with the four phones from the black square (RGB value (0,0,0)). iPhone has the smallest distance to the real black. The results obtained by Galaxy are in consonance with the previous results. It obtains the brightest images. iPhone obtains the biggest coefficient of variability because its mean values are closer to 0. However, it has the smaller standard deviations. Therefore in conclusion, iPhone has the camera which better represents blacks.

The conclusion of this test is that iPhone obtains the best results relatively. It obtains the best accuracy in 3 out of 5 tests (red, white and black), whereas BlackBerry obtains the best accuracy representing the blue square and Samsung Galaxy yields the best result on the representation of the green square.

4.1.1.1 Resolution test

The second test analyzes the resolution performance for each cellphone. Figure 4.9, Figure 4.10, Figure 4.11 and Figure 4.12 show the image acquired of the ISO 12233 chart.

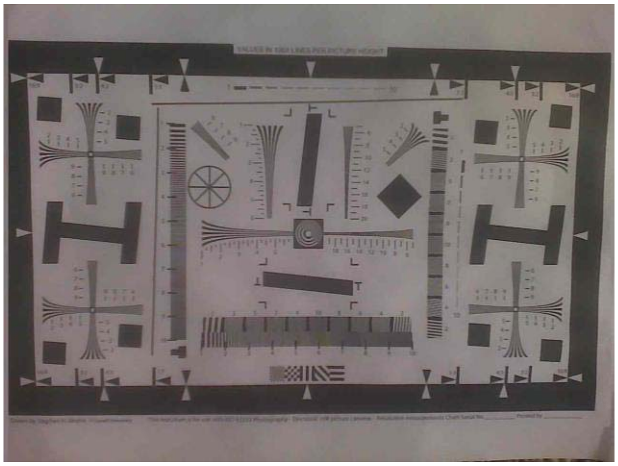

Figure 4.9: *ISO 12233 chart of Nokia 2720*

Table 4.6: (a) Euclidean distance to the real black color (0,0,0), and (b) Values of the black square for the four phones

(a)

Phone	**Distance**
Nokia	97.7291
BlackBerry (BB)	60.3609
iPhone	35.3981
Galaxy	104.4833

(b)

	Red coordinate			**Green coordinate**			**Blue coordinate**		
Phone	μ mean	σ std dev.	$\frac{\sigma}{\mu}$ variability	μ mean	σ std dev.	$\frac{\sigma}{\mu}$ variability	μ mean	σ std dev.	$\frac{\sigma}{\mu}$ variability
Nokia	57.354	5.455	0.095	59.321	5.865	0.098	52.367	6.261	0.119
BB	34.412	4.957	0.144	36.219	3.887	0.107	33.872	5.065	0.149
iPhone	18.866	3.473	0.184	24.179	3.434	0.1420	17.675	3.408	0.192
Galaxy	62.403	5.137	0.082	60.935	5.171	0.084	57.527	5.330	0.092

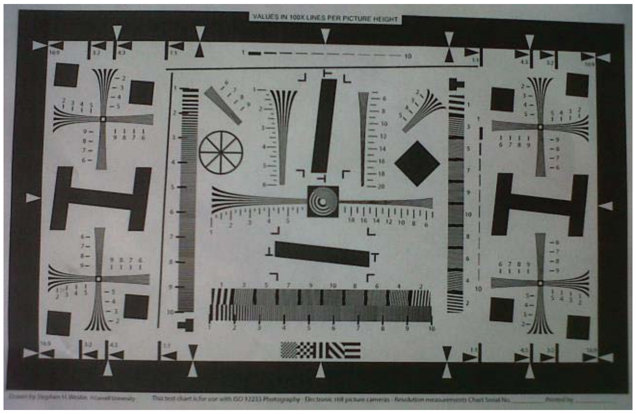

Figure 4.10: *ISO 12233 chart of BlackBerry*

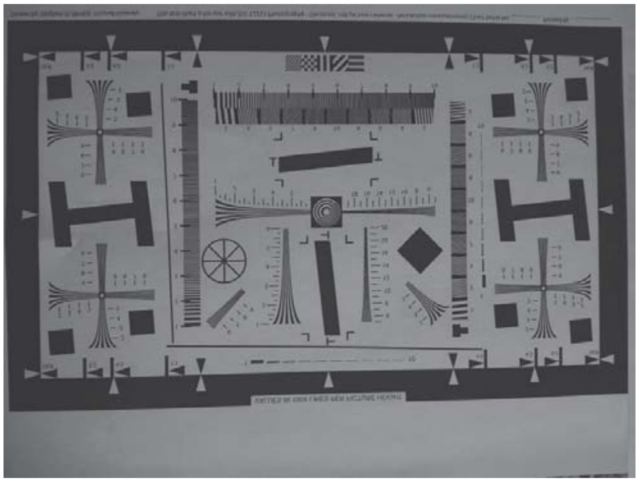

Figure 4.11: *ISO 12233 chart of iPhone*

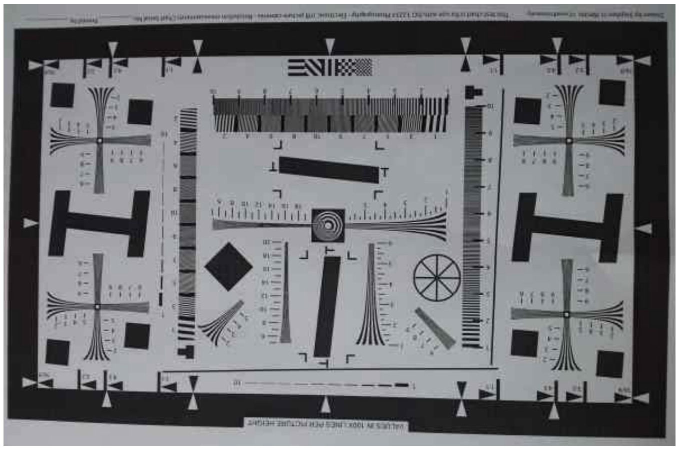

Figure 4.12: *ISO 12233 chart of Samsung Galaxy*

Figure 4.13 and Figure 4.14 show the central circle from ISO 12233 chart augmented. The level of blurriness of the lines indicates the resolution performance of each cellphone camera.

(a) (b)

Figure 4.13: *Sample image using (a) Nokia and (b) BlackBerry*

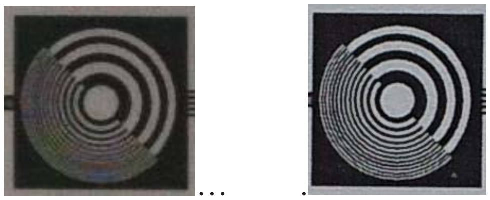

… .

(a) (b)

Figure 4.14: *Sample image using (a) iPhone and (b) Samsung Galaxy*

Nokia and Blackberry images do not differentiate any line from the bottom part of the circle. On the other hand, the iPhone 3GS results are much better. Almost all the circles are visible. Finally, Samsung Galaxy SII has the highest resolution. All the circle lines are clearly visible.

The next figures show another portion of the chart ISO 12233. These samples consist of the rule located at the top part of the chart. It consists of separated lines. Every level of separation is indicated as a number at the top or bottom part of the rule. Therefore, the higher the resolution of the camera, the more lines are possible to differentiate from the ruler.

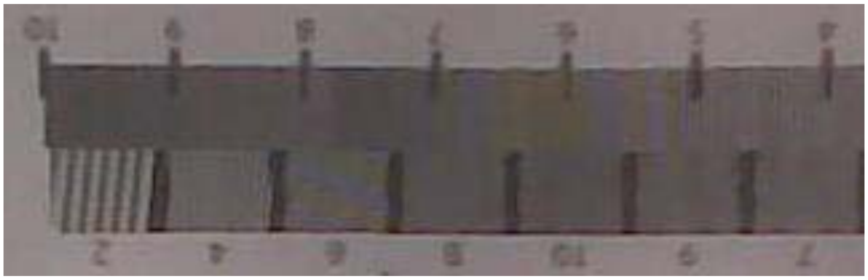

Figure 4.15: *Sample image using Nokia*

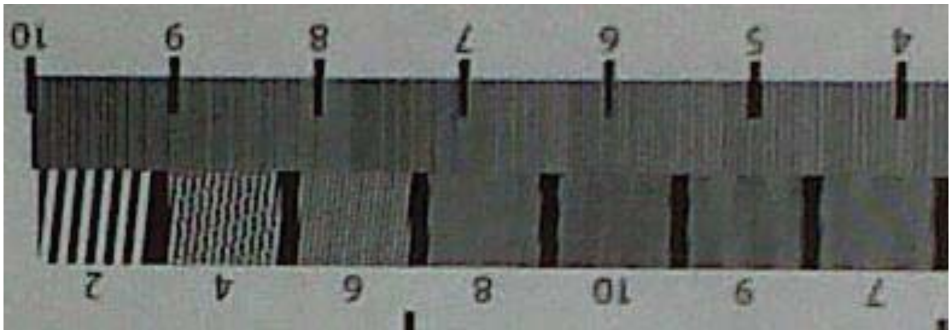

Figure 4.16: S*ample image using BlackBerry*

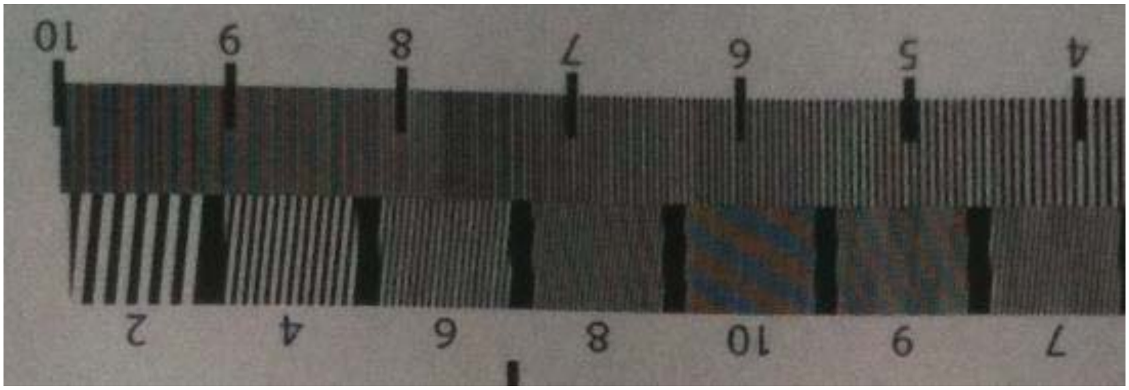

Figure 4.17: *Sample image using iPhone*

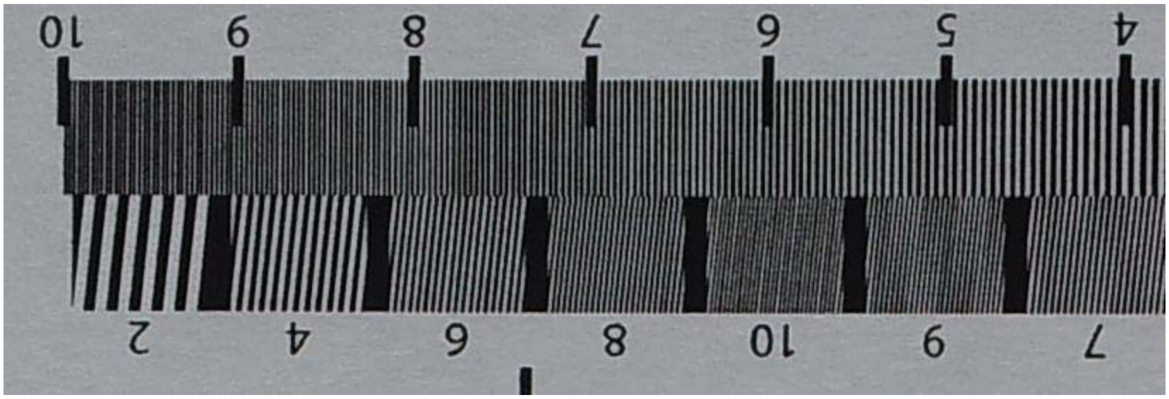

Figure 4.18: S*ample image using Galaxy*

The results obtained are similar to the circle´s results. In Nokia’s acquired image, (Figure 4.15), it is only possible to see the separation between lines in the levels two and three from the bottom part of the ruler. BlackBerry’ acquired image (Figure 4.16) illustrates that the phone camera is able to differentiate only lines in the levels two, four and six from the bottom part, and in level four from the top part of the rule. On the other hand, iPhone gets a very high quality in resolution. In Figure 4.17, it is possible to differentiate all the lines at the top of the ruler, and until level eight in the bottom ruler.

Finally, Samsung Galaxy obtains the highest resolution quality. Figure 4.18 illustrates that Samsung Galaxy is able to capture all the lines from the ruler. Therefore, iPhone and Samsung Galaxy are yielding the best results in this test. Notice that the iPhone is capable to capture almost all the separation lines, whereas a similar resolution camera such as Blackberry's camera, can hardly differentiate the lines in four levels.

4.2 Objective 2

Three configurations have been developed to test the efficacy to acquire quality color images of a skin cancer mole of three different cellphones cameras. In each image a ruler is also incorporated to indicate the size of the melanoma. The camera's configuration for each cellphone is illustrated in *Table 4.7*. ISO system is the measure of camera light sensitivity. The larger the ISO value the more sensitive will be the camera to the light. However, the image will present more noise. Therefore, to obtain the highest quality image possible, the lowest possible ISO value is required. On the other hand, White-Balance (WB) is the process to remove unrealistic colors on the image. The cameras usually have White-Balance systems to represent the white color as white regardless the color temperature of the light.

Table 4.7: Cellphones camera configuration

Phone	Focus	ISO	WB	Picture Quality	Exposure	Flash
Samsung	Macro	50	Daylight	Very High	0	OFF
BlackBerry	Infinity	100	Daylight	Very High	0	OFF
Nokia	Infinity	N/A	N/A	N/A	N/A	OFF

The first configuration corresponds to side lighting with room light. The results are presented in Figure 4.19.

Samsung Galaxy is able to capture a focused image, despite the fact that the object is very close to the lens. On the other hand, BlackBerry and Nokia's images are blurred because of the short distance between camera and object (because of the lack of macro focus setting). Galaxy's image is brighter, and the characteristics of the mole are better differentiated than those acquired by other phones.

The second lighting configuration uses only the table light in one side. Figure 4.20 presents the results. The blurriness effects, in BlackBerry and Nokia, are still present in this configuration. Besides, the images are darker than those in the previous configurations.

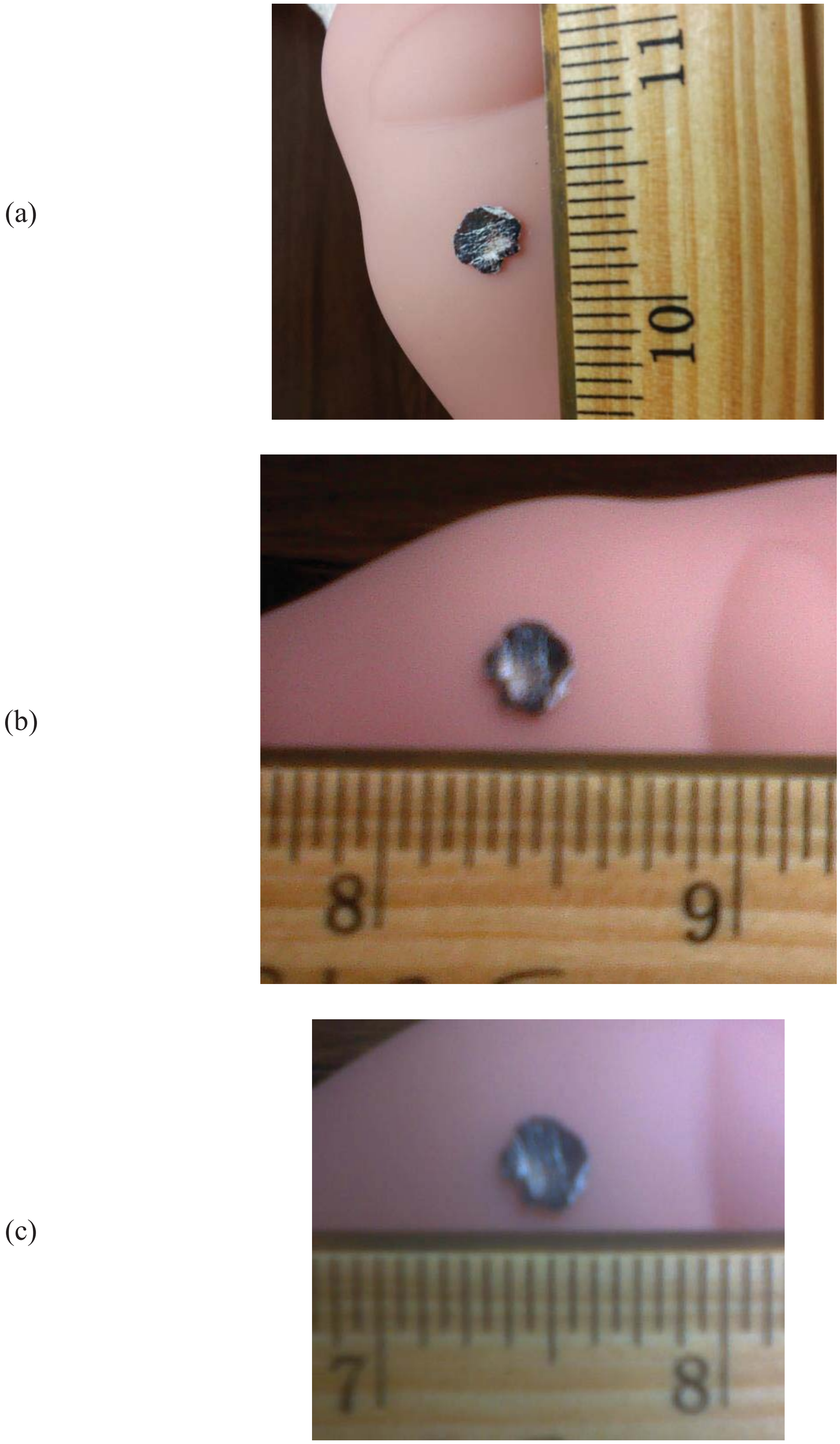

Figure 4.19: *Image acquired using (a) Samsung Galaxy SII, (b) BlackBerry Curve 9300 and (c) Nokia 2720. Configuration one*

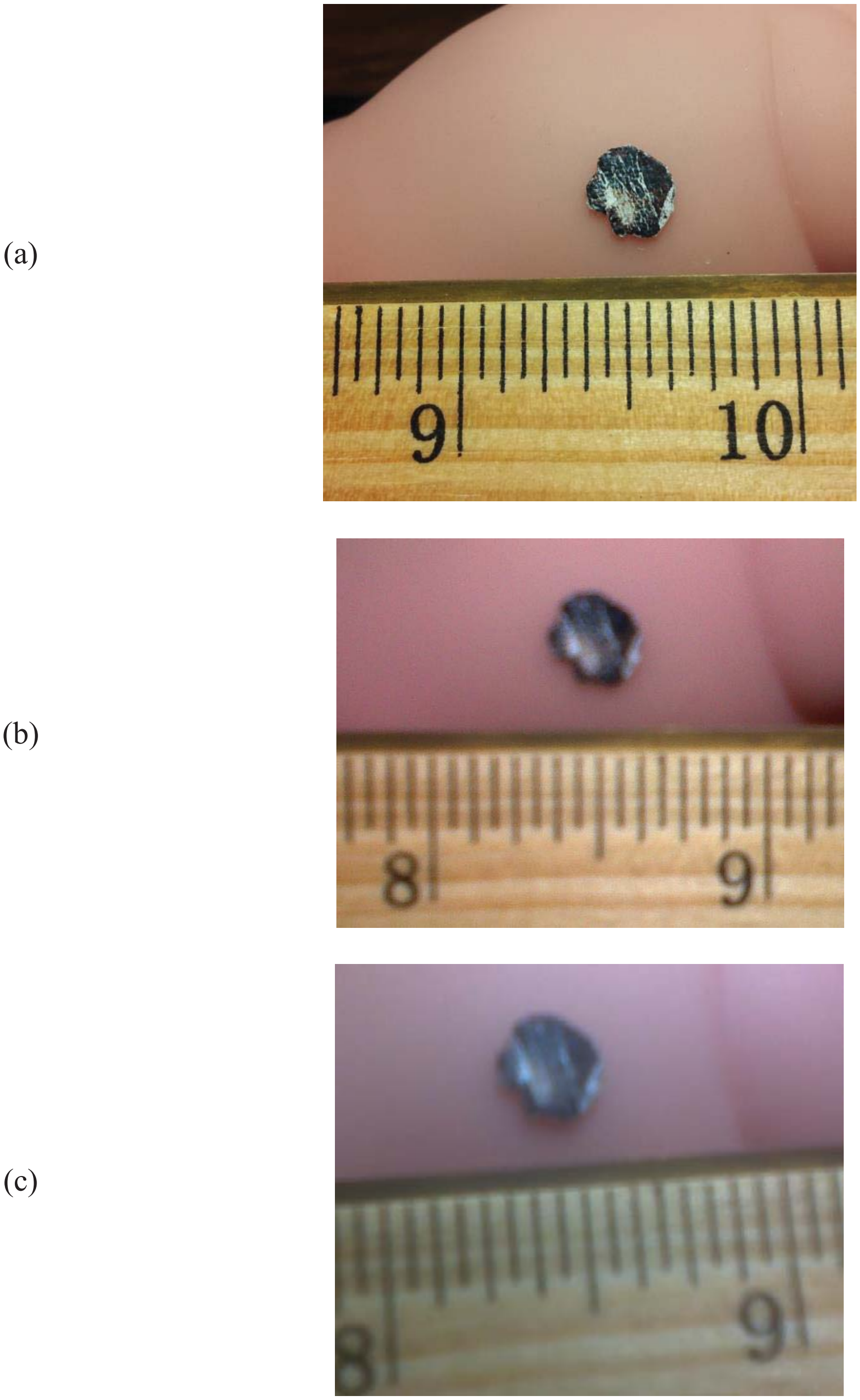

Figure 4.20: *Images acquired using (a) Samsung Galaxy SII, (b) BlackBerry Curve 9300 and (c) Nokia 2720. 2^{nd} lighting configuration*

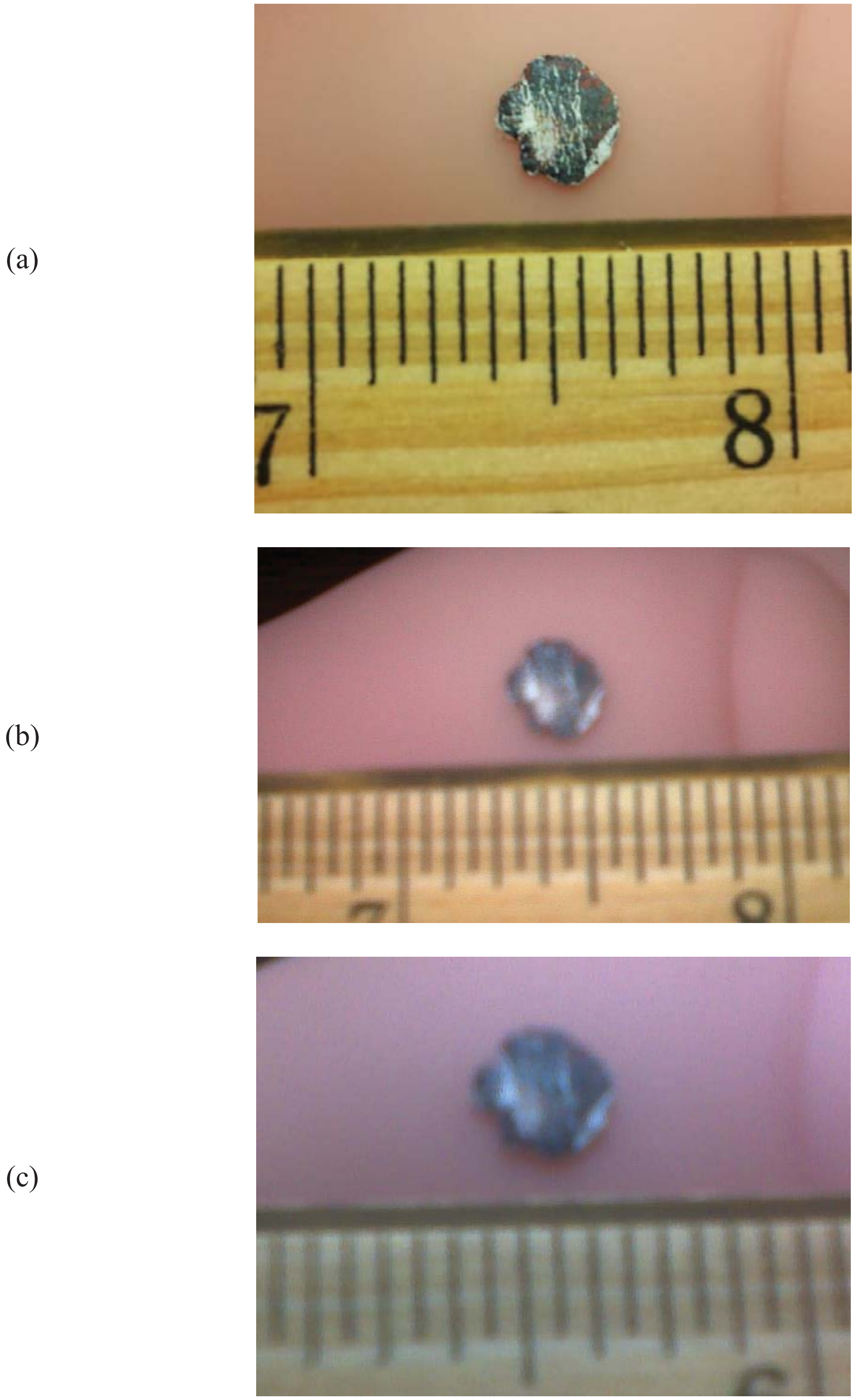

Figure 4.21: *Images acquired using (a) Samsung Galaxy SII, (b) BlackBerry Curve 9300 and (c) Nokia 2720. 3rd lighting configuration*

The last lighting configuration used front lighting. Figure 4.21 presents the results.

The blurriness of the images obtained with Nokia and BlackBerry phones are still present. The images are little bit brighter, and therefore it is easier to see the mole characteristics.

In general, Samsung Galaxy SII performs very well in the three configurations. It obtains the highest quality image using the configuration three with frontal lighting, even though the differences are minimal. On the other hand, BlackBerry and Nokia struggle to obtain quality images without the possibility to obtain images using macro focus. Therefore, although select light sources are used, the quality of the images is heavily impacted with the blurriness.

4.3 Objective 3

4.3.1 Image processing

Figure 4.22 shows a typical result of applying the Gaussian filter with $\sigma = 2$ to a mole image. Notice that the histograms in Figure 4.23 are also smoothed. The blurriness present on the right image of Figure 4.23 is due to averaging the pixels with their neighbors. The noise is reduced, and thus the next operations applied to the blurred image will obtain better results.

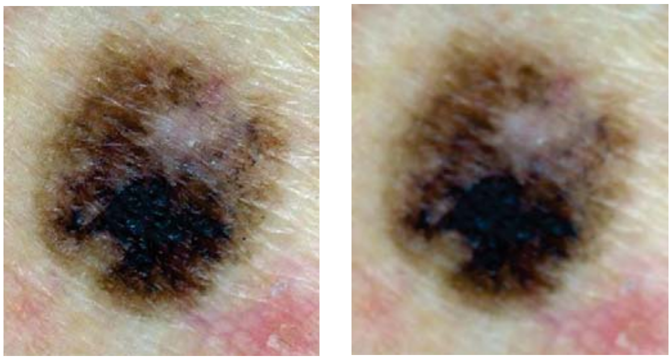
(a) (b)

Figure 4.22: *(a) Skin mole image and (b) Skin mole image after applying Gaussian filter source of image (Diepgen & Yihune, 2013, with permission)*

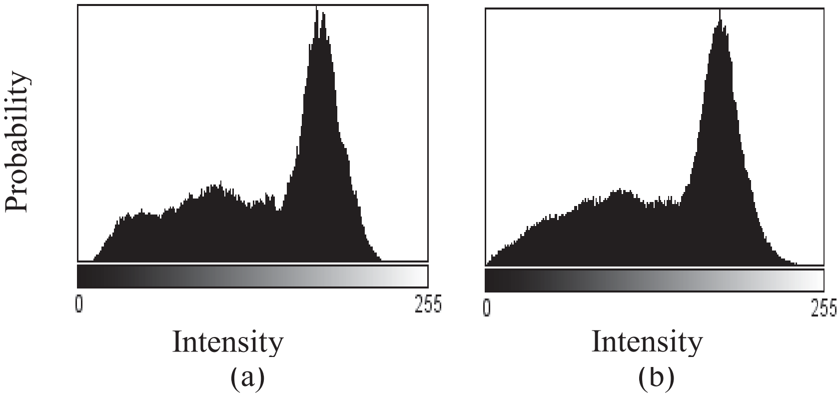

Figure 4.23: *(a) Histogram of the skin mole image without smoothing and (b) Histogram of the skin mole image with smoothing in grey scale*

4.3.2 Histogram based thresholding

The results of segmenting the images using Otsu´s, Modified Otsu´s and Max Entropy are presented. The segmentation process is performed in the RGB color space.

4.3.2.1 Histogram thresholding

Figure 4.25 shows the histogram for the three colors coordinates of Figure 4.24.

Result for segmentation of each color coordinate is presented below. A simple inspection of the histograms indicates that a better segmentation could result in the green coordinate, because of relatively better separation of peaks with a valley. On the other hand, histograms in red and blue coordinates do not show a clear valley.

Figure 4.27 shows the histograms of a typical mole image where segmentation could be challenging because of non-distinct valleys between peaks in the histograms. It demonstrates how neither red nor green coordinate has the required contrast to find a good threshold. The blue coordinate has two peaks and a valley, however, the separation is quite small. In conclusion, the segmentation process for the image shown in Figure 4.26 will not work.

Figure 4.24: A typical image of a *mole (Diepgen & Yihune, 2013, with permission)*

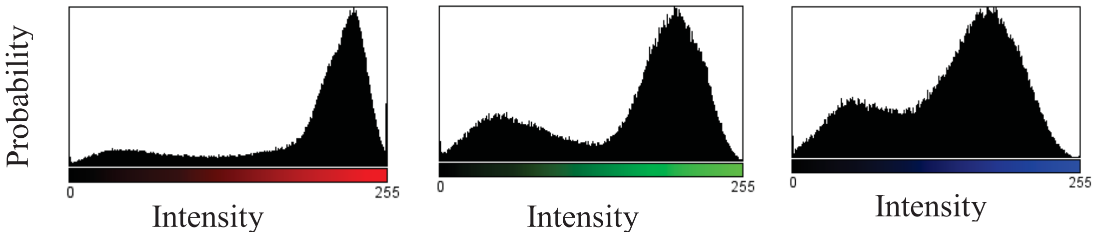

(a) (b) (c)

Figure 4.25: *Histograms of a typical mole of the (a) red, (b) green and (c) blue coordinates.*

Figure 4.26: *A typical mole image where the histogram segmentation process would not work effectively (Diepgen & Yihune, 2013, with permission)*

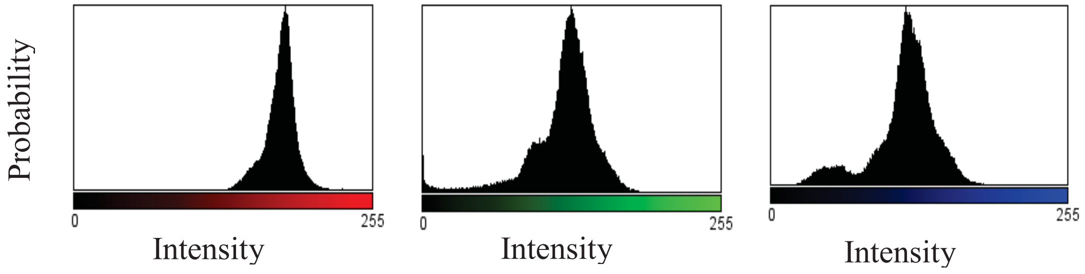

(a) (b) (c)

Figure 4.27: *Histograms of a segmented mole of the (a) red, (b) green and (c) blue coordinates*

4.3.2.1.1 Otsu’s Thresholding

Table 4.8 shows the threshold levels determined by Otsu´s algorithm on Figure 4.24. Figure 4.28 shows the result of the segmentation operation.

Table 4.8: Thresholding values determined by Otsu´s algorithm

	Red	**Green**	**Blue**
Otsu	146	132	123

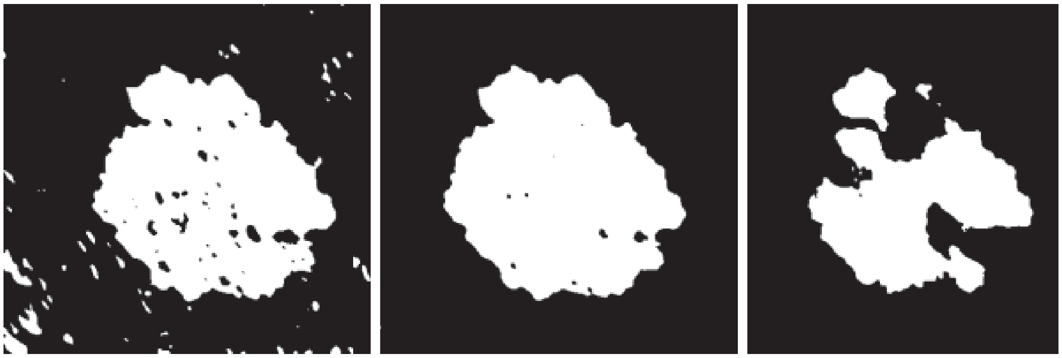

(a) (b) (c)

Figure 4.28: *Otsu´s Thresholding result for (a) red, (b) green and (c) blue coordinates*

It can be observed that red coordinate is little bit over segmented, and the blue coordinate is under segmented. In this example, green coordinate segments the mole effectively.

For the image in Figure 4.26, Otsu´s algorithm is not able to segment the image correctly in two of the three color coordinates:

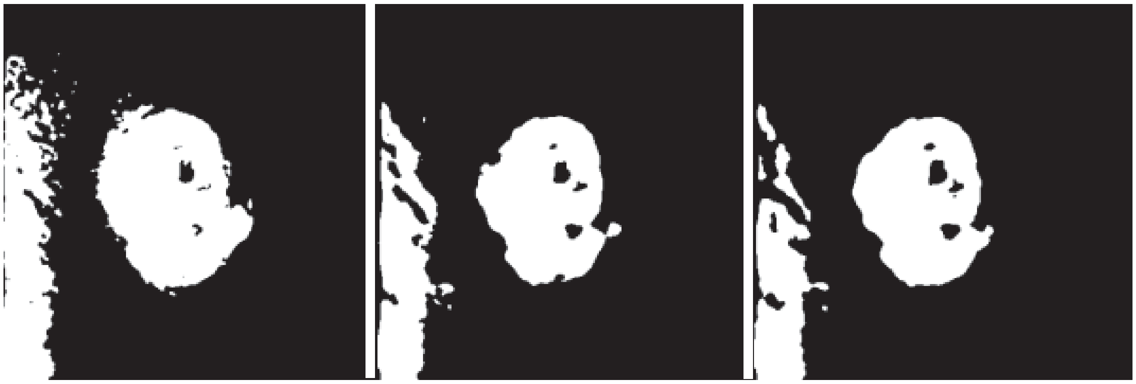

(a) (b) (c)

Figure 4.29: *A typical example of a undesirable segmentation of the Figure 4.26 for (a) red, (b) green and (c) blue coordinates*

4.3.2.1.2 Modified Otsu's

Table 4.9 shows the determined thresholds using Modified Otsu´s Thresholding for the image in Figure 4.24. Figure 4.30 shows the result of the segmented image. Notice the slight difference between Otsu´s Thresholding and Modified Otsu´s.

Table 4.9: Thresholding values determined by Otsu´s and Modified Otsu´s

	Red	**Green**	**Blue**
Otsu	146	132	123
Modified Otsu	147	134	123

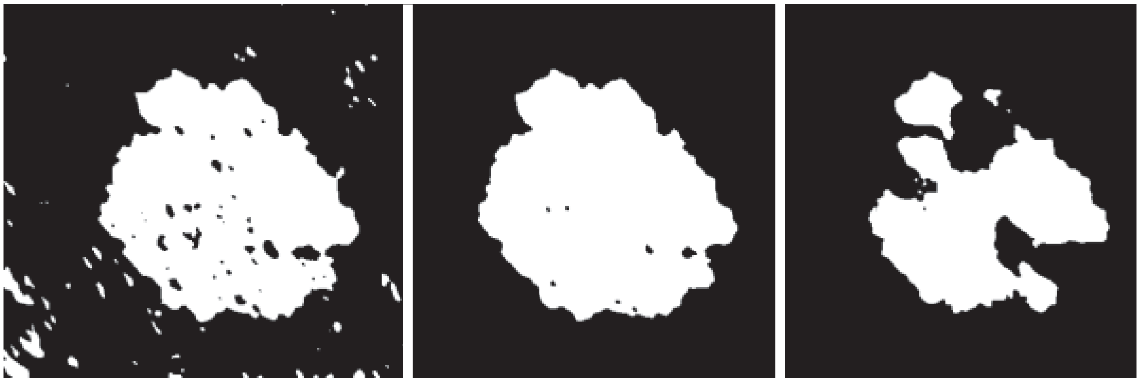

(a) (b) (c)

Figure 4.30: *Segmented images in (a) red, (b) green and (c) blue coordinates using Modified Otsu's algorithm*

While the histogram does not have a clear separation of background and object, Modified Otsu´s is also not capable to segment the image in all coordinates. Figure 4.31 shows the result of a segmentation using Modified´s Otsu, for a typical image with low contrast between object and background.

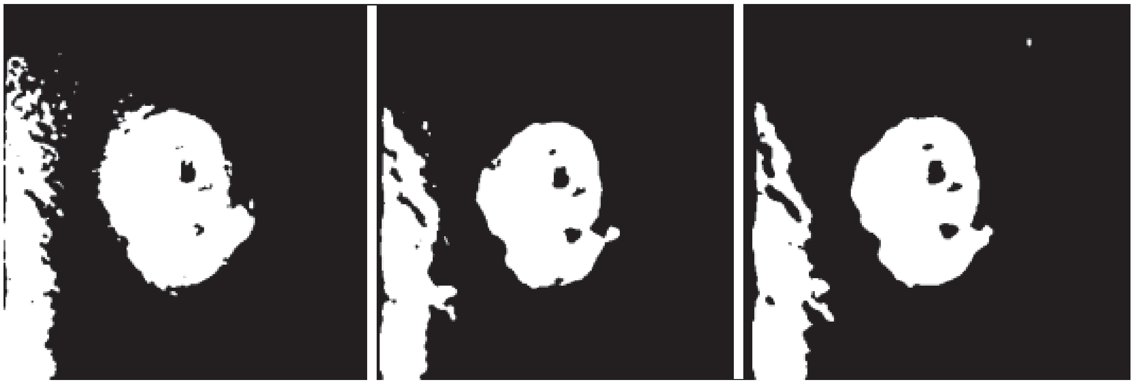

(a) (b) (c)

Figure 4.31: *A typical segmented images of image in Figure 4.26 in (a) red, (b) green and (c) blue coordinates using Modified Otsu's algorithm*

4.3.2.1.3 Max Entropy

Table 4.10 shows the thresholds determined by Max Entropy´s algorithm for the image in Figure 4.24. Figure 4.32 shows the result of the segmented image.

Table 4.10: Otsu´s, Modified Otsu´s and Max Entropy thresholds

	Red	**Green**	**Blue**
Otsu	146	132	123
Modified Otsu	147	134	123
Max entropy	163	156	129

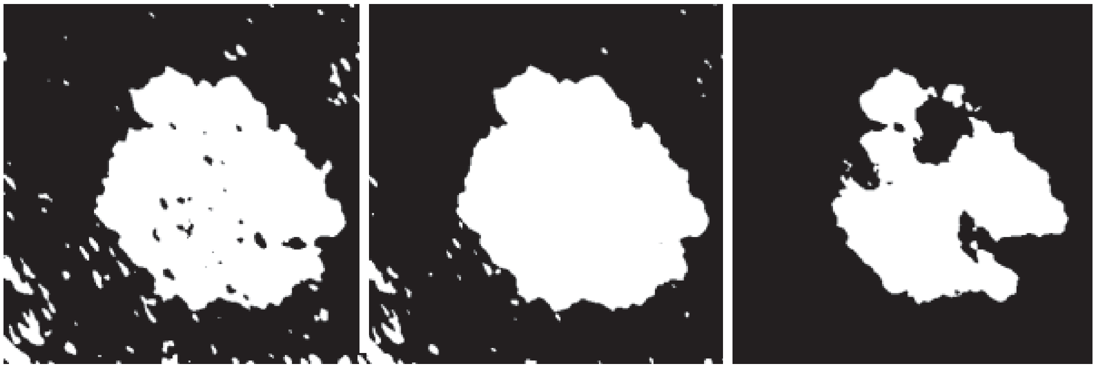

(a) (b) (c)

Figure 4.32: *Segmented image in (a) red, (b) green and (c) blue coordinates using using Max Entropy algorithm*

Max Entropy performs better than Otsu´s for the image in Figure 4.24. However, object and background are too similar; therefore neither Max Entropy is capable to accurately segment the image. The result is illustrated in Figure 4.33:

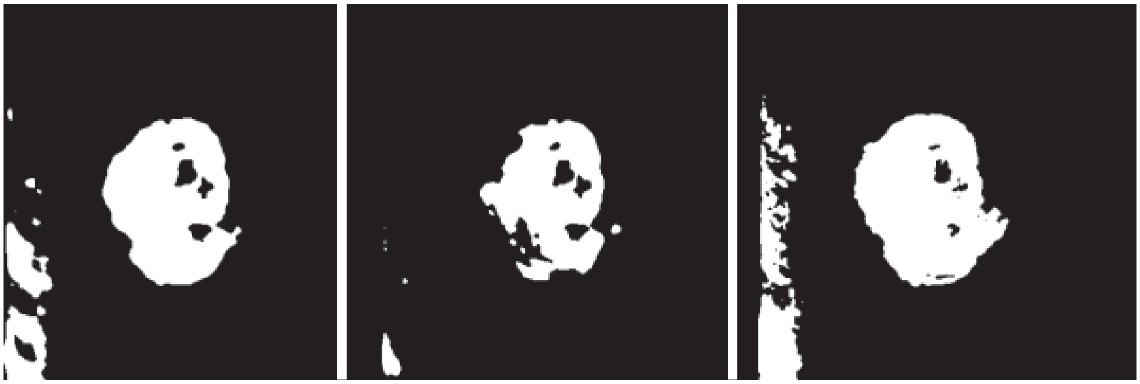

(a) (b) (c)

Figure 4.33: *Typical segmented images of the Figure 4.26 in (a) red, (b) green and (c) blue coordinates using Max Entropy algorithm*

4.3.2.2 Merging

For each algorithm (Modified Otsu´s and Max Entropy), three images were obtained. Figure 4.34 shows the result of merging the six images presented in Figure 4.24 and Figure 4.26.

Figure 4.34: *Intial merged image of the mole*

Once the initial merged image is obtained, it is necessary to find the contours for the objects present in the image in Figure 4.34. Figure 4.34 shows the shape of the mole surrounded with smaller artifacts. Therefore the operation to find all the contours produces an array whose size is the number of shapes and holes present in the image. Figure 4.35 shows the result of finding all the contours (contours and holes) within the image.

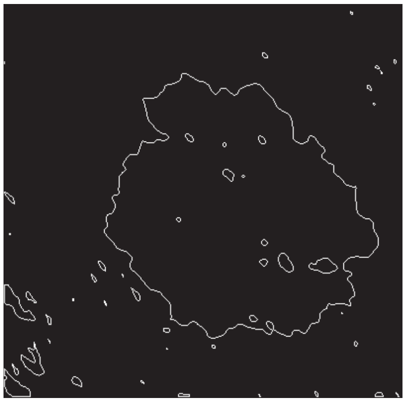

Figure 4.35: *Contours and holes of the image of the mole*

Figure 4.36 shows the result after selecting the biggest contour from the set of contours.

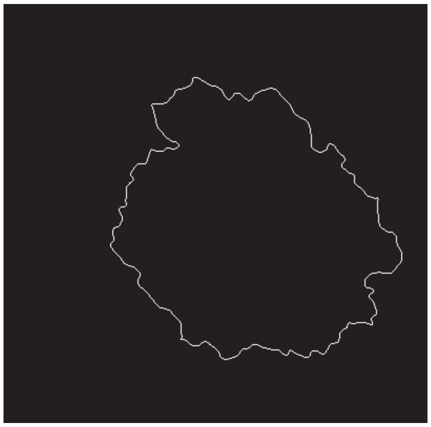

Figure 4.36: *Mole border*

Figure 4.37 shows the final result of the whole segmentation process.

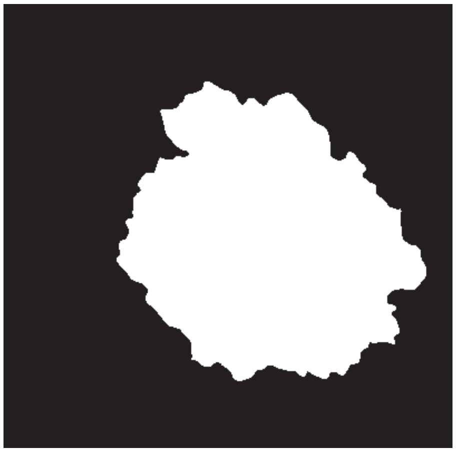

Figure 4.37: *Segmented mole*

On the other hand, when the thresholding process did not work effectively, the results are unpredictable. Figure 4.38 shows the result of merging of the six images for the bad segmented mole

Figure 4.38: *Merged segmented image for the image with challenging conditions (Figure 4.26)*

Figure 4.39 shows the result after finding all the contours and holes.

Figure 4.39: *Contours and holes for image with challenging conditions*

Figure 4.40 shows the result of selecting the biggest contour of the image.

Figure 4.40: *Wrong selection of the biggest border set*

The previous result shows that the biggest shape in the image was not the shape of the mole. Therefore, the final result of the segmented mole is incorrect, and therefore it was discarded. Figure 4.41 illustrates the bad segmented image.

Figure 4.41: *Wrong segmentation result of the mole image in Figure 4.26*

4.3.3 Feature extraction

4.3.3.1 Results of color coordinate Conversion

Figure 4.42 shows the RGB image converted to HSV.

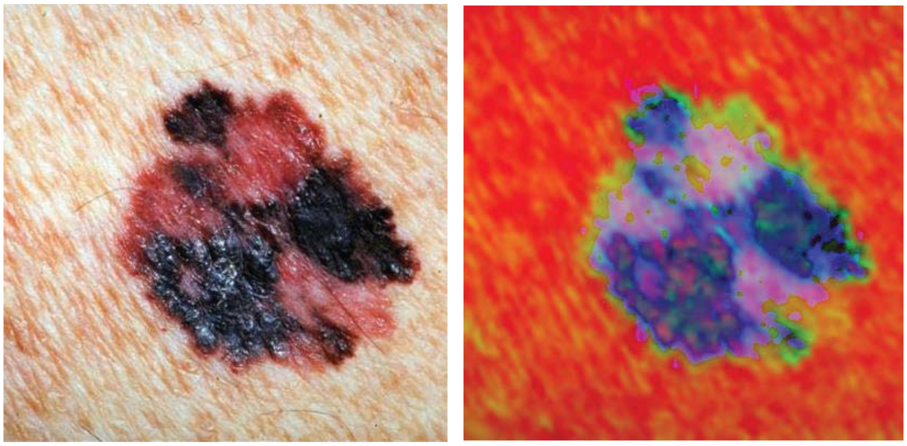

(a) (b)

Figure 4.42: *(a) RGB image converted to (b) HSV image*

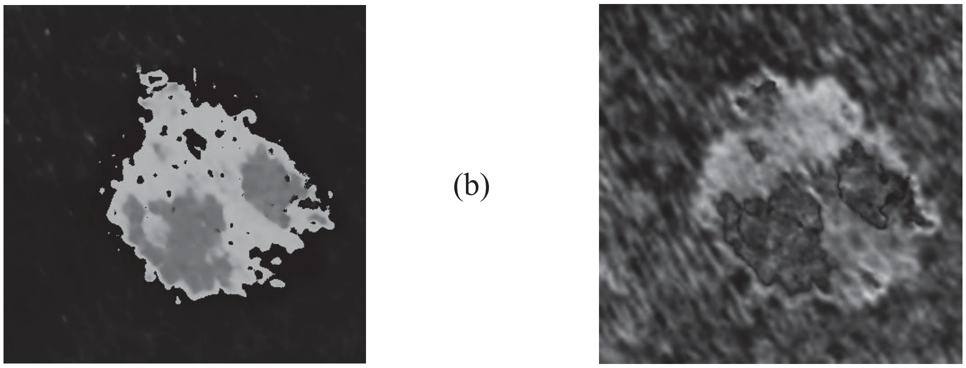

(a) (b)

(c)

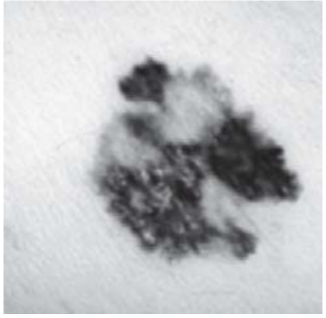

Figure 4.43: Skin mole images in *(a) Hue, (b) Saturation and (c) Value coordinate*

Figure 4.44 shows the Hue image resulting after shifting the hue values of the previous "Hue image" 90 degrees.

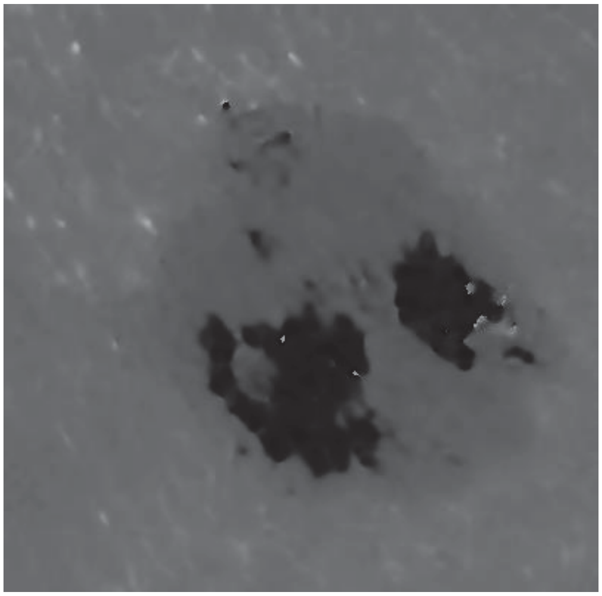

Figure 4.44: *Hue coordinate of a mole shifted 90 degrees*

4.3.3.2 Results for color feature extraction

Figure 4.45 shows a melanoma sample image and Figure 4.46 presents a sample benign mole image used in the followings sections.

In *Table 4.11* illustrates the percentage of total area for each region and for each skin mole sample. *Table 4.12* shows the results of the ratio of percentages of total area for each image region. When the skin mole has only one region, this feature is always 0.

Figure 4.45: *A typical melanoma sample image. (Diepgen & Yihune, 2013, with permission)*

Figure 4.46: *A typical benign mole sample. (Diepgen & Yihune, 2013, with permission)*

Table 4.11: Distribution of the percentage of total area for each image region

Image	**Region 1**	**Region 2**	**Region 3**	**Region 4**
Melanoma	25.17%	1.70%	73.13%	0,003%
Benign mole	0%	0%	100%	0%

Table 4.12: Ratio of percentage of area between image regions

Image / Regions	**1 / 2**	**1 / 3**	**1 / 4**	**2 / 3**	**2 / 4**	**3 / 4**
Melanoma	14.893	0.344	8073.5	0.023	544.5	23456
Benign mole	0	0	0	0	0	0

The melanoma sample image has pixels in the four regions, although region 2 and 4 have very small percentages. On the other hand, the benign mole has pixels distributed in one single region (3). In Figure 4.47 and Figure 4.48, the distribution of these regions in the skin images are shown.

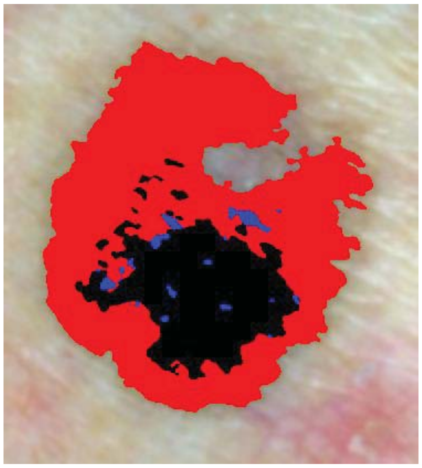

Figure 4.47: *Regions of the melanoma*

Figure 4.48: *Regions of the benign mole*

This result meets with the original idea that the melanomas often tend to have more than one single region, whereas the benign moles have one uniform color.

Table 4.13 presents the features extracted from the two images.

4.3.3.3 Asymmetry feature extraction

Figure 4.49 shows the the border of the melanoma extracted using Freeman Chain Code.

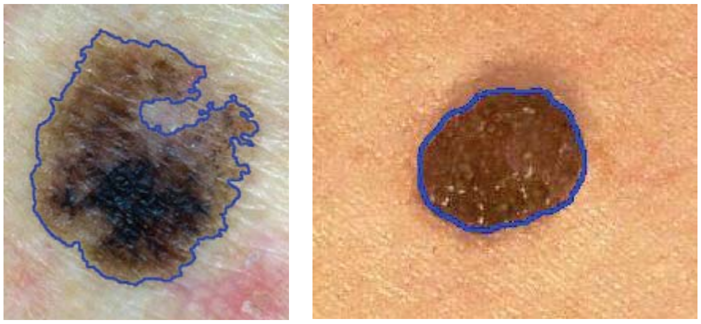

Figure 4.49*: A typical border images (melanoma and benign mole) using Freeman Chain Code*

Table 4.13: Features of the four regions

	Coordinate	**Region 1**				**Region 2**				**Region 3**				**Region 4**			
		Mean	St.Dev	Max	Min	Mean	St.Dev	Max	Min	Mean	St.Dev	Max	Min	Mean	St.Dev	Max	Min
Melanoma image	*Hue*	53.932	1132.03	150	0	33.080	183.787	57	0	101.744	57.013	118	60	150	0	150	150
	Saturation	84.163	1951.75	210	0	43.064	1421.62	157	3	79.839	807.996	185	0	3	0	3	3
	Value	47.677	165.065	69	9	86.729	177.599	131	70	117.425	603.686	175	70	75	4	77	73
Benign image	*Hue*	0	0	0	0	0	0	0	0	102.08	1.695	106	98	0	0	0	0
	Saturation	0	0	0	0	0	0	0	0	119.234	251.65	218	95	0	0	0	0
	Value	0	0	0	0	0	0	0	0	187.594	547.861	242	114	0	0	0	0

Figure 4.50 shows the enclosing rectangle and the two principal axes major L1 and minor L2 for both the images.

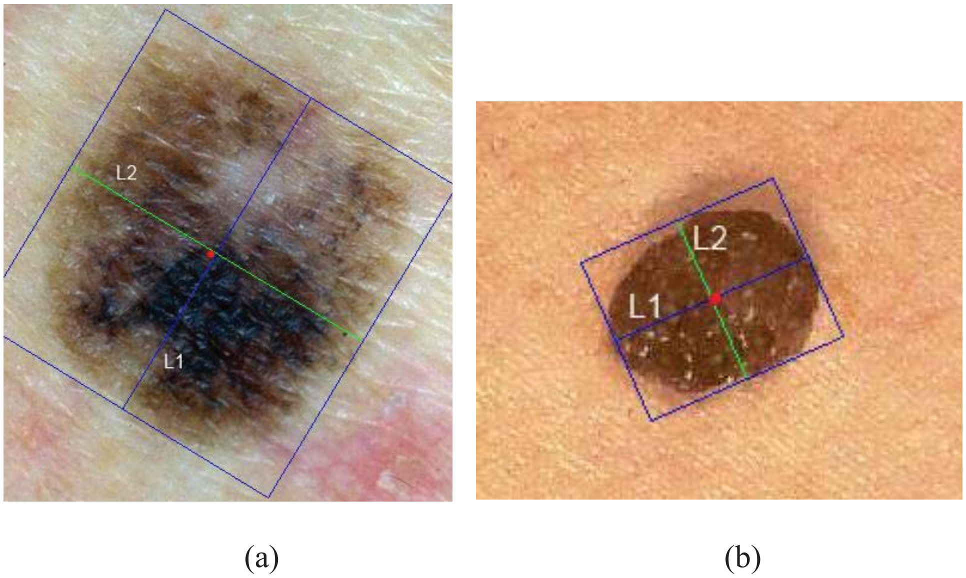

(a) (b)

Figure 4.50: *Bounding box, principal axes and centroid for the (a) melanoma and the (b) benign mole images*

The red point indicates where the centroid of the shape is. The centroid is separated from the center of the enclosing rectangle.

Table 4.14 shows typical values of different features obtained for the melanoma and the benign mole images.

Table 4.14: Feature values for the melanoma and benign images

Feature	**Melanoma**	**Benign mole**
Circularity	0.202	0.085
Compactness	0.278	0.778
Ratio of L2 and L1	0.935	0.819
Ratio of area melanoma and area enclosing rectangle	0.729	0.810
Ratio between left side of L1 and the melanoma area	0.533	0.508
Ratio between right side of L1 and the melanoma area	0.491	0.544
Ratio between left side of L2 and the melanoma area	0.492	0.495
Ratio between right side of L2 and the melanoma area	0.532	0.557
Ratio between convex hull area and mole area	0.872	0.993
Distance of centroid to the center of the rectangle	5.267	1.973
Invariant moment 1	0.175	0.164
Invariant moment 2	6.90E-04	1.26E-03
Invariant moment 3	4.36E-05	2.18E-05
Invariant moment 4	2.11E-05	2.07E-07
Invariant moment 5	-4.50E-10	2.53E-13
Invariant moment 6	2.74E-07	4.70E-09
Invariant moment 7	-4.54E-10	3.61E-13

Ratio of projected area along L1	0.116	0.058
Ratio of projected area along L2	0.151	0.086

4.3.3.4 Border feature extraction

Figure 4.51 and Figure 4.52 show the process to create the 8 pixel thick border of the melanoma sample image. Figure 4.51 and Figure 4.52 illustrate the dilated and eroded segmented mole images

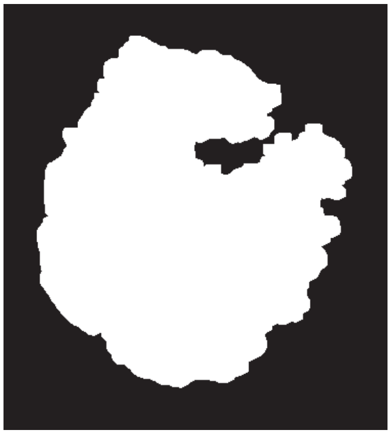

Figure 4.51: *Dilated melanoma* $I_{dilated}$

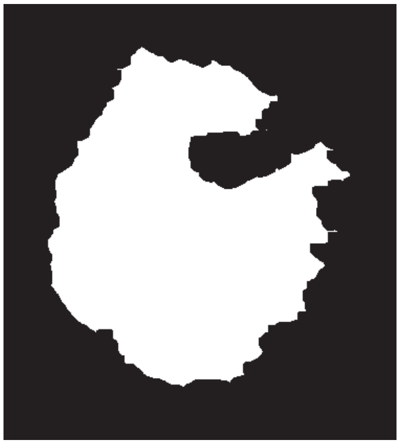

Figure 4.52: *Eroded melanoma* I_{eroded}

Figure 4.53 shows I_{outer} and I_{inner} of the mole.

Finally, Figure 4.54 presents the result of merging the outer border with the inner border to obtain the 8 pixel thick mole border I_{border}.

The following Figure 4.55 presents the RGB result of the border of the melanoma $I_{colorborder}$ and the RGB inner region $I_{colorinner}$. These two images are used afterwards to obtain all the color features.

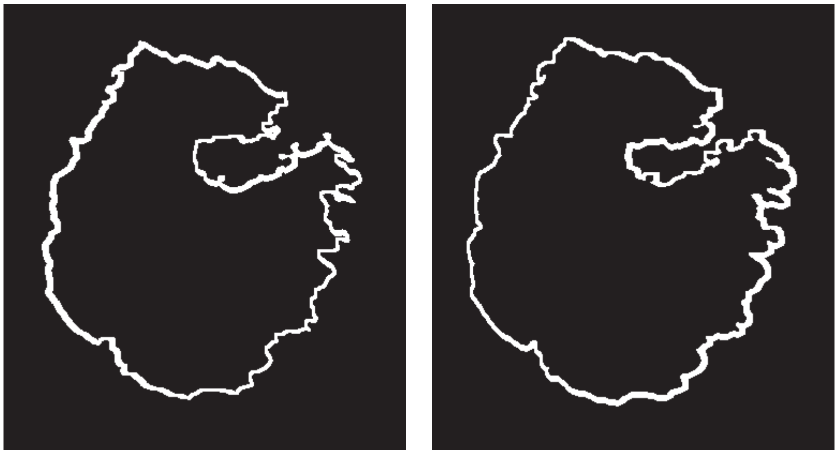

(a) (b)

Figure 4.53: *(a)* I_{outer} *and (b)* I_{inner} *images*

Figure 4.54: *8 pixel thick mole border* I_{border}

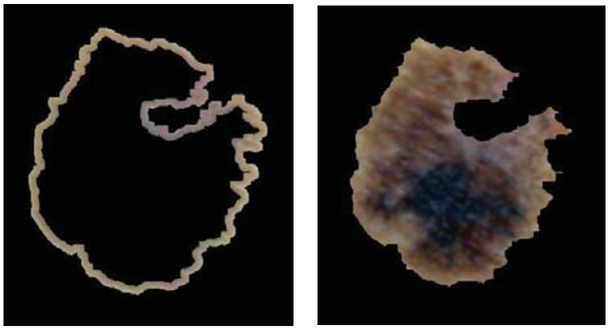

Figure 4.55: $I_{colorborder}$ *and* $I_{colorinner}$ *of the mole image*

Table 4.15 presents the color features for $I_{colorborder}$ of the two skin cancer samples.

4.3.3.4.1 Border unevenness features

Figure 4.56 shows the result after applying Sobel operator in (x) (horizontal, Ix') and (y) domain (vertical, Iy') respectively. Figure 4.57 shows the merged result of these two images.

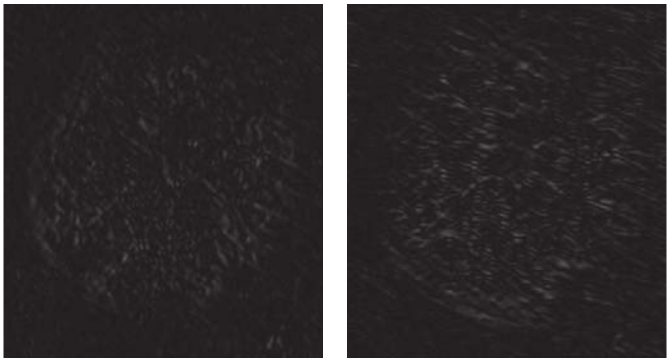

(a) (b)

Figure 4.56: *(a)* $\boldsymbol{Ix'}$ *and (b)* $\boldsymbol{Iy'}$ *for the segmented mole image*

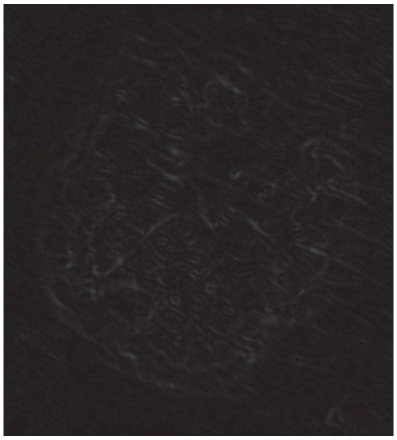

Figure 4.57: *Edges detected in the mole image using Sobel operator*

Table 4.15 lists the results of the border magnitude and variation in direction features for the melanoma and benign mole samples.

Table 4.15: Magnitude and Variation of direction features

Feature	**Melanoma**	**Benign mole**
μ Magnitude	27.82	44.269
σ Magnitude	13.65	17.42
Variation of direction	0.557	0.452

Table 4.16: Border color features of the melanoma and benign mole

	Coordinate	Region 1				Region 2				Region 3				Region 4			
		Mean	St.Dev	Max	Min	Mean	St.Dev	Max	Min	Mean	St.Dev	Max	Min	Mean	St.Dev	Max	Min
Melanoma image	*Hue*	0	0	0	0	28.833	318.606	54	0	105.629	56.890	119	60	123.696	67.516	150	120
	Saturation	0	0	0	0	8.783	11.136	17	2	62.449	413.822	127	2	30.348	127.792	41	2
	Value	0	0	0	0	148.100	86.590	167	128	154.925	195.016	200	112	164.174	73.796	174	139
Benign image	*Hue*	0	0	0	0	0	0	0	0	101.309	1.574	105	98	0	0	0	0
	Saturation	0	0	0	0	0	0	0	0	151.111	628.457	240	109	0	0	0	0
	Value	0	0	0	0	0	0	0	0	163.816	1191.540	241	98	0	0	0	0

4.3.4 Feature analysis

In total, 197 features were extracted from each image.

Table 4.18 presents statistical parameters ($\mu, \sigma,$ maximum and minimum) for selected asymmetry features.

Figure 4.58 shows the distribution of values of the feature of compactness. The plot illustrates the overlap present in the compactness feature. Table 4.17 illustrates the mean and standard deviation for this feature. Therefore, assuming these distributions are normal (there are more than 30 samples), the 95% confidence intervals for both groups are as follow (*Table 4.17*):

Table 4.17: 95% confidence interval

Melanoma group	$(0.252, 0.860)$
Benign group	$(0.595, 0.947)$

Figure 4.59 shows the distribution of values for the distance of the centroid to the center of the bounding box. There is a clear outlier in the melanoma group (35.87). Also, the histogram shows some degree of overlap between both groups.

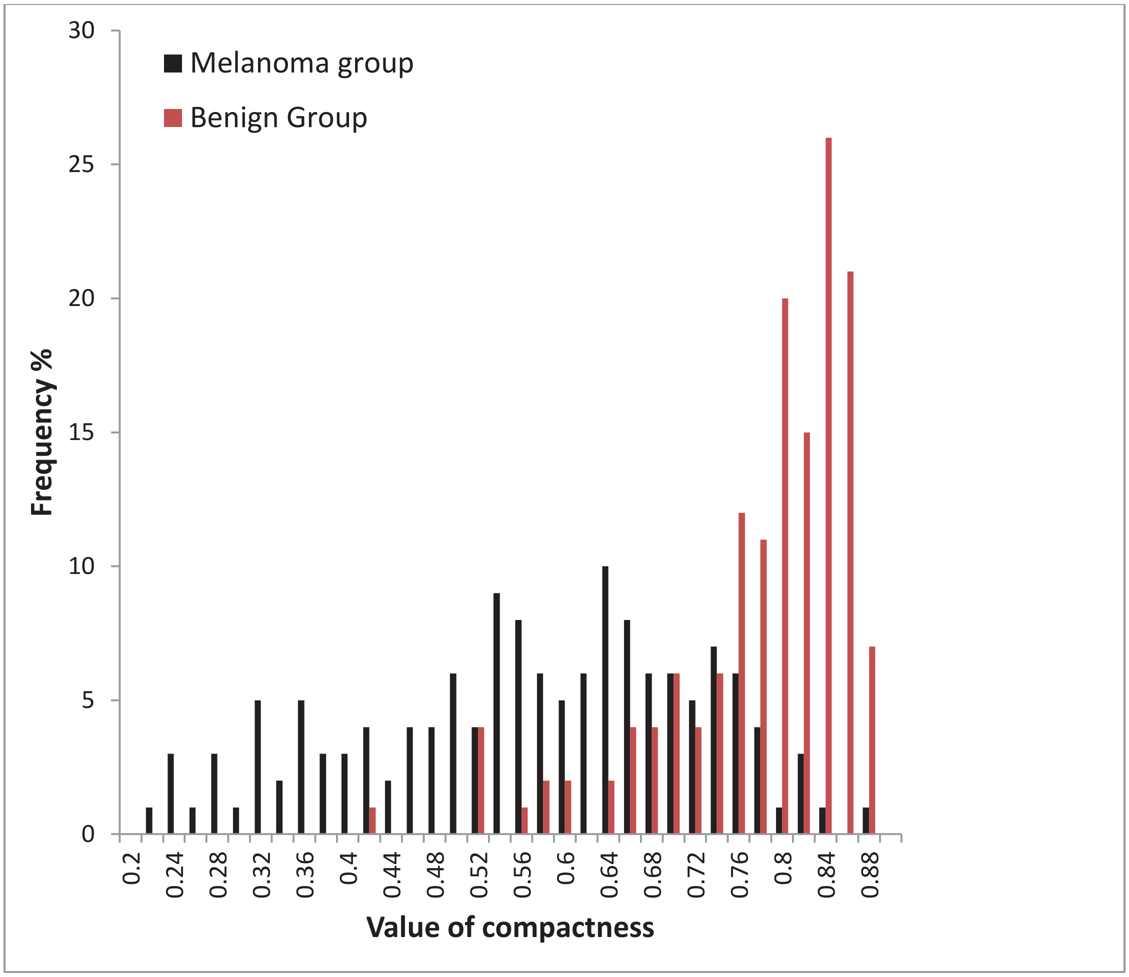

Figure 4.58: *Plot of distribution of compactness*

Figure 4.60 shows the correlation between these two features. The coefficient of correlation is -0.63 (equation: $y = mx + c$). Therefore, there is a moderate dependence between asymmetry features. Hence, it is required to remove redundancy from dataset.

Table 4.18: Statistical information of asymmetry features

Asymmetry Features	$\mu_{melanoma}$	μ_{Benign}	$\sigma_{melanoma}$	σ_{Benign}	**Max Melanoma**	**Max Benign**	**Min Melanoma**	**Min Benign**
Compactness	0.556	0.771	0.152	0.088	0.863	0.880	0.219	0.413
Circularity	0.169	0.120	0.070	0.053	0.471	0.270	0.052	0.037
Ratio convex hull	0.902	0.961	0.052	0.021	0.979	0.987	0.663	0.863
Ratio melanoma area	0.710	0.767	0.052	0.030	0.835	0.841	0.478	0.675
Distance centroid	6.186	2.088	4.849	2.024	35.748	11.490	0.222	0.126
Ratio region 1	0.508	0.527	0.053	0.037	0.646	0.645	0.372	0.422
Projected area L1	0.154	0.103	0.064	0.044	0.362	0.252	0.035	0.023
Projected area L2	0.149	0.096	0.075	0.047	0.482	0.342	0.046	0.027
Invariant moment 1	0.182	0.171	0.023	0.011	0.310	0.215	0.161	0.160
Invariant moment 2	5.79E-03	3.30E-03	7.61E-03	3.87E-03	5.20E-02	2.04E-02	1.76E-06	3.00E-05

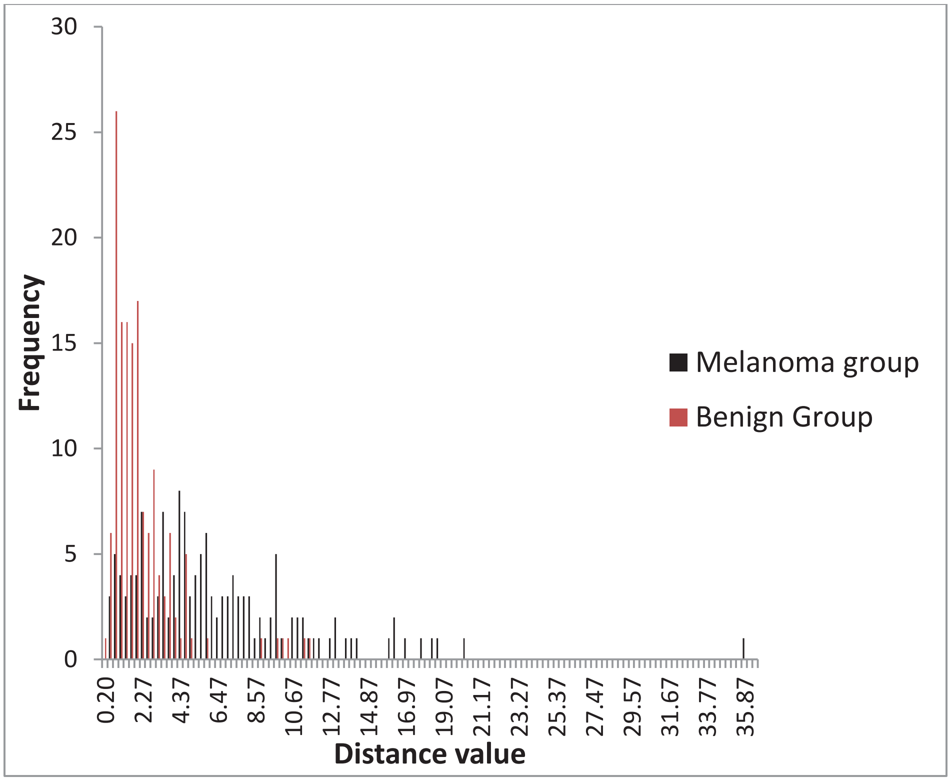

Figure 4.59: G*raph of distance from centroid to the center of the enclosing rectangle*

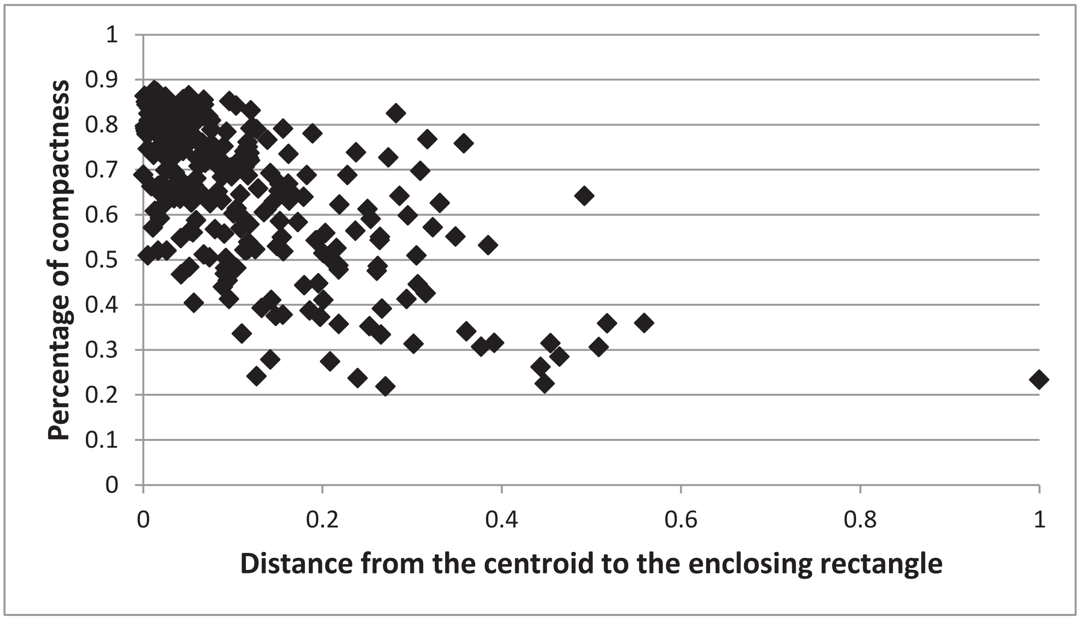

Figure 4.60: *Correlation of compactness and distance*

4.3.4.1 Color feature analysis

Table 4.19 presents the statistics of percentage of total area for each color region.

Table 4.19: Statistical information regarding percentage of total area for each region

Group	**Parameter**	**Area region 1**	**Area region 2**	**Area region 3**	**Area region 4**
Melanoma	μ	0.194	0.060	0.723	0.022
	σ	0.239	0.136	0.278	0.077
	Max	0.890	0.632	1.000	0.695
	Min	0.000	0.000	0.104	0.000
Benign	μ	0.126	0.036	0.824	0.003
	σ	0.219	0.128	0.281	0.018
	Max	0.981	0.754	1.000	0.196
	Min	0.000	0.000	0.000	0.000

Color features have also overlap. For instance, Figure 4.61 shows that the feature is totally overlapped.

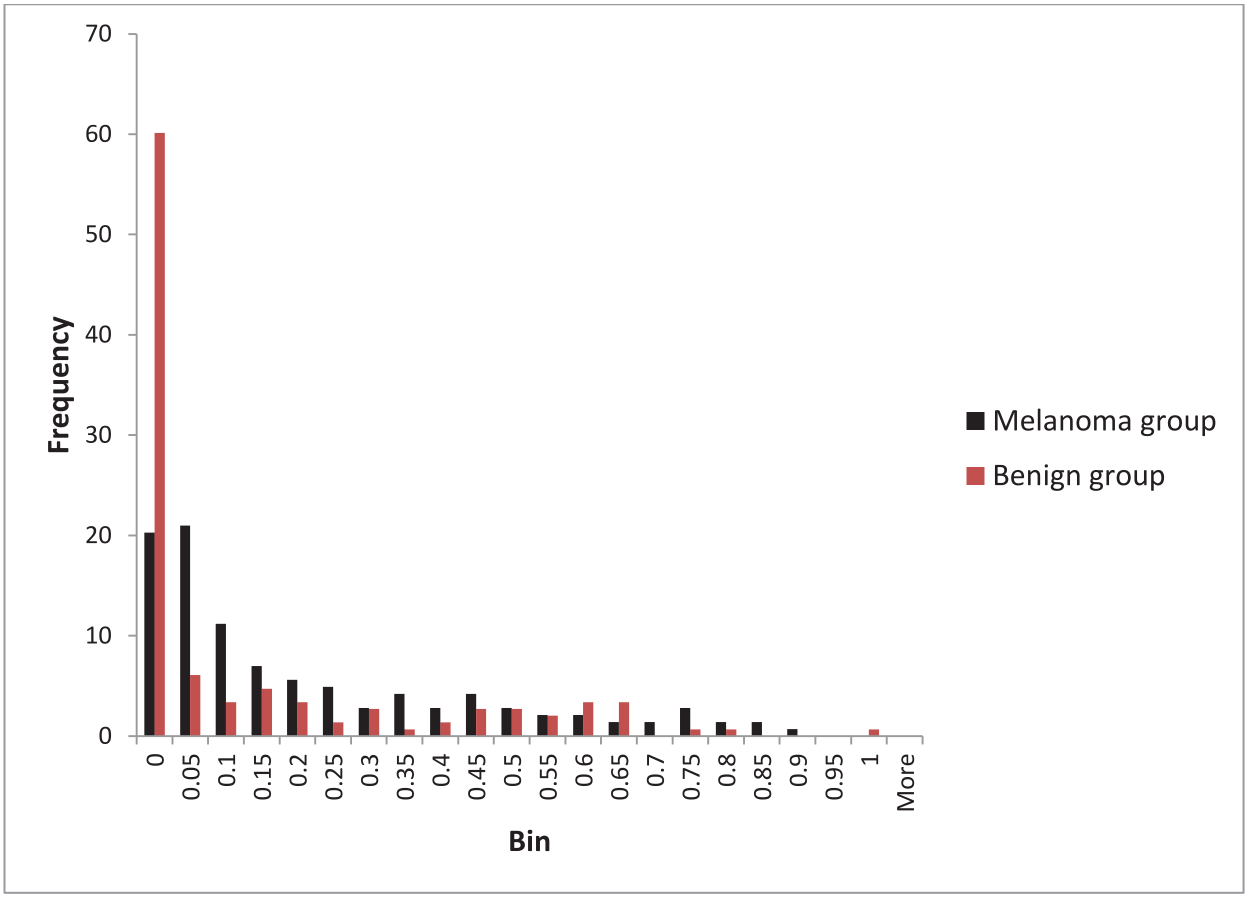

Figure 4.61: *Distribution for region 1 feature*

In general, all the color features are found to have a high degree of overlap.

4.3.4.2 Border feature analysis

Border features indicated the same issue as color features. Figure 4.62 illustrates the relationship of percentage of total mole area in region 3 in the border image $I_{colorborder}$ and in the inner image $I_{colorinner}$.

The classification criteria is that the melanomas have border of different colors and darker than inner regions.

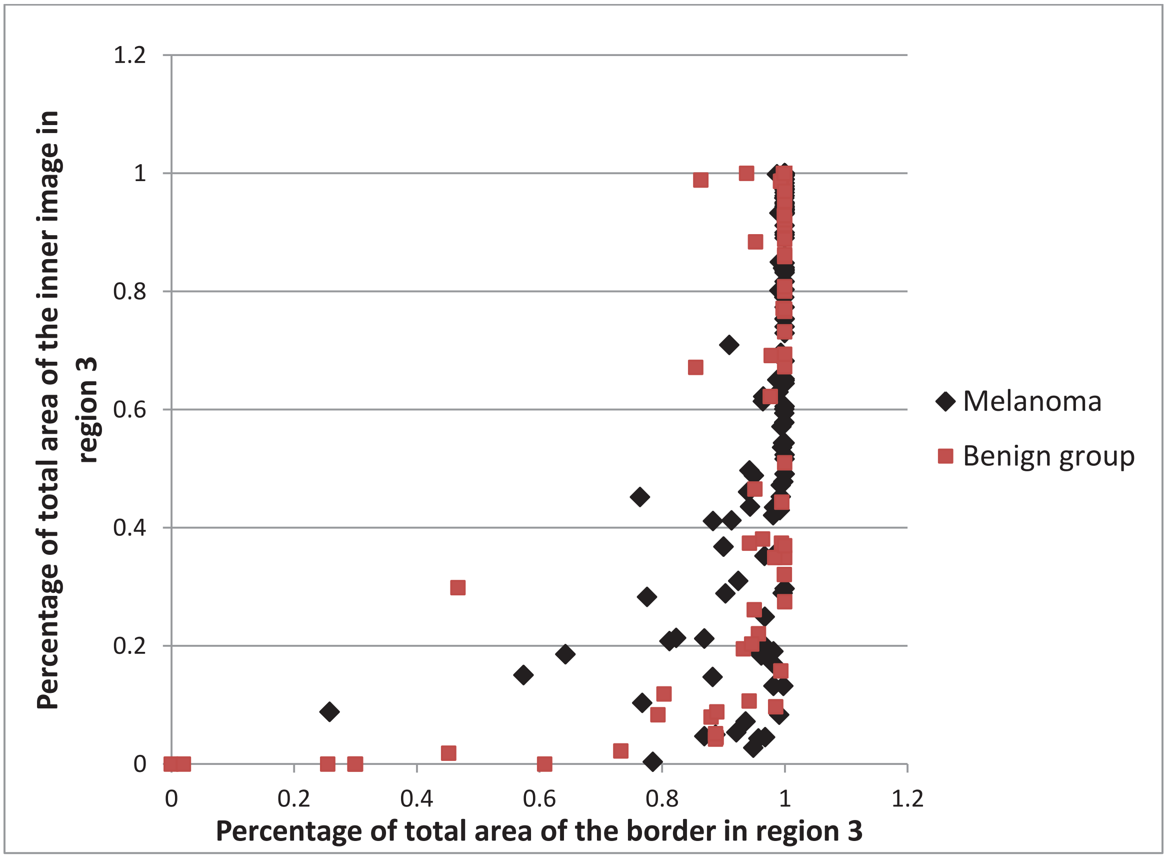

Figure 4.62: *Ratio of percentage of total area in border and percentage of total area in inner for region 3*

Border features show a lot of overlap. Figure 4.63 shows the distribution of the minimum value in Value coordinate in HSV. Although the melanoma group have 80% of the samples in the value 70, there is still a lot of overlap.

Figure 4.64 illustrates the distribution of the average of differences in direction code changes using Freeman Chain Code. As we mentioned before, color and border features present more overlap than asymmetry features.

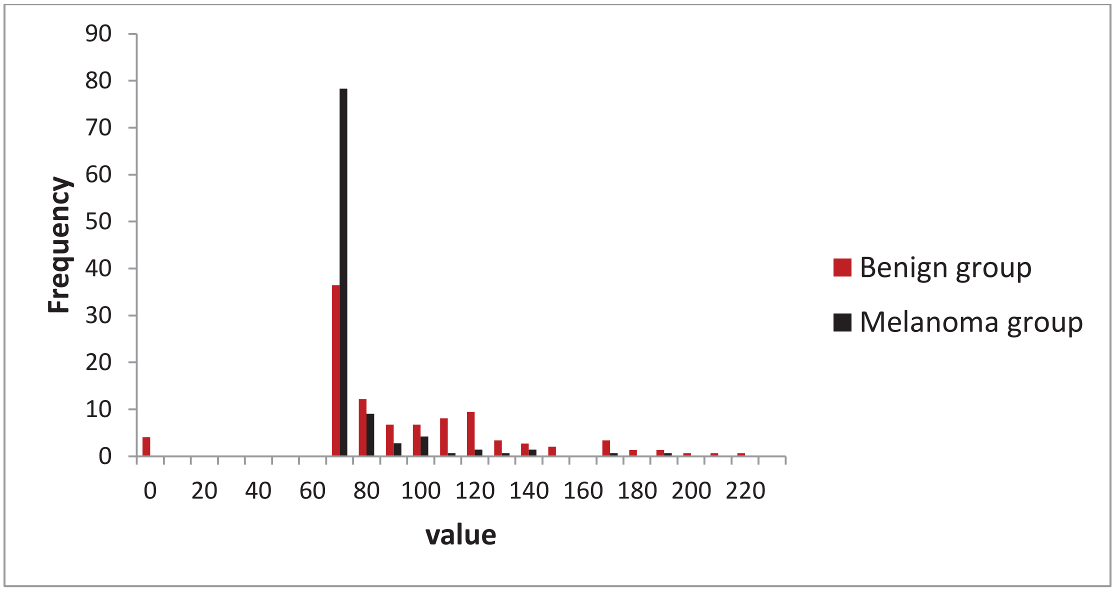

Figure 4.63: *Plot of minimum value in Value coordinate (HSV) of region 3 for inner regions of the mole*

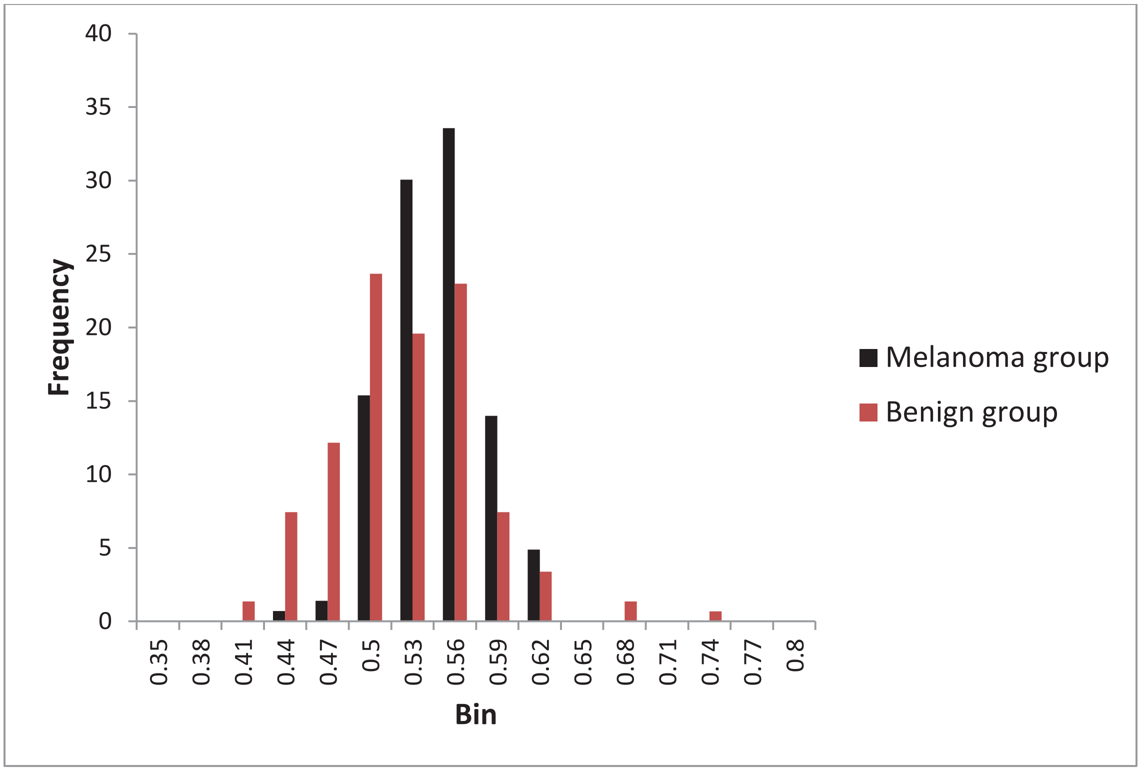

Figure 4.64: *Average of difference in direction code change (Freeman Chain Code)*

In conclusion, neither color nor border features separate accurately the two groups. However, the classifier works in a higher dimension feature than two dimensions. Also, the dependency between features could be reduced by using PCA. Therefore, even though this overlap is not desired, the results could still be acceptable. Due to lack of time, it was not possible to find new features to define color and border.

Figure 4.65, Figure 4.66. Figure 4.67 show 3D plots of different asymmetry, color and border features. They illustrate a relatively better separability amongst groups.

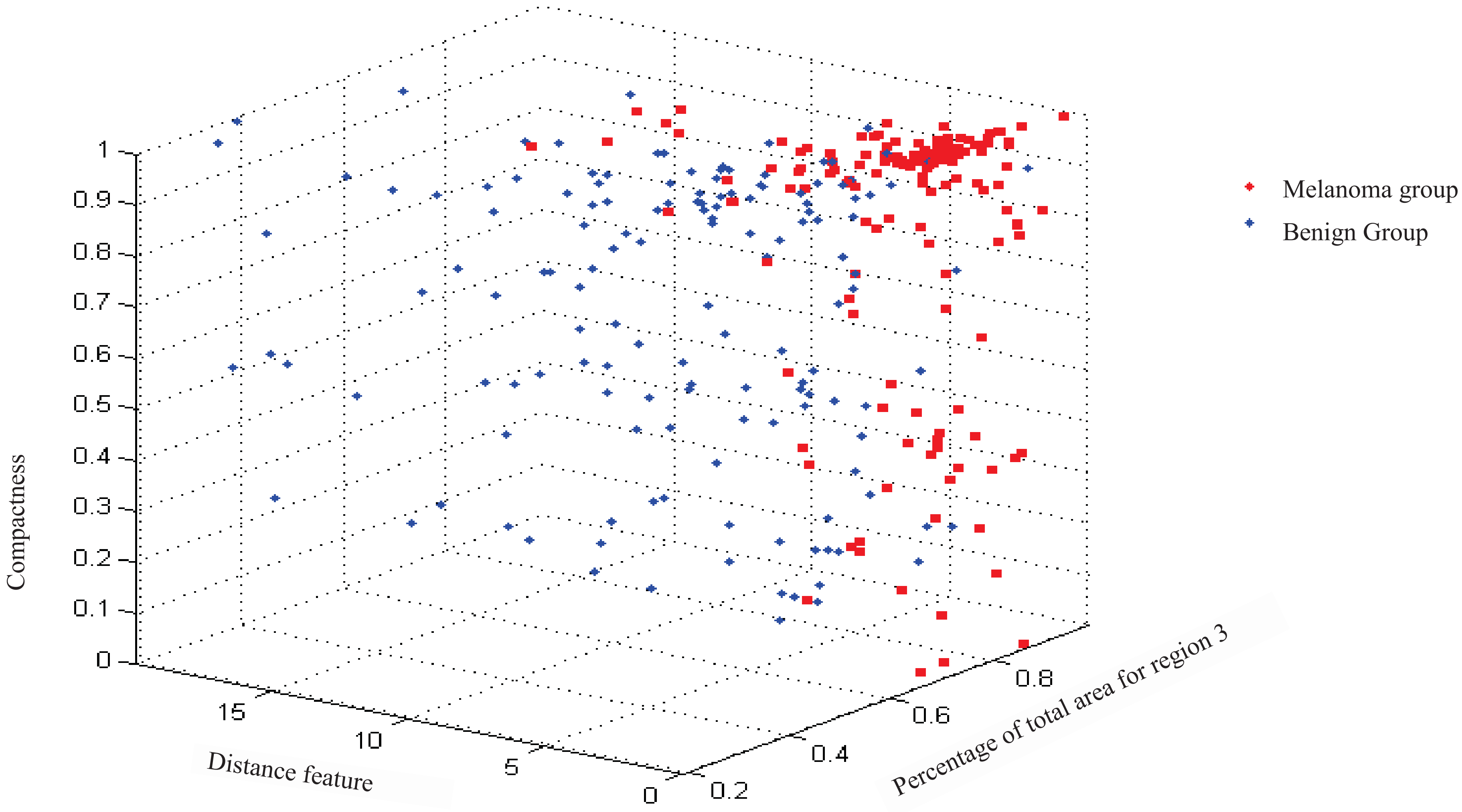

Figure 4.65: *Relationship between compactness, distance from the centroid to the center of the enclosing rectangle and percentage of total area for region 3*

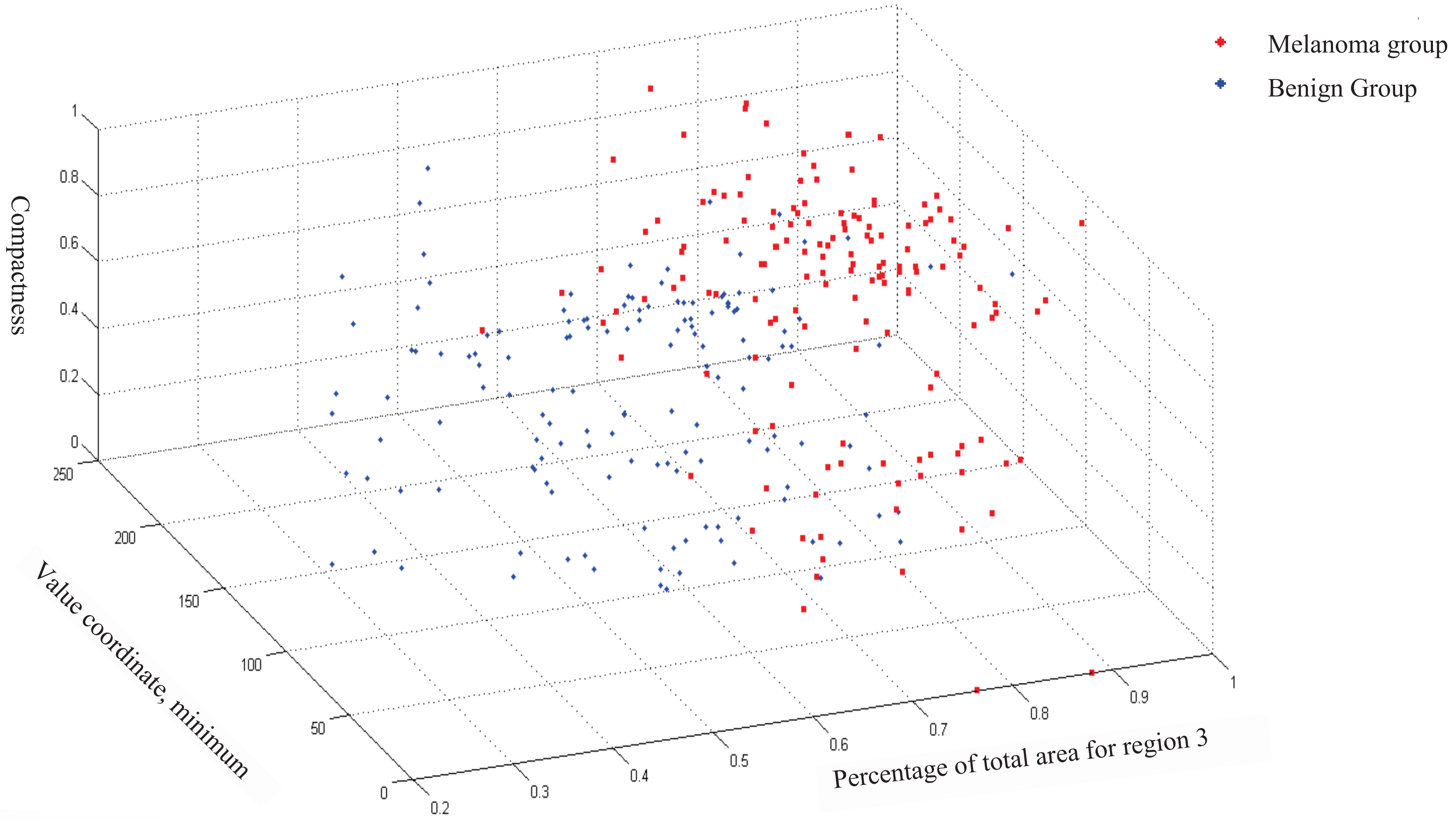

Figure 4.66: *Relationship of compactness, minimum value in Value coordinate for region 3, and percentage of total area for region 3*

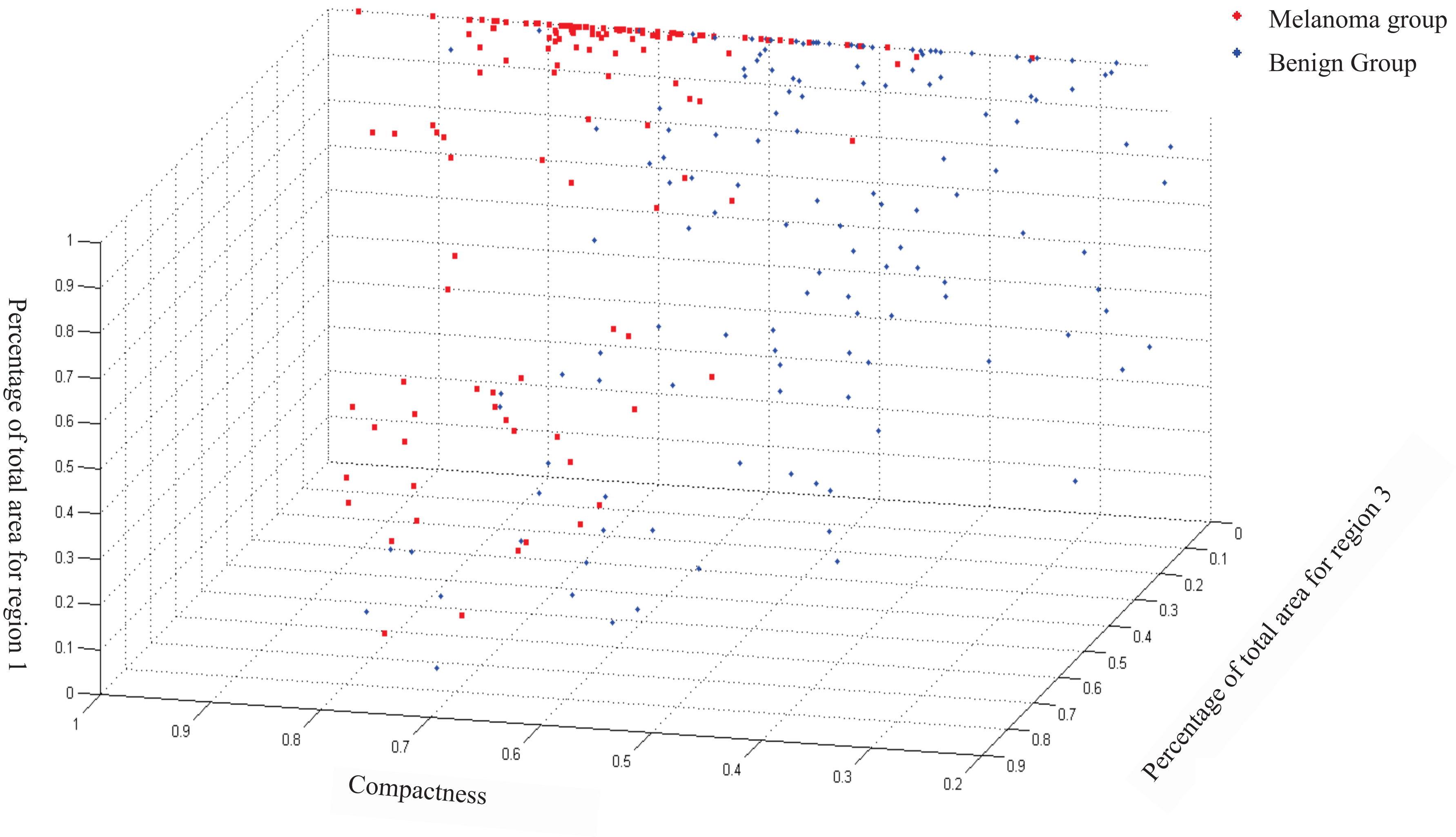

Figure 4.67: *Relationship between compactness, percentage of total area for region 1 and percentage of total area for region .*

After this analysis, the conclusion is that asymmetry features are the most important features. However, as seen from 3-D plots, color and border features showed some added discrimination in the feature set.

4.3.5 Classification results

The feature set with 197 features is reduced using principal component analysis. *Table 4.20* shows the eigenvalues and the cumulative explained variation until 98%.

Table 4.20: Eigenvalues and the cumulative percentage

#	**Eigenvalue**	**% variation explained**	**Cumulative %**
1	46.890	23.78%	23%
2	18.803	9.54%	33%
3	17.574	8.91%	41%
4	11.137	5.65%	47%
5	9.477	4.81%	51%
6	8.582	4.35%	55%
7	6.726	3.41%	59%
8	6.255	3.17%	62%
9	5.490	2.78%	65%
10	4.328	2.20%	67%
11	3.957	2.01%	69%
12	3.830	1.94%	72%
13	3.545	1.80%	73%
14	3.221	1.63%	75%
15	3.036	1.54%	77%
16	2.940	1.49%	78%
17	2.765	1.40%	80%
18	2.438	1.24%	81%
19	2.401	1.22%	82%
20	2.131	1.08%	83%
21	2.028	1.03%	85%

#	Eigenvalue	% variation explained	Cumulative %
23	1.852	0.94%	87%
25	1.495	0.76%	88%
26	1.444	0.73%	89%
27	1.418	0.72%	90%
28	1.301	0.66%	90%
29	1.190	0.60%	91%
30	1.082	0.55%	92%
31	1.053	0.53%	92%
32	0.988	0.50%	93%
33	0.883	0.45%	93%
34	0.819	0.42%	94%
35	0.790	0.40%	94%
36	0.745	0.38%	94%
37	0.714	0.36%	95%
38	0.635	0.32%	95%
39	0.622	0.32%	95%
40	0.546	0.28%	96%
41	0.524	0.27%	96%
42	0.488	0.25%	96%
43	0.481	0.24%	96%
44	0.445	0.23%	97%
45	0.433	0.22%	97%
46	0.384	0.19%	97%
47	0.365	0.19%	97%
48	0.334	0.17%	97%
49	0.328	0.17%	97%
50	0.310	0.16%	98%

Due to the fact that there is quite feature dependence between the feature set, only the first four principal components increase the cumulative percentage significatively. The rest of principal components only added a very small percentage of variation. This means that the feature set shows high levels of dependency. Due to the short time available, it was not possible to investigate more features to reduce this dependency.

In this study, 50 principal components were used.

The next step was to tune the SVM classification method with the pair (C, γ). The plot in Figure 4.68 shows the accuracy yielded for each pair of values (C, γ).

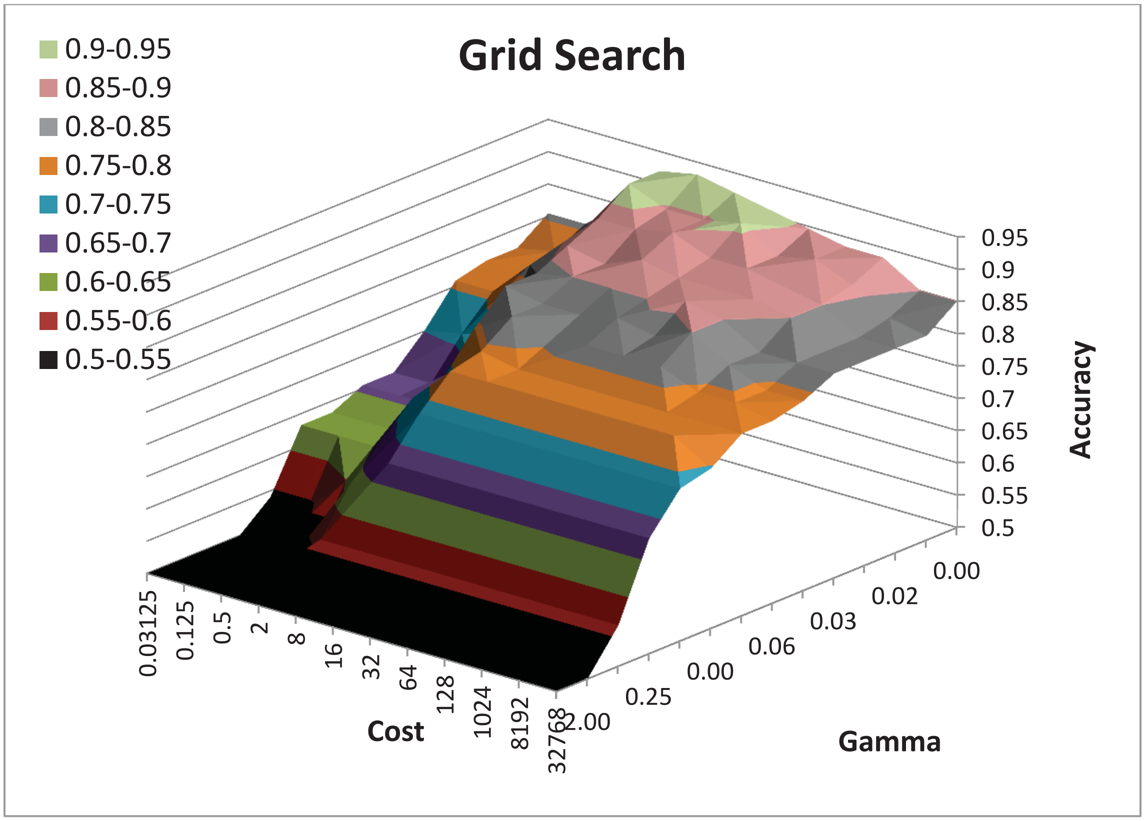

Figure 4.68: *Parameter pair configuration*

The best pair (C, γ) found is $(8, 2^{-8})$

The accuracy of the training group of 204 images was 95.10%.

The accuracy obtained for validation using the test group of 87 images was 93.10% (81 images classified correctly from 87). The sensitivity was 92.68%, (38 images classified correctly from 41). The specificity was 93.48%, (43 images classified correctly from 46).

4.3.5.1 Discussions of the skin moles misclassified

Table 4.21 and *Table 4.22* shows the results of the classification for the training and testing groups. The results are expressed as the distance of the skin sample image to the hyper plane found after training SVM. *Table 4.23* presents the error for each misclassified image. When a melanoma is misclassified, it is assigned a negative value and when a benign mole is misclassified it is assigned a positive value. The further from 0 the more error is present in the classification of the skin sample.

Table 4.21: Results of the classification for the training group

Training group melanomas		**Training group benign moles**	
File name	**Margin distance**	**File name**	**Margin distance**
2.png	1	157.png	-1.10503
4.png	1	160.png	0.852741
5.png	1	162.png	-1
8.png	1	163.png	0.186993
9.png	1.532202	165.png	-1
10.png	2.401164	166.png	-0.16348
11.png	0.522883	167.png	-1.46786
12.png	2.385023	168.png	-0.26154
13.png	0.959265	169.png	-1.44437
14.png	1.469082	170.png	-1
15.png	1	171.png	0.366608
16.png	1.1808	172.png	-1
17.png	1.977776	173.png	-1
18.png	1.957663	174.png	-1.42592
19.png	1	178.png	-1.00338
20.png	2.402991	179.png	-1
22.png	1	180.png	-2.3292
24.png	1.569749	181.png	-2.14147
26.png	0.015234	183.png	-1

Training group melanomas		**Training group benign moles**	
File name	**Margin distance**	**File name**	**Margin distance**
28.png	1	186.png	-1
29.png	1.003569	188.png	-1
30.png	2.365454	189.png	-1.63986
33.png	2.297106	193.png	-1.48023
34.png	2.604464	194.png	-1.03634
36.png	-0.20577	195.png	-1.26233
37.png	1.327031	196.png	-1.32326
38.png	1.955363	197.png	-1.92645
39.png	1	198.png	-1
41.png	-0.45211	201.png	-0.54662
44.png	1	204.png	-2.33323
46.png	1	208.png	-2.09079
48.png	1	212.png	-1.73967
49.png	1	214.png	0.109984
50.png	1	215.png	-0.80265
51.png	1	217.png	-1
53.png	1.046532	218.png	-1
54.png	1	219.png	-1
56.png	1	220.png	0.009855
57.png	1.081858	221.png	-1.97428
58.png	1	222.png	-1
68.png	0.875498	224.png	-1
78.png	0.286778	225.png	-1.23096
79.png	1.098169	226.png	-0.4014
80.png	1	227.png	-0.70725
84.png	1	228.png	-1
85.png	0.334793	229.png	-0.39636
86.png	1	230.png	-1
87.png	0.877274	231.png	-1.85667
88.png	1	232.png	-1
90.png	1	233.png	-1
91.png	1	235.png	-1
92.png	1	236.png	-1.6016
93.png	1.06599	237.png	-1.98189
95.png	1.865355	238.png	-1

Training group melanomas		Training group benign moles	
File name	Margin distance	File name	Margin distance
96.png	0.764116	242.png	-1
97.png	1.890316	246.png	-2.55654
99.png	1.33986	249.png	-1
100.png	1.961082	251.png	-1.87834
102.png	1.320213	253.png	-1
103.png	2.28781	254.png	-1.90168
104.png	1	256.png	-1
106.png	1	257.png	-2.88185
107.png	0.826657	258.png	-2.77883
108.png	1.271537	259.png	-1.96754
109.png	1.662553	260.png	-1.78689
110.png	1	261.png	-2.12019
111.png	1	262.png	-2.61242
112.png	0.874741	263.png	-0.91189
114.png	1.216511	264.png	0.476625
116.png	1	266.png	-1.568
123.png	1.271723	271.png	-0.33322
125.png	1.185128	272.png	-1.04308
126.png	3.043072	273.png	-1
127.png	1.609126	275.png	-0.29827
128.png	2.441176	276.png	-1
129.png	0.768398	278.png	-1
130.png	0.270425	279.png	-1
131.png	1	281.png	-2.00497
132.png	-1.30247	283.png	-1
133.png	1	284.png	-1.11485
135.png	0.669454	285.png	-1.50351
137.png	1	286.png	-2.38983
138.png	0.433657	287.png	-1
139.png	0.31095	289.png	-1.9992
140.png	1.411776	290.png	-1.24368
141.png	0.280362	291.png	-1
142.png	1.89335	292.png	-1.48999
144.png	1	293.png	-1.74736
146.png	2.189036	294.png	-1

149.png	-0.47807	295.png	-1.33004
150.png	0.929454	298.png	-0.63402
151.png	1	299.png	-1.87606
153.png	1	302.png	-1
154.png	1	303.png	-1
156.png	1.208473	304.png	-1.25213

Table 4.22: Results of the classification for the test group

Test group melanomas		**Test group benign moles**	
File name	**Margin distance**	**File name**	**Margin distance**
0.png	2.196831	158.png	-0.11932
1.png	1.167489	159.png	0.381959
3.png	0.259615	161.png	-0.29927
6.png	0.503649	164.png	1.154557
7.png	1.626604	175.png	-0.33012
21.png	1.083566	176.png	-2.38293
23.png	1.130823	177.png	-1.38995
25.png	2.514342	182.png	-0.24891
27.png	1.441288	184.png	-1.06412
32.png	2.009149	185.png	-1.04677
35.png	0.533365	187.png	-1.21157
40.png	0.268869	190.png	-0.48633
43.png	0.78466	192.png	-2.1511
52.png	0.373035	199.png	0.243054
55.png	1.366966	200.png	-1.29814
59.png	2.400729	203.png	-1.61377
60.png	0.61304	206.png	-0.47095
61.png	1.374684	207.png	-0.73199
66.png	1.028947	209.png	-1.36656
81.png	0.299114	210.png	-0.65158
82.png	-1.25535	213.png	-1.37512
83.png	0.27429	216.png	-0.45274
89.png	1.163735	223.png	-0.50035
94.png	0.811933	234.png	-1.05
98.png	0.049243	239.png	-1.36999

Test group melanomas		Test group benign moles	
File name	Margin distance	File name	Margin distance
101.png	2.018426	240.png	-0.37956
105.png	1.060318	241.png	-0.09027
113.png	0.227975	243.png	-1.81061
115.png	0.839565	244.png	-2.03265
117.png	0.230778	245.png	-1.90552
120.png	1.596229	247.png	-0.16458
122.png	-0.11882	248.png	-1.23359
124.png	0.421455	250.png	-2.61477
134.png	0.526688	252.png	-1.56519
143.png	1.503744	265.png	-0.89008
145.png	0.407802	270.png	-1.2436
147.png	0.22787	274.png	-0.58506
148.png	-1.20991	277.png	-1.88492
152.png	2.060777	280.png	-1.7969
155.png	0.578454	282.png	-1.44268
		296.png	-0.22248
		297.png	-0.85913
		300.png	-1.14152
		301.png	-1.07715

Table 4.23: Error for the misclassified images

Image filename	Error
82.png	-1.25535
122.png	-0.11882
148.png	-1.20991
159.png	0.381959
164.png	1.154557
199.png	0.243054

4.3.5.2 Previous works

Table 4.24 illustrates the classification results of previous works on skin cancer classification with another set of skin images and other classification algorithms. Our results are lower than the work from Cavalcanti & Scharcanski. They used K-nearest neighbors with Decision Tree Classifier on 220 images. Their training set is bigger because they used Bootstrap Resampling method to increase the number of samples. In comparison with the other two works, our method provided better results in overall. Alcon´s work (2009) used the same dataset of images as Cavalcanti´s research and Adaboost with correlation based feature selection for classification. The specificity obtained is lower than that obtained in our research. Finally, the work of Amelard (2012) showed a similar result. Their dataset is smaller, and they used less features. In conclusion, our study provided optimal accuracy given our small data set.

Table 4.24: Comparison of other classification results

Authors	**Classifier**	**Accuracy**	**Sensitivity**	**Specificity**
Thesis research	SVM with RBF	93.10%	92.68%	93.48%
(Amelard, Wong, & Clausi, 2012)	SVM without kernel	86.89%	91.60%	80.46%
(Cavalcanti & Scharcanski, 2011)	K-NN with Decision tree	96.71%	96.26%	97.78%
(Alcón et al., 2009)	Adaboost with Correlation based feature	86%	94%	68%

CHAPTER 5. CONCLUSIONS AND FUTURE WORK

5.1 Conclusions

The following conclusions are derived from this study:

1. Cameras with at least 1 MP have enough resolution for basic telemedicine applications.
2. Modern smartphones are a powerful tool to develop telemedicine applications. Our research indicates the feasibility to develop a computer aid telemedicine application.
3. Front lighting work well to acquire simulated images of moles (simulated). The images obtained with the Samsung Galaxy SII are relatively brighter. However, the three configurations yield good results with this smartphone.
4. 50 principal components accounted for 98% of the variation. And the accuracy of the training group of 184 images is 95.10%.
5. The accuracy obtained for validation using the testing group of 87 images is 93.10%
6. The sensitivity is 92.68% and the specificity is 93.48%

5.2 Future work

Due to limitations in time, it is not possible to acquire skin images with the smartphone camera. The datasets of images are obtained from reliable internet sources. However, the smartphone telemedicine application needs to be tested to classify skin cancer images using smartphone camera systems.

Moreover, the classification algorithm used only asymmetry, color and border features to classify melanomas. Color and border features presented a lot of overlap. Therefore, further investigation is needed to find other features which could discriminate two groups. Also, texture features are not included in this research. Texture is an important feature, and very descriptive to differentiate melanomas from benign moles and used in previous works for classification (Alcón et al., 2009). Therefore, texture features could be evaluated to improve the overall accuracy of detecting melanomas.

REFERENCES

REFERENCES

Adams, R., & Bischof, L. (1994). Seeded Region Growing. *IEEE transactions on pattern analysis and machine intelligence*, *16*(6), 641–647.

Aizerman, M., Braverman, E., & Rozonoer, L. (1964). Theoretical foundations of the potential function method in pattern recognition learning. *Automation and Remote Control*, *25*, 821–837.

Alcón, J. F., Ciuhu, C., Kate, W., Heinrich, A., Uzunbajakava, N., Krekels, G., … De Haan, G. (2009). Automatic Imaging System With Decision Support for Inspection of Pigmented Skin Lesions and Melanoma Diagnosis. *IEE Journal of selected topics in signal processing*, *3*(1), 14–25.

Amelard, R., Wong, a., & Clausi, D. a. (2012). Extracting High-Level Intuitive Features (HLIF) for Classifying Skin Lesions Using Standard Camera Images. *2012 Ninth Conference on Computer and Robot Vision*, 396–403. doi:10.1109/CRV.2012.59

Bailo, G., Barbieri, I., & Cevasco, S. (2005). A Telemedicine Application Project in Emergency Handling. In *Proceedings of the 5th WSEAS Int. Conf. on Applied Informatics and Communications* (pp. 16–19). Malta.

Batistatos, M. C., Tsoulos, G. V., & Athanasiadou, G. E. (2012). Mobile telemedicine for moving vehicle scenarios: Wireless technology options and challenges. *Journal of Network and Computer Applications*, *35*(3), 1140–1150. doi:10.1016/j.jnca.2012.01.003

Bellina, L., & Missoni, E. (2009). Mobile cell-phones (M-phones) in telemicroscopy: increasing connectivity of isolated laboratories. *Diagnostic Pathology*, *4*(1), 19.

Brüllmann, D., Alvarez, P., & Willershausen, B. (2009). Recognition of root canal orifices in video sequences as a future support system during endodontic treatment. *Journal of endodontics*, *35*(10), 1400–1403. Retrieved from http://ukpmc.ac.uk/abstract/MED/19801239

Burger, W., & Burge, M. J. (2010). *Digital Image Processing. An Algorithmic Introduction Using Java*. (W. Burger, Ed.) (First Edit., p. 565). New York: Springer Science.

Cavalcanti, P. G., & Scharcanski, J. (2011). Automated prescreening of pigmented skin lesions using standard cameras. *Computerized Medical Imaging and Graphics : the Official Journal of the Computerized Medical Imaging Society*, *35*(6), 481–491. doi:10.1016/j.compmedimag.2011.02.007

Charlesworth, A. (2010). The ascent of smartphone. *Engineering and Technology*, *4*(3), 32–33.

Chitika. (2012). RIM Web Usage Down 25% in the Past Year.

Cortes, C., & Vapnik, V. (1995). Support-Vector Networks. *Machine Learning*, *20*(3), 273–297.

Dermnetnz.org. (2013). http://dermnetnz.org/.

DermQuest.org. (2010). The art of science and practice of dermatology.

Diepgen, T. L., & Yihune, G. (2013). Dermatology Online Atlas. Retrieved from http://www.dermis.net/doia/

Doi, K. (2009). Computer-aided diagnosis in radiological imaging: current status and future challenges. In J. K. Udupa, T. Zhang, M. Ding, J. Liu, H. Maître, H. Sun, … H. Tong (Eds.), *Proc. of SPIE* (Vol. 7497, p. 74971A–74971A–8). doi:10.1117/12.851178

Fan, R., Chen, P., & Lin, C. (2005). Working Set Selection Using Second Order Information for Training Support Vector Machines. *Journal of Machine Learning Research*, *6*(2005), 1889–1918.

Finlay, D. D., Nugent, C. D., Breen, C. J., Bond, R., & Moore, G. (2009). A smartphone based telemedicine system for recording limited lead body surface potential maps. In *Computers in Cardiology 2009* (pp. 237–240). Utah.

Freeman, H. (1974). Computer Processing of Line-Drawing Images. *ACM Computing Surveys*, *6*(1), 57–97.

Freeman, H., & Shapira, R. (1975). Determining the Minimum-Area Encasing Rectangle for an Arbitrary Closed Curve. *Communications of the ACM*, *18*(7), 409–413.

Ganapathy, K., & Ravindra, A. (2008). mHealth: a potential tool for health care delivery in India (pp. 1–9). Bellagio, Italy: The Rockefeller Foundation. Retrieved from http://ehealth-connection.org/files/conf-materials/mHealth_A potential tool in India_0.pdf

Ganster, H., Pinz, A., Röhrer, R., Wildling, E., Binder, M., & Kittler, H. (2001). Automated melanoma recognition. *IEEE TRANSACTIONS ON MEDICAL IMAGING*, *20*(3), 233–239.

Gao, Y., Mas, J. F., Kerle, N., & Navarrete Pacheco, J. A. (2011). Optimal region growing segmentation and its effect on classification accuracy. *International Journal of Remote Sensing*, *32*(13), 3747–3763. doi:10.1080/01431161003777189

Goasduff, L., & Pettey, C. (2012). Gartner says worldwide smartphone sales soared in fourth quarter of 2011 with 47 percent growth. *Gartner*. Retrieved October 10, 2012, from http://www.gartner.com/it/page.jsp?id=1924314

Hitchcock, C. L. (2011). The future of telepathology for the developing world. *Archives of Pathology & Laboratory Medicine*, *135*(2), 211–214. doi:10.1043/1543-2165-135.2.211

Hsieh, C.-H., Tsai, H.-H., Yin, J.-W., Chen, C.-Y., Yang, J. C.-S., & Jeng, S.-F. (2004). Teleconsultation with the Mobile Camera-Phone in Digital Soft-Tissue Injury: A Feasibility Study. *Plastic and Reconstructive Surgery*, *114*(7), 1776–1782. doi:10.1097/01.PRS.0000142402.07896.21

Hsu, C., Chang, C., & Lin, C. (2010). A Practical Guide to Support Vector Classification. *Bioinformatics*, *1*(1), 1–16. doi:10.1177/02632760022050997

Hu, M. K. (1962). Visual Pattern Recognition by Moment Invariants. *IRE Transactions on Information Theory*, *8*(2), 179–187.

Hugo, S., Lourenço, A., & Paz, N. (2011). Real-time Biosignal Acquisition and Telemedicine Platform for AAL based on Android OS. In *Proceedings of the 1st International Living Usability Lab Workshop on AAL Latest Solutions, Trends and Applications* (pp. 111 – 121). Rome, Italy.

International Telecommunication Union. (2012). Key Global Telecom Indicators for the World Telecommunication Service Sector. Retrieved from http://www.itu.int/ITU-D/ict/statistics/at_glance/KeyTelecom.html

Istepanian, R. S. H., Pattichis, C. S., & Laxminarayan, S. (2006). *Ubiquitous M-health systems and the convergence towards 4G mobile technologies*. (R. S. H. Istepanian, C. S. Pattichis, & S. Laxminarayan, Eds.)*Topics in Biomedical Engineering* (pp. 3–14). London, UK: Springer US. Retrieved from http://www.springerlink.com/index/u0t40j4h322632h6.pdf

Itseez. (2013). OpenCV. Retrieved from http://opencv.org/

Kapur, J. N., Sahoo, P. K., & Wong, A. C. . (1985). A New Method for Gray-Level Picture Thresholding Using the Entropy of the Histogram. *Graphical Models and Image Processing*, *29*(3), 273–285.

Keyes, L., & Winstanley, A. (2001). Using Moment Invariants for Classifying Shapes on Large Scale Maps. *Computers, Environment and Urban Systems*, *25*(1), 119–130.

Kurita, T., Otsu, N., & Abdelmalek, N. (1992). Maximum Likelihood Thresholding Based on Population Mixture Models. *Pattern recognition*, *25*(10), 1231–1240.

López Ruiz, N., Martínez Olmos, A., Pérez de Vargas Sansalvador, I. M., Fernández Ramos, M. D., Carvajal, M. A., Capitan Vallvey, L. F., & Palma, A. J. (2012). Determination of O2 using colour sensing from image processing with mobile devices. *Sensors and Actuators B: Chemical*, *171*, 938–945. doi:10.1016/j.snb.2012.06.007

Lowie, A. (2012). Teledermatology: A Tool for Nurse Practitioner Practice? *The Journal for Nurse Practitioners*, *8*(8), 617–620. doi:10.1016/j.nurpra.2012.06.003

Maglogiannis, I., & Doukas, C. N. (2009). Overview of advanced computer vision systems for skin lesions characterization. *IEEE transactions on information technology in biomedicine : a publication of the IEEE Engineering in Medicine and Biology Society*, *13*(5), 721–33. doi:10.1109/TITB.2009.2017529

Marshall, A., Medvedev, O., & Antonov, A. (2008). Use of a Smartphone for Improved Self-Management of Pulmonary Rehabilitation. *International Journal of Telemedicine and Applications*, *2008*, 1–5.

Martínez, A. M., & Kak, A. C. (2001). PCA versus LDA. *IEE Transactions on Pattern Analysis and Machine Intelligence*, *23*(2), 228–233.

Matheus, R., & Ribeiro, M. M. (2009). Telemedicine in Brazilian public policy management. In *Proceedings of the 3rd International Conference on Theory and Practice of Electronic Governance - ICEGOV '09* (pp. 274–280). New York: ACM Press. doi:10.1145/1693042.1693098

Mihailovic, B., Miladinovic, M., & Vujicic, B. (2009). Telemedicine in Dentistry (Teledentistry). In G. Graschew & T. A. Roehofs (Eds.), *Advances in Telemedicine: Applications in Various Medical Disciplines and Geographical Regions*.

Milligan, C., Roberts, C., & Mort, M. (2011). Telecare and older people: who cares where? *Social science & medicine (1982)*, *72*(3), 347–54. doi:10.1016/j.socscimed.2010.08.014

Montero, R. S., & Bribiesca, E. (2009). State of the Art of Compactness and Circularity Measures 1. *International Mathematical Forum*, *4*(27), 1305–1335.

Nutalapati, R., Boyapati, R., Jampani, N., & Dontula, B. S. K. (2011). Applications of teledentistry: A literature review and update. *Journal of International Society of Preventive and Community Dentistry*, *1*(2), 37–44. doi:10.4103/2231-0762.97695

Otsu, N. (1979). A Tlreshold Selection Method from Gray-Level Histograms. *IEEE Transactions on Systems, Man, and Cybernetics*, *9*(1), 62–66.

Panigrahi, S., & Gunasekaran, S. (2000). Computer Vision. In S. Gunasekaran (Ed.), *Nondestructive Food Evaluation: Techniques to Analyze Properties and Quality* (pp. 39–98). New York: Marcel Dekker, INC.

Panigrahi, S., Misra, M. K., Bern, C., & Marley, S. (1995). Background segmentation and dimensional measurement of corn germplasm. *Transactions of the ASAE.*, *38*(1).

Patel, V., McClendon, R., & Goodrum, J. (1998). Color computer vision and artificial neural networks for the detection of defects in poultry eggs. *Artificial Intelligence Review*, *12*, 163–176.

Perera, C. (2012). The Evolution of E-Health – Mobile Technology and mHealth. *Journal of Mobile Technology in Medicine*, *1*(1), 1–2. doi:10.7309/jmtm.1

Pinto, N., Cox, D. D., & DiCarlo, J. J. (2008). Why is real-world visual object recognition hard? *PLoS Computational Biology*, *4*(1), 151–156. doi:10.1371/journal.pcbi.0040027

Przystalski, K. (2010). Decision Support System for Skin Cancer Diagnosis, 406–413.

Rashkovska, A., Tomasic, I., & Trobec, R. (2011). A Telemedicine application: ECG data from wireless body sensors on a Smartphone. In *MIPRO, Proceedings of the 34th International Convention* (pp. 262–265). Opatija, Croatia.

Romero, G., Cortina, P., & Vera, E. (2008). Telemedicine and Teledermatology (II): Current State of Research on Dermatology Teleconsultations. *Actas Dermo-Sifiliográficas (English Edition)*, *99*(8), 586–597. doi:10.1016/S1578-2190(08)70326-3

SharkD. (2009). The HSV color model mapped to a cylinder. POV-Ray source is available from the POV-Ray Object Collection. Retrieved from http://commons.wikimedia.org/wiki/File:HSV_color_solid_cylinder.png

Shen, L., Hagen, J., & Papautsky, I. (2012). Point-of-care colorimetric detection with a smartphone. *Lab on a Chip*, *12*, 4240–4243. doi:10.1039/c2lc40741h

Smith, A. R. (1978). Color Gamut Transform Pairs. In *SIGGRAPH 78 Conference Proceedings* (pp. 1–17).

Sposaro, F., & Tyson, G. (2009). iFall: an Android application for fall monitoring and response. In *31st Annual International Conference of the IEEE EMBS* (Vol. 2009, pp. 6119–6122). Minneapolis, MN. doi:10.1109/IEMBS.2009.5334912

Suzuki, S., & Abe, K. (1985). Topological Structural Analysis of Digitized Binary Images by Border Following. *Computer Vision, Graphics, and Image Processing*, *30*(1), 32–46.

Tran, K., Ayad, M., Weinberg, J., Cherng, A., Chowdhury, M., Monir, S., … Kovarik, C. (2011). Mobile teledermatology in the developing world: implications of a feasibility study on 30 Egyptian patients with common skin diseases. *Journal of the American Academy of Dermatology*, *64*(2), 302–9. doi:10.1016/j.jaad.2010.01.010

Viola, P., & Jones, M. J. (2004). Robust Real-Time Face Detection. *International Journal of Computer Vision*, *57*(2), 137–154.

Westin, S. (2010). ISO 12233 Chart. Retrieved from http://www.graphics.cornell.edu/~westin/misc/res-chart.html

Wirthlin, D. J., Buradagunta, S., Edwards, R. a, Brewster, D. C., Cambria, R. P., Gertler, J. P., … Abbott, W. M. (1998). Telemedicine in vascular surgery: feasibility of digital imaging for remote management of wounds. *Journal of vascular surgery*, *27*(6), 1089–99. Retrieved from http://www.ncbi.nlm.nih.gov/pubmed/9652471

Woodbridge, J., Nahapetian, A., Noshadi, H., Sarrafzadeh, M., & William, K. (2009). Wireless health and the smart phone conundrum. *HCMDSS/ …*, *6*(2), 1–6. doi:10.1145/1859823.1859834

APPENDICES

APPENDIX. SKIN IMAGE FILENAMES

Melanoma file names			
1.png	2.png	3.png	4.png
5.png	6.png	7.png	8.png
9.png	10.png	11.png	12.png
13.png	14.png	15.png	16.png
17.png	18.png	19.png	20.png
21.png	22.png	23.png	24.png
25.png	26.png	27.png	28.png
29.png	30.png	31.png	32.png
33.png	34.png	35.png	36.png
37.png	38.png	39.png	40.png
41.png	42.png	43.png	44.png
45.png	46.png	47.png	48.png
49.png	50.png	51.png	52.png
53.png	54.png	55.png	56.png
57.png	58.png	59.png	60.png
61.png	66.png	68.png	78.png
79.png	80.png	81.png	82.png
83.png	84.png	85.png	86.png
87.png	88.png	89.png	90.png
91.png	92.png	93.png	94.png
95.png	96.png	97.png	98.png
99.png	100.png	101.png	102.png
103.png	104.png	105.png	106.png
107.png	108.png	109.png	110.png
111.png	112.png	113.png	114.png
115.png	116.png	117.png	118.png
119.png	120.png	121.png	122.png
123.png	124.png	125.png	126.png
127.png	128.png	129.png	130.png
131.png	132.png	133.png	134.png
135.png	136.png	137.png	138.png
139.png	140.png	141.png	142.png
143.png	144.png	145.png	146.png
147.png	148.png	149.png	150.png

151.png	152.png	153.png	154.png
155.png	156.png	157.png	

Benign moles file names

158.png	159.png	160.png	161.png
162.png	163.png	164.png	165.png
166.png	167.png	168.png	169.png
170.png	171.png	172.png	173.png
174.png	175.png	176.png	177.png
178.png	179.png	180.png	181.png
182.png	183.png	184.png	185.png
186.png	187.png	188.png	189.png
190.png	191.png	192.png	193.png
194.png	195.png	196.png	197.png
198.png	199.png	200.png	201.png
202.png	203.png	204.png	205.png
206.png	207.png	208.png	209.png
210.png	211.png	212.png	213.png
214.png	215.png	216.png	217.png
218.png	219.png	220.png	221.png
222.png	223.png	224.png	225.png
226.png	227.png	228.png	229.png
230.png	231.png	232.png	233.png
234.png	235.png	236.png	237.png
238.png	239.png	240.png	241.png
242.png	243.png	244.png	245.png
246.png	247.png	248.png	249.png
250.png	251.png	252.png	253.png
254.png	255.png	256.png	257.png
258.png	259.png	260.png	261.png
262.png	263.png	264.png	265.png
266.png	267.png	268.png	269.png
270.png	271.png	272.png	273.png
274.png	275.png	276.png	277.png
278.png	279.png	280.png	281.png
282.png	283.png	284.png	285.png
286.png	287.png	288.png	289.png

290.png	291.png	292.png	293.png
294.png	295.png	296.png	297.png
298.png	299.png	300.png	301.png
302.png	303.png	304.png	305.png